NUMERICAL EXAMINATION OF FLOATING OFFSHORE WIND TURBINE AND DEVELOPMENT OF AN INNOVATIVE FLOATING PLATFORM DESIGN

A Thesis Submitted to
the Graduate School of Engineering and Sciences of
İzmir Institute of Technology
in Partial Fulfillment of the Requirements for the Degree of

MASTER OF SCIENCE

in Civil Engineering

by
Yüksel ALKAREM

July 2020
İZMİR

ACKNOWLEDGMENTS

My sincerest thanks go to my dear advisor Assist. Prof. Dr. Bergüzar Özbahçeci for her perpetual guidance and support throughout my thesis. She has always assisted me in participating in extra curriculum activities, such as sharing some findings of this work at the national conference “9—Kıyı Mühendisliği Sempozyumu” held in Adana, November 2018.

Besides my advisor, I would like to thank Assoc. Prof. Dr. Ünver Özkol for his teachings with the aerodynamics part of the thesis and gave me the extraordinary opportunity to become part of this project and realize the spar-buoy scale model.

This study was funded by the Scientific and Technological Research Council of Turkey, TUBITAK under 217M451.

I want to send my sincere gratitude to my colleague Kadir Aktaş who helped with the spar-buoy design and analysis.

Many thanks to the Türkiye Bursları Scholarship, which sponsored my arrival in Turkey and the pursuit of my master’s degree.

Lastly, I would love to thank my parents, Adnan Alkarem and Hana Tattan, and my brothers, for their continuous support.

ABSTRACT

NUMERICAL EXAMINATION OF FLOATING OFFSHORE WIND TURBINE AND DEVELOPMENT OF AN INNOVATIVE FLOATING PLATFORM DESIGN

Harvesting offshore wind energy has been a primary stimulus for research recently as more shreds of evidence show the highly unexploited potential it carries. As water depth increases, fixed-bottom foundations become impractical and floating solutions must be adopted for offshore wind turbines. The underlying causes of high demands to reach accurate numerical simulation of floating offshore wind turbines are a plethora. The system's nonlinearities impose a serious challenge on the estimation of system responses, power production, and fatigue loading. Proper simulation of environmental stochastic loading from wind and wave plays a critical role in the analysis of such systems. The floating platforms govern the integrity of the entire system. There are different kinds of existing platforms like semi-submersible, spar, tension leg, etc. However, attempts to reduce hydrodynamic and aerodynamic-induced mean and dynamic excitations continue. This study examines the performance of a semi-submersible platform numerically using a hydro-aero coupled model and compares the results with the benchmark experimental data and other numerical model studies. A comparative study shows the present model depending on the second-order potential theory, and the dynamics of the mooring cables agrees well with the experimental results. A spar type platform is also modeled for mid-depth conditions. Moreover, a novel floating platform is developed and compared to existing alternatives in the field. The proposed platform achieves better stability in terms of mean offsets and dynamic oscillations, especially in pitch at extreme conditions. Another extinct feature of the design is the diminished tensile strain in the mooring lines for a relatively shorter cable length and equal linearized horizontal stiffness.

ÖZET

DENİZ ÜSTÜ YÜZER RÜZGAR TÜRBİNLERİNİN SAYISAL MODELLEME ILE İNCELENMESİ VE YENİ BİR YÜZER PLATFORMUN GELİŞTİRİLMESİ

Açık denizde rüzgar gücünün karaya göre çok daha yüksek olması nedeniyle, açık denizdeki rüzgardan enerji elde edilmesi, yenilenebilir enerjinin yaygınlaşması açısından gün geçtikçe önem kazanmaktadır. Deniz suyu derinleştikçe karadaki türbinler gibi tabana oturan sabit sistemler (kazık gibi) ekonomik bir çözüm olma niteliğini kaybetmekte ve yüzer platformlar tercih edilmektedir. Yüzer türbin sistemlerinde görülen doğrusal olmayan problemlerin çözümü, sistemin davranışlarının tahmin edilmesi, enerji elde etme ve yorulma problemlerinin incelenmesi açısından kritiktir. Dolayısıyla doğru ve güvenilir bir yüzer rüzgar türbini modellemesi konusunda çalışmalar devam etmekte ve önem kazanmaktadır. Deniz üstü yüzer türbinlerinde yüzer platform, sistemin bütünlüğü ve stabilitesi için en önemli yapıdır. Yarı-batık, spar (direk), TLP gibi çeşitli yüzer platformlar bulunmakla birlikte hidrodinamik ve aerodinamik kaynaklı hareketlerin azaltılarak daha stabil ve ekonomik yüzer platform arayışları sürmektedir. Bu çalışmada, öncelikle yarı-batık bir yüzer platform, geliştirilen hidro-aero analizi akuple edilmiş bir sayısal modelle incelenmiştir. Geliştirilen model hem röper kabul edilen güvenilir ve kullanıma açık hidrolik model deneyleri sonuçlarıyla, hem de aynı yarı-batık platformu modelleyen dünya çapında başka araştırmacıların kullandığı modellerle elde edilen sonuçlarla karşılaştırılmıştır. Sonuçlar geliştirilen modelin deney değerleriyle oldukça uyumlu ve diğer kodlara göre deney sonuçlarına daha yakın deplasman, rotasyon ve kuvvet değerleri verdiğini göstermiştir. Daha sonra analitik yöntemler ve geliştirilen modelleme kullanılarak spar tipi bir platformun da en başından tasarımı yapılmıştır. Ayrıca yeni bir platform tipi geliştirilmiş ve performansı yarı-batık ve spar platformlarla karşılaştırılmıştır. Yeni platformun özellikle baş-kıç vurma rotasyonu diğer platformlara göre çok daha düşük çıkmıştır ki baş-kıç vurma rüzgar türbini ve enerji elde edilmesinde en önemli serbestlik derecesi olarak kabul edilmektedir. Yeni platformun diğer bir avantajı da bağlanma zincirlerinde oluşan düşük gerilmedir.

TABLE OF CONTENTS

LIST OF FIGURES

Figure **Page**

Figure **Page**

Figure **Page**

Figure **Page**

Figure **Page**

Figure **Page**

Figure **Page**

LIST OF TABLES

Table **Page**

Table **Page**

ABBREVIATIONS

AOF	Aggregate Objective Function
BEM	Blade Element Momentum theory
BET	Blade Element Theory
CAE	Computer-Aided Engineering Tools
DLL	Dynamic Link Library
DMM	Dynamic Mooring Model
DoF	Degree of Freedom
DoF^o	Degree of Freedom of Interest
DP	Dynamic Positioning
DSA	Deterministic Spectral Amplitude
FAST	Fatigue, Aerodynamics, Structures, and Turbulence
FD	Frequency-Domain
FDT	Free Decay Test
FFT	Fast Fourier Transform
FOWT	Floating Offshore Wind Turbine
FSI	Fluid-Structure Interaction
HAWT	Horizontal Axis Wind Turbine
HF	High-Frequency Response
IEA	International Energy Agency
LC	Load Case
LF	Low-Frequency Response
ME	Morison Equation Model
MT	Momentum Theory
NREL	National Renewable Energy Laboratory
O&G	Oil and Gas
OC3	Offshore Code Comparison Collaboration
OC4	Offshore Code Comparison Collaboration Continuation
OC5	Offshore Code Comparison Collaboration, Continued, with Correlation
PF	Potential Flow model
PSD	Power spectrum density

QSMM	Quasi-Static Mooring Model
RAO	Response Amplitude Operators
RNA	Rotor-Nacelle Assembly
SWL	Still-Water Level.
TD	Time-Domain
TLB	Tension Leg Buoy
TLCD	Tuned Liquid Column Dampers
TLP	Tension Leg Platform
ULS	Ultimate Limit State
VAWT	Vertical Axis Wind Turbine
WF	Wave-Frequency Response

NOMENCLATURE

Symbol		Description	Units
A	=	Added mass matrix	[t or $t \cdot m^2$]
A_{out}	=	Cross-sectional area of the outer part of the shell	[m^2]
A_{wp}	=	Water-plane area	[m^2]
APE	=	Absolute percentage error	[−]
BM	=	Distance between metacenter and center of buoyancy	[m]
$C_{l,fs}$	=	Lift coefficient in a fully separated flow	[m]
$C_{l,inv}$	=	Lift coefficient in an inviscid flow	[−]
C_{l_1}	=	Lift coefficient at the merged angle of attack	[−]
C_P	=	Power coefficient	[−]
C_T	=	Thrust coefficient	[−]
C_a	=	Added mass coefficient	[−]
C_d	=	Drag coefficient	[−]
C_l	=	Steady lift coefficient	[−]
C_m	=	Inertia coefficient	[−]
C_q	=	Elementary Torque coefficient	[−]
C_t	=	Elementary Thrust coefficient	[−]
$\overrightarrow{CoB}$	=	Position vector of the center of buoyancy = (x_B, y_B, z_B)	[m]
$\overrightarrow{CoG}$	=	Position vector of the center of gravity = (x_g, y_g, z_g)	[m]
D	=	Cylindrical diameter	[m]
D_1	=	Diameter of the upper portion of the spar-buoy	[m]
D_2	=	Diameter of the lower portion of the spar-buoy	[m]
D_T	=	Tower diameter	[m]
D_f	=	Footing diameter	[m]
EA	=	Axial stiffness of the mooring cable	[kN]

Symbol		Description	Units
$F_{p_{jj}}$	=	Linear damping force	[kN]
$F_{q_{jj}}$	=	Quadratic damping force	[kN]
$\overrightarrow{F_h}$	=	Hydrodynamic forces on the mooring cable	[kN]
F_B	=	Buoyancy force	[kN]
F_M	=	Force due to Morison formula	[kN]
F_T	=	Thrust force	[kN]
F_{TL}	=	Tip-loss factor	$[-]$
F_d	=	Hydrodynamic drag force	[kN]
F_j	=	Total wave force	[kN]
$F_j^{lines,0}$	=	Quasi-static mooring forces at the equilibrium position	[kN]
F_j^{lines}	=	Quasi-static mooring forces on the platform	[kN]
F_{wk}	=	Wave-kinematics force	[kN]
F_{zj}	=	Reaction force from the seabed	[kN]
$\overline{GM}$	=	Metacentric height	[m]
H	=	Wave height	[m]
$\overline{H}$	=	Mean wave height	[m]
H_{f_1}	=	Height of the tower base	[m]
H_0	=	Height of the portion above the SWL of the spar-buoy	[m]
H_1	=	Height of the upper portion of the spar-buoy	[m]
H_{10}	=	mean of the greatest one-tenth wave heights in the wave profile	[m]
H_2	=	Height of the conical region of the spar-buoy	[m]
H_3	=	Height of the lower portion of the spar-buoy	[m]
H_b	=	Ballast height	[m]
H_f	=	Footing thickness	[m]
H_s	=	Significant wave height	[m]
I_{wp}	=	Principal second moment of the water-plane area	$[m^4]$
I_{xx}	=	Roll moment of inertia	$[t \cdot m^2]$
I_{yy}	=	Pitch moment of inertia	$[t \cdot m^2]$

Symbol		Description	Units
I_{zz}	=	Yaw moment of inertia	$[\mathrm{t}\cdot\mathrm{m}^2]$
$J(x)$	=	Aggregate objective function	$[-]$
K	=	Hydrostatic stiffness matrix	$[\frac{\mathrm{kN}}{\mathrm{m}}$ or $\mathrm{kN}.\frac{\mathrm{m}}{\mathrm{deg.}}]$ (diagonal)
K_{jj}	=	Diagonal element in the hydrostatic stiffness matrix	$\left[\frac{\mathrm{kN}}{\mathrm{m}}\right]$or $\left[\mathrm{kN}.\frac{\mathrm{m}}{\mathrm{deg.}}\right]$
KC	=	Keulegan-Carpenter Number	$[-]$
L	=	Wavelength	[m]
L_B	=	Length of the laid portion of the mooring cable	[m]
L_c	=	Total unstretched length of the cable	[m]
M	=	Mass matrix	$[\mathrm{t}$ or $\mathrm{t}\cdot\mathrm{m}^2]$
M_T	=	Thrust-induced moment	$[\mathrm{kN}\cdot\mathrm{m}]$
M_X	=	Restoring moment for roll rotation	$[\mathrm{kN}\cdot\mathrm{m}]$
M_Y	=	Restoring moment for pitch rotation	$[\mathrm{kN}\cdot\mathrm{m}]$
N_c	=	Number of cables	$[-]$
O	=	Point of origin (first convention)	$[-]$
O'	=	Point of origin (second convention)	$[-]$
P_{jj}	=	Linear damping coefficient	$[-]$
Q_{jj}	=	Quadratic damping coefficient	$[-]$
QTF_{ij}	=	Quadratic transfer function	$\left[\frac{\mathrm{kN}}{\mathrm{m}^2}\right]$
R	=	Rotor radius	[m]
$\vec{R}$	=	Vector position of the first node in a cable element	[m]
RX	=	Roll rotation	[deg.]
RY	=	Pitch rotation	[deg.]
RZ	=	Yaw rotation	[deg.]
$S(\omega)$	=	Spectral density function of wave elevation	$\left[\frac{\mathrm{m}^2}{\mathrm{Hz}}\right]$
$S_U(\omega)$	=	Spectral density function of the wind velocity	$\left[\frac{\mathrm{m}^2}{\mathrm{s}}\right]$
T	=	Wave period	[s]
$\vec{T}$	=	Cable tension	[kN]

Symbol		Description	Units
$T_{c,dyn}$	=	Characteristic dynamic tension value	[kN]
$T_{c,means}$	=	Characteristic mean tension value	[kN]
T_0	=	Mooring cable pretension	[kN]
T_H	=	Horizontal component of the cable tension	[kN]
T_{MPM}	=	Most probable maximum tension	[kN]
T_V	=	Vertical component of the cable tension	[kN]
T_d	=	Design tension	[kN]
T_{n_j}	=	Natural period of the j^{th} mode	[s]
T_p	=	Peak period	[s]
U_0	=	Undisrupted upstream wind velocity	$\left[\frac{\mathrm{m}}{\mathrm{s}^2}\right]$
U_{10}	=	Wind velocity at 10 m height	$\left[\frac{\mathrm{m}}{\mathrm{s}}\right]$
U_n	=	Normal velocity acting on the airfoil	$\left[\frac{\mathrm{m}}{\mathrm{s}^2}\right]$
U_{rel}	=	Relative velocity seen by the airfoil	$\left[\frac{\mathrm{m}}{\mathrm{s}^2}\right]$
U_t	=	Tangential velocity acting on the airfoil	$\left[\frac{\mathrm{m}}{\mathrm{s}^2}\right]$
$\vec{V}$	=	Shear force on a cable element	[kN]
W	=	Actual induction velocities	$\left[\frac{\mathrm{m}}{\mathrm{s}}\right]$
W_{int}	=	Intermediate induction velocities	$\left[\frac{\mathrm{m}}{\mathrm{s}}\right]$
W_{qs}	=	Quasi-static induction velocities	$\left[\frac{\mathrm{m}}{\mathrm{s}}\right]$
X	=	Surge position	[m]
Y	=	Sway position	[m]
Z	=	Heave position	[m]
a	=	Wave amplitude	[m]
$\vec{a}_j$	=	Nodal acceleration of a cable element	$\left[\frac{\mathrm{m}}{\mathrm{s}^2}\right]$
a_B	=	Axial induction factor	$[-]$
a'_B	=	Tangential induction factor	$[-]$
a_{FD}	=	Amplitude of a response in frequency-domain	[m or deg. or kN]
c	=	Wave celerity	$\left[\frac{\mathrm{m}}{\mathrm{s}}\right]$
c	=	Chord length	[m]

Symbol		Description	Units
c_n	=	Normal projection of drag and lift forces	[kN]
c_t	=	Tangential projection of drag and lift forces	[kN]
d	=	Draft	[m]
dA_r	=	Annular area of the rotor	$[\mathrm{m}^2]$
f	=	Frequency	[Hz]
f_s	=	The separation function	$[-]$
g	=	Gravitational acceleration	$\left[\frac{\mathrm{m}}{\mathrm{s}^2}\right]$
h	=	Water depth	[m]
k	=	Wave number	$\left[\frac{1}{\mathrm{m}}\right]$
k_{jj_m}	=	Linearized mooring line stiffness	$\left[\frac{\mathrm{kN}}{\mathrm{m}}\right]$or $\left[\mathrm{kN}.\frac{\mathrm{m}}{\mathrm{deg.}}\right]$
m	=	Total structural mass of the system	[t]
m_0	=	Zero[th] moment of a PSD	[m or deg or kN]
m_a	=	Added mass	[t]
m_b	=	Ballast mass	[t]
m_s	=	Shell mass	[t]
m'	=	Net mass of the element cable	[t]
mrl	=	Mean run length parameter	$[-]$
n	=	Wave spreading parameter	$[-]$
p	=	hydrodynamic pressure	$\left[\frac{\mathrm{kN}}{\mathrm{m}^2}\right]$
$\dot{q}$	=	Wave particle velocity	$\left[\frac{\mathrm{m}}{\mathrm{s}}\right]$
$\ddot{q}$	=	Wave particle acceleration	$\left[\frac{\mathrm{m}}{\mathrm{s}^2}\right]$
r	=	Radial position along the blade	[m]
s_{fs}	=	Slope of the linear zone of the dynamic stall model	$[-]$
t	=	Time	[s]
$\dot{u}_j$	=	Body velocity in the translational mode *j*	$\left[\frac{\mathrm{m}}{\mathrm{s}}\right]$
$\ddot{u}_j$	=	Body acceleration in the translational mode *j*	$\left[\frac{\mathrm{m}}{\mathrm{s}^2}\right]$
u_j	=	Translational mode of motion	[m]
x_f	=	Fairlead horizontal position	[m]

Symbol		Description	Units
x_j	=	The j[th] mode of body motion	[m or deg.]
$\hat{z}$	=	Depth of the mud layer	[m]
z_{hub}	=	Hub height	[m]
z_f	=	Fairlead vertical position	[m]
∇	=	Volumetric displacement	$[m^3]$
ΔS_e	=	Cable element length	[m]
Δt	=	Timestep	[s]
$\Delta\alpha$	=	Angle of attack extent of the transition zone	[deg.]
Φ	=	First-order velocity potential	$\left[\frac{m^2}{s}\right]$
Ω	=	Rotor angular velocity	$\left[\frac{rad}{s}\right]$
γ	=	Peak enhancement factor	$[-]$
γ_{dyn}	=	Load factor for dynamic tension	$[-]$
γ_{mean}	=	Load factor for mean tension	$[-]$
ε	=	For mooring system, the axial strain in the cable	$[-]$
η	=	Wave surface elevation	[m]
θ_c	=	Angle between the cables	[deg.]
θ_j	=	Rotational mode of motion	[deg.]
θ_p	=	Blade pitch angle	[deg.]
$\mu(x)$	=	Objective function	$[-]$
μ_c	=	Synthetic calibrating coefficient	$[-]$
ν	=	Longuet-Higgins parameter	$[-]$
ρ_a	=	Air density	$\left[\frac{kg}{m^3}\right]$
ρ_f	=	Water density	$[t/m^3]$
τ_1, τ_2	=	Time constant used in the dynamic wake/inflow model	$[-]$
φ_{r_j}	=	Radiation wave induced by the j[th] body motion contribution to the velocity potential solution	$\left[\frac{m^2}{s}\right]$
φ_1	=	Incident wave contribution to the velocity potential solution	$\left[\frac{m^2}{s}\right]$

Symbol		Description	Units
φ_d	=	diffraction wave contribution to the velocity potential solution	$\left[\frac{\mathrm{m}^2}{\mathrm{s}}\right]$
χ	=	Wave direction	
ω	=	For hydrodynamic model, angular frequency	$\left[\frac{\mathrm{rad}}{\mathrm{s}}\right]$
ω	=	For mooring dynamics, weight of the cable per unit length	$\left[\frac{\mathrm{kN}}{\mathrm{m}}\right]$
ϵ	=	Twist angle	[deg.]
ϕ	=	Air flow angle	[deg.]

CHAPTER 1

INTRODUCTION

1.1. Research Background and Problem Statement

The ever-increasing global tendency to decarbonize energy systems drives more interest in the development in the field of sustainability and the pursuit of alternative, renewable energy resources. Due to its high accessibility, wind energy is the first natural resource to exploit.

The wind industry is experiencing a shift to the offshore market, and this tendency is most likely to continue in the coming decades. This shift is caused by:

1- the offshore wind being more energetic and less turbulent due to the absence of obstacles and low aerodynamic roughness length (Landberg, 2016) rendering it highly potential,
2- the vast, unexploited oceanic territories, and the depletion of onshore and even near-shore locations in some part of the world,
3- the fact that offshore wind farms are socially less inconvenient.

The market moves inshore, but it is also gradually sailing further from the coastline, where wind farms operate more efficiently. Figure 1.1 illustrates the transition of online offshore wind farms in Europe from the beginning of the 21st century and their average water depth. As can be seen, the continuation of this trend implicates additional challenges. As water depth increases, fixed-bottom foundations become impractical and floating solutions must be adopted.

A unit or an array of a horizontal or vertical axis wind turbine (HAWT/VAWT) mounted on a floating platform to provide reasonable stability under environmental excitations such as wind, wave, and currents constitute what is known as a floating offshore wind turbine (FOWT) system. Catenary or taut mooring lines connect the platform to the seabed for station-keeping purposes and provide external restoring forces and moments in horizontal degrees of freedom (DoF). The system becomes primarily dependent upon how stable the substructure is. Owed to the relative novelty of this field,

the design of FOWT platforms is currently inspired by the Oil & Gas (O&G) industry. However, this translation is not optimized to support such slender bodies due to their fundamentally different characteristics from O&G structures. The inclusion of aerodynamic forces, hydrodynamic effects on the platform, gearbox system, and the integrity of the heavy rotor-nacelle assembly (RNA) and many other variables imply additional constraints on the design.

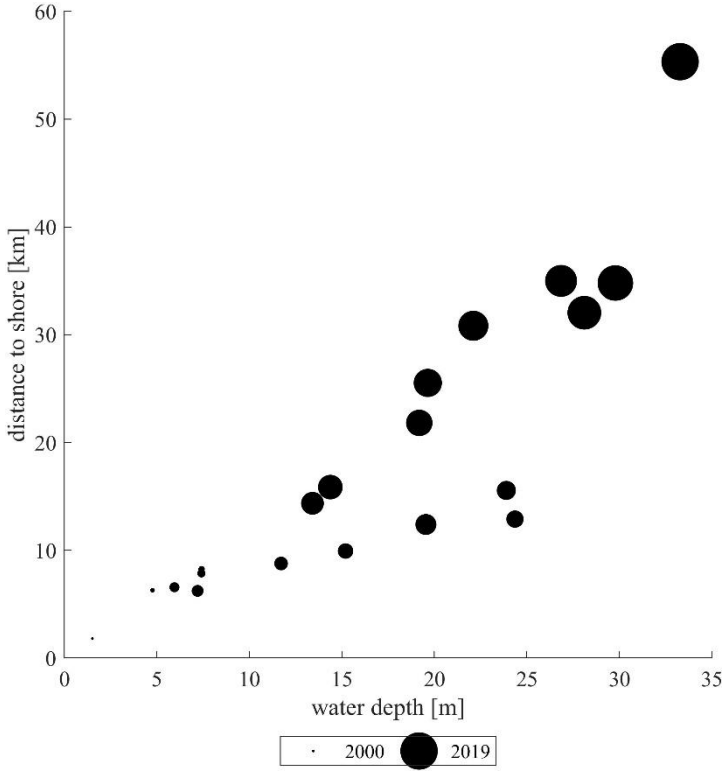

Figure 1.1: Average water depth and distance-to-shore of online wind farms in Europe between 2000-2019.
(source: Walsh, 2019a)

1.2. Aim and Scope of the Study

This study aims to simulate the fully-coupled hydrodynamics, mooring dynamics, and aerodynamics of FOWT systems while keeping a general focus on the first two. The serviceability and elasticity of the system are not included as part of the scope. The central thesis objectives are:

1- the investigation of different calibration schemes in the numerical models of the semi-sub platform to examine their capabilities of capturing hydrodynamic second-order forces and the investigation of wave irregularity on the system performance in terms of wave directionality, and the frequency spectrum shape,

2- the development of a spar-buoy type platform design suitable for the support of a 300 kW HAWT,

3- the optimization of an innovative platform geometry in terms of hydrostatic and hydrodynamic performance employing thorough parametric analysis and comparing its performance with the readily available designs. The optimization is scoped to passive geometrical alteration.

1.1. The Structure of the Thesis

The thesis is constructed as following; a review of the relevant scholarly work is provided in chapter 2. Methodologies, assumptions, and modeling setups are described in chapter 3, followed by the development of semi-sub numerical models in chapter 4 and the spar-buoy model in chapter 5. Chapter 6 comprises the definition of the innovative design where parametric analysis is carried out to optimize the platform that is compared with other existing floating systems in Chapter 7. This thesis closes with the main conclusions drawn in this study and provides future works, as mentioned in Chapter 8.

CHAPTER 2

LITERATURE REVIEW

2.1. General Review

The rapid expansion of the wind industry made it the 2nd most abundant form of power generation in 2016 in the European Union (Pineda Iván and Pierre, 2016). By the end of 2019, the continent has 205 GW of wind energy capacity, covering 15% of electricity demand (Walsh, 2019b).

The potential wind carries offshore is driving the wind industry to shift from land-based to sea-based wind farms. An offshore wind farm encounters 90% greater wind on average compared to an onshore wind farm (Archer and Jacobson, 2005). Since 2009, offshore share of newly installed wind farms rose from 6% to a staggering 31% in 2019, and this tendency is more likely to continue in the coming decades (Walsh, 2019b). Fixed-bottom foundations are deployed for low to moderate water depths such as monopole (shallow waters) and jacket support structures (moderate depths).

Wind has most of its energy condensed at locations further away from the coastline, where water is deep enough to render fixed-bottom foundations unfeasible. Therefore, floating technologies must be adopted.

2.2. Floating platforms

Floating platforms are classified according to how they achieve their stability in roll and pitch rotations (Butterfield et al., 2005). Passive stability methods comprise:

1- Ballast: the floating platform delivers better rotational restorability through gravity by adding weight at high drafts. Spar-buoy primarily uses this method (Jonkman, 2010).

2- Buoyancy: restorations are produced by the disturbance of the balanced buoyant force as the platform moves through increasing the water-plane area. Barge platform is a typical example of this method (Jonkman, 2007).

3- Tensioned mooring cables: any deviation from the platform's original position creates an unbalanced sum of forces on the platform. Mooring lines must be highly tensioned at the equilibrium position for the restorations to be sufficient, which necessitates the platform to have an excess buoyancy bank to create that tension. Tension leg platform (TLP) principally adopts this approach (Jonkman and Matha, 2013).

Apart from these passive approaches, semi-active or active stability methods also exist, such as dynamic positioning (DP) systems that help restore the original position by applying perpetual dynamic thrusters (Sørensen, 2011).

Although these methods are different in principle, any moored platform ought to use all of them, and when it comes to the first two methods, it is conceptually impossible to apply one without the other. Because no matter how slender the platform is, it has to pierce water creating a water-plane area. Similarly, barge platforms must apply some ballast to counterweight the wind turbine above and lower the center of gravity of the whole system (Wayman, 2006). Finally, even if the mooring system is solely used for station-keeping purposes, suspended cable weight exerts vertical forces and helps increasing hydrostatic restoration in vertical DoFs. Figure 2.1 illustrates the primary platforms supporting a HAWT.

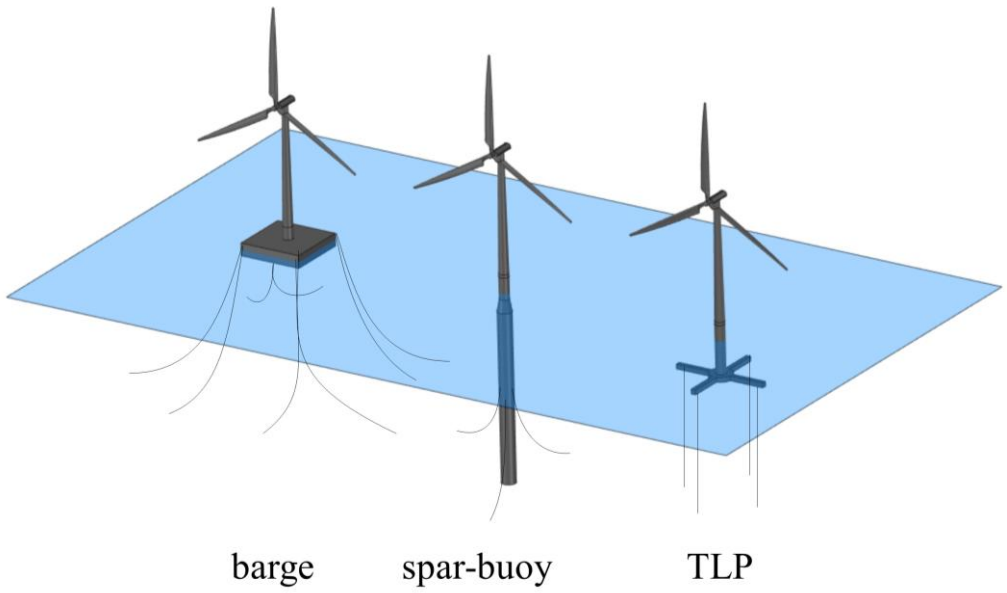

Figure 2.1: Primary platform designs with the 5 MW wind turbine mounted on top of them.

That being said, some floaters are more hybrid than others. Semi-submersible platforms are typical examples of adopting buoyancy as their primary stability method and ballast as a secondary method, which fortifies the system's resistance and restoring moments against exciting forces. The catenary mooring lines – connected to the sea bed - work as minor stabilizers (A. N. Robertson et al., 2016). Another example is the taught leg buoy (TLB) platform designed at MIT that combines the concept of a TLP and a spar-buoy (Sclavounos et al., 2010). Butterfield et al. (2005) suggested the stability triangle method (see Figure 2.2 to organize and quantify the contribution from each technique to the final rotational stiffness of the platform. One can add a dimension to the triangle to account for the DP stabilization method.

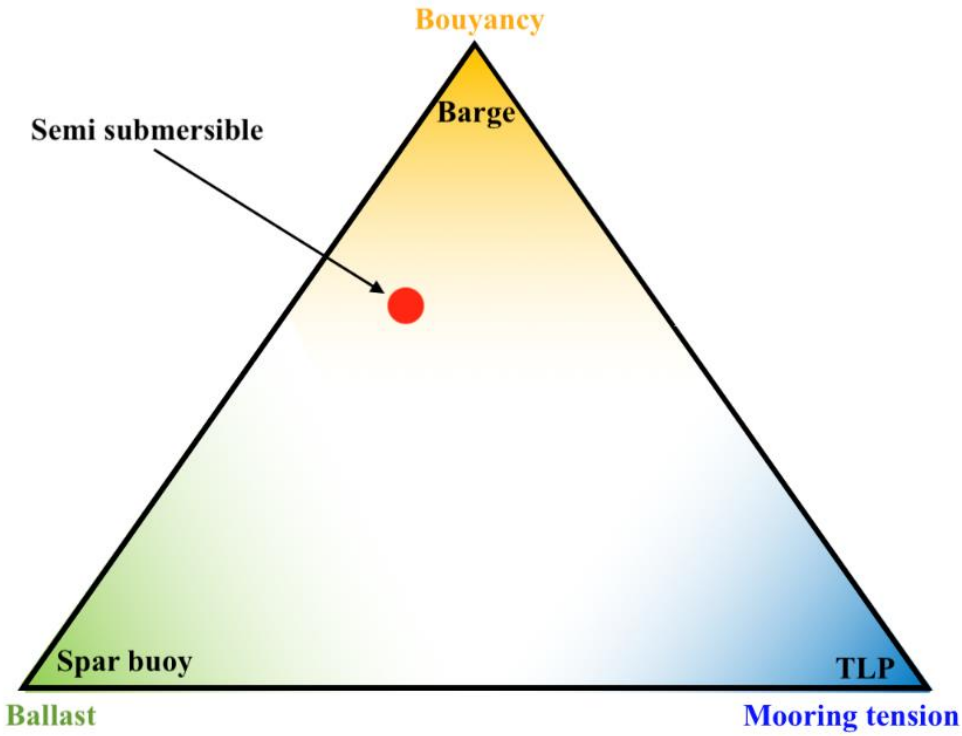

Figure 2.2: Stability triangle showing the representative platform for each method and a hybrid example.

As for the superstructure, it is believed that each wind turbine in an offshore farm operating at deep waters must be rated at 5 MW or higher for the overall system to be cost-effective (Karimirad and Moan, 2012a). As such, National Renewable Energy Laboratory (NREL) has built the 5-MW baseline wind turbine, and now it is taken as the reference for most offshore development studies (Jonkman et al., 2009).

2.3. Numerical Modeling of FOWT in the Literature

The underlying physics driving the dynamics of FOWT systems are multi-various and interactive, requiring Computer-aided Engineering (CAE) tools to accurately estimate the behavior of the FOWT system (Jonkman and Buhl, 2005). The fully-coupled aero-hydro-servo-elastic FAST model is a famous example.

Some scholars prefer accurate solutions, such as Computational Fluid Dynamics (CDF)-based numerical models to capture the platform motions and forces by solving Navier-Stokes Equations. It comes at the expanse of computational cost. Works done by (Benitz et al., 2015; Tran and Kim 2018) are examples of this method. Others have devised simplified aero-hydro dynamic models to produce fast results with the sacrifice of some accuracy (Karimirad and Moan 2012b; Kim et al., 2015). If CFD is to be avoided, the application of a potential-flow or Morison's equation-based approaches in the hydrodynamic sub-model and the Blade Element Momentum Theory (BEM) in the aerodynamic sub-model are the main alternatives. Potential flow neglects viscous-induced excitation/damping, while Morison's approach is inapplicable for large diffracting structures. These limitations must be considered to capture the fundamental hydrodynamic forces exerted on the platform. A just approach is to use both models simultaneously. ANSYS™ AQWA® package is a popular tool that embraces the two methods (ANSYS Inc., 2013). It is composed of two systems:

1- Hydrodynamic diffraction system, which is used to developing the primary hydrodynamic properties required to conduct complex motion analyses. The three-dimensional hydrodynamic effects of multiple floating bodies can be investigated.

2- Hydrodynamic response system, which is used as an upstream solution to execute dynamic analysis of the floating system's global performance either in time or frequency domain using the information provided by the hydrodynamic diffraction model. Additionally, physical connections, such as mooring lines and articulations between different floating bodies or between a body and a fixed point can be equipped to the dynamic analyses for modeling restraining effects on the vessel(s).

Typically, FOWT motion is divided into low-frequency (LF) and wave-frequency (WF) responses. LF is governed by the change in the wind and nonlinear wave forces, whereas linear wave-diffraction forces define the WF response. If the turbine is operating under

dynamic wind excitations, wind excitations are the dominant influence upon LF, but if the turbine is parked/idled and its blades are feathered, second-order hydrodynamic forces control LF responses even under higher wind speeds due to the absence of thrust, the main aerodynamic driving force (Coulling et al., 2013)

Second-order wave forces originating in irregular seas can be described as the contribution of a pair of sinusoidal waves (Pinkster, 1980). For a pair of equal frequencies, their values correspond to a constant force, namely a mean drift forces creating an offset at the direction of the loading. The difference or sum of the frequencies (non-diagonal elements of the Quadratic transfer function QTF, defined in section 3.2.1.4) may create non-constant slowly varying drift forces (difference-frequency) or high-frequency (HF) oscillations (sum-frequency) if that natural frequency of the overall system or any of its components' lock in at that frequency. For floating platforms, the difference-frequency entails a challenge of creating response amplification, especially if the DoF natural modes are close to the wave-dominated region (Pinkster, 1980). Karimirad (2013) has studied various hydrodynamic models and investigated the importance of the calculations of second-order forces on Hywind Spar-buoy FOWT response and found that heave motion is the most affected DoF. Additionally, as conditions grow extreme, nonlinear hydrodynamic effects cause the difference between the models to become more prominent. Coulling et al. (2013) examined the importance of second-order wave-diffraction forces on the semi-submersible platform's LF behavior. They concluded that better agreement is reached with model test data after the inclusion of wave nonlinearities, especially at wave-only environmental excitation.

Tensions in the mooring can be modeled using either quasi-static or dynamic modeling. However, while the quasi-static model contributes to accurate static tension values, it results in under-predicting the tensions in the cables under dynamic motion. Ergo, the dynamic model is more appropriate to capture the dynamic tension responses (M. Masciola et al., 2013). Dynamic tensions are a function of the fairleads' motion. Therefore, erroneous prediction of structural response subsequently influences the tension values (Hall and Goupee, 2015), but the influence of tension dynamics on the global performance of the floating wind turbine outside snap load events is insignificant (M. D. Masciola, 2013; Karimirad, 2013).

2.3.1. Offshore Code Comparison Collaboration Projects (OC3, OC4, and OC5)

To address and evaluate the robustness of different modeling techniques, International Energy Agency (IEA) initiated three tasks to test, validate, and benchmark the performance of numerous offshore wind turbine modeling tools developed by several institutions and companies worldwide. FOWT took a significant part in these projects. OC3-Hywind Spar was investigated under Offshore Code Comparison Collaboration (OC3) project phase IV brought forth by the first task (IEA Task 23, Subtask 3), which was initiated in 2004 and ended in 2009 (Jonkman et al., 2010). The second task (IEA Task 30) introduced was the Offshore Code Comparison Collaboration Continuation (OC4) project in 2010 (Robertson et al., 2014), where a semi-submersible platform supporting the NREL 5-MW baseline wind turbine was delved into in phase II. OC3 and OC4 are quite similar in structure the way the model is created. They are tested under different loading conditions first to examine specific components of the system and full system response and later verified through rigorous code-to-code comparisons. The third project, Offshore Code Comparison, Continued, with Correlation (OC5), as an extension to IEA Task 30 starting from 2014 (Robertson, 2015), was unlike previous projects, it took a step forth. It made additional code-to-physical data comparisons for the validation of three different systems. Accordingly, the procedure was modified, where participants need to choose specific data sets to calibrate aerodynamic, hydrodynamic, and structural properties of their models. Various approaches are adopted by participants to model the aerodynamics, hydrodynamics, and mooring connections of the system. For instance, participants who used 1st order potential theory have calculated Morison drag forces through the application of strip-theory, while others have included damping matrix to approximate these forces. Participants in OC5 phase II had their results compared with an experiment based on a DeepCwind FOWT model at Maritime Research Institute of Netherlands (MARIN) in 2013. The test model is conducted on the Marin Stock wind turbine (MSWT), a performance-match scale-model wind turbine (Kimball et al., 2014). Conclusions are drawn that later helped better understanding CAE tools performance under various loadings and how they can be further developed in the future.

2.4. Effects of Wave Irregularity

Although these projects use stochastic wind and wave environmental loading, it does not fully represent the chaotic nature at open seas. The definition of wave irregularity is complex. The superposition of waves with different heights and periods is just one aspect. For instance, the variation in energy distribution in the wave spectrum for two equally energetic, fully developed seas might impact LF and WF responses. This has only been narrowly investigated in the literature. Barrera et al. (2019) has studied the significance of wave parameters over the mooring dynamics in severe sea states and has demonstrated that maximum tensions are independent on maximum wave heights, but instead on how the waves are arranged. Saulnier et al. (2011) have underlined the essential role played by the groupiness of the wave in addition to the standard wave parameters (wave height and period) on the behavior of wave energy converters and, consequently, on the power production estimation. The spreading of energy on a broader range of directions is another form of wave irregularity than the frequent application of unidirectional waves. Kvittem and Moan (2015) studied fatigue forces on a semi-submersible platform under misaligned wind and wave excitations. They concluded that the assumption of unidirectionality is conservative. Still, the most considerable fatigue damage is a function of the wave direction. When Zhang and Ishihara (2016) tested the spreading effect on the Fukushima MIRAI 2MW FWT prototype, they concluded that the multidirectional assumption decreases the motion in surge, heave, and pitch. However, Waals (2009) derived a 4-dimensional QTF that relates to a pair of waves of different frequencies and directions for the calculation of low-frequency motions of a soft-moored ship. He found that wave directionality may have a considerable impact on vessel motion, especially in shallow water. He also deduced that conventional simulations are not conservative, particularly of motions not excited by unidirectional loading. The same conclusion was reached by Duarte et al. (2014) after they tested an equal-energy discretization method for synthesizing directional wave spectra on a semi-submersible OC4 platform. They detected a significant increase in sway and roll motion.

A complete analysis of the triggering or weakening effect of wave groupiness and wave multidirectionality under a wide range of mean wave directions on low and wave frequency responses (and the correlation between the two) and cable tensions compared to the conventional excitation methods is missing. This study addresses these influences

calibrating and validating the hydrodynamic and mooring dynamics of the FOWT for better understanding the motion of a floating wind turbine under a wide range of loading in Chapter 4.

2.5. Floating Platform Optimization for Offshore Wind Turbines

The improvements in the optimization to make FOWT systems less expensive and more reliable are ample. FOWT system optimization employing passive, semi-active, or active approaches is a trendy, ongoing topic for research worldwide. Improvements can be made to the turbine, such as modifying the wind turbine control system. For instance, blade pitch regulation for a turbine on land is considered too fast for a wind turbine installed offshore. It might induce negative damping at low frequencies creating transient vibrations throughout the tower (Larsen and Hanson, 2007). Geometrical modifications of the tower or RNA can also be checked to reduce aerodynamic forces that might cause fatigue on the floating platform. The tower of the baseline NREL wind turbine, for example, has its length truncated to minimize gyroscopic moments on the platform (Jonkman et al., 2009).

Another category is optimizing the substructure to mitigate hydrodynamic excitations. Stochastic wind and wave-induced platform tilt motions cause heavy loading on the turbine structure due to the massive inertia and gravitational forces implying a severe challenge on the design of FOWTs (Butterfield et al., 2005). This is more prominent the deeper the center of gravity (CoG) of the platform, e.g., spar-buoy. Such motions amplify tower top displacement when the platform inclines, causing severe fatigue and ultimate loads on the RNA, modifying yaw bearing loading, disrupting the gearbox lubrication distribution, and so on (Si et al., 2014). Therefore, the minimization of the platform's rotational DoF is crucial. Jiawen Li et al. (2014) studied a new floating platform that functions like a spar-buoy at lower water depths by placing a buoyancy tank at the top and ballast tank at the bottom to increase the metacentric height and provide great restoring moments. Their design is complemented by an active ballast system that alters the position of ballast water when wind speed and its directionality changes significantly. A different approach to reducing the resonant platform responses is installing buoyancy dampers (Moharrami and Tootkaboni, 2014) or tuned liquid column dampers (TLCD). TLCD dissipates the energy by letting a liquid in a U-shape tube(s)

flow from one end to another, passing through an orifice (Jaksic et al., 2015; Lee et al., 2006; Z. Zhang and Høeg, 2020).

Geometrical optimization of the floating platform is an essential aspect of FOWT design. To optimize the platform's hydrodynamics, the designer must relocate the natural periods to avoid resonant responses at the wave-dominated excitation region. This is accomplished by increasing the added mass in a particular DoF. Added mass is defined as the measurement of the additional inertia impeded by the surrounding fluid on the platform as it attempts to accelerate in that direction (Sarpkaya, 2010).

Supplementary extrusions in the platform serve to produce added mass in the heave direction, such as the application of heave plates. Sudhakar and Nallayarasu, (2014) experimentally and numerically investigated single and double heave plates and the effect of relative spacing between the plates on the performance of a spar-buoy platform. A similar parametric analysis for a heave plate mounted at a vertical cylinder for various heave diameter, gap values, and different Keulegan–Carpenter (KC) numbers is investigated by Zhu and Lim (2017). Their study revealed that the heave diameter is the governing parameter for the variation of added mass. Helical strakes – typically applied for spar-buoy platforms – utilize the same concept to reduce vertical platform motions (Ding et al., 2017). Added mass can also be incremented by modifying existing geometries. For example, Liu, et al., (2019) examined some variations of the DeepCwind semi-submersible platform configuration. The upper parts of the offset columns were inclined by various angles, which led to better performance in heave direction due to the increase of the entrapped water underneath the inclined columns.

Improvements in the mooring system can be a critical factor in the design of a FOWT system. Liu, et al. (2019) were capable of reducing the platform's excursion by implementing a multi-segmented mooring line configuration. Rodrigues et al. (2015) adopted an active triangular mooring system that alters the cables' length to optimize the position of the individual FOWT in a wind farm to avoid the wakes from other wind turbines. Chen et al. (2017) examined the influence of mooring parameters such as the mooring line numbers and fairlead position on the dynamic responses of a spar-buoy under the combined loading of wave, wind, and current. They realized that both the platform motion and mooring tensions change significantly. The final decision for choosing the optimal mooring type and mooring line numbers depends on economic and

engineering constraints. The introduction of clump masses at a specific location along the mooring cable reduces the tension at the expanse of lessening mooring stiffness and allowing the platform to drift to a greater extent (Ghafari and Dardel 2018; Liu, Yuangang, et al., 2019).

From the literature survey above, it is evident that a trade-off is inevitable in the process of optimization. Active and semi-active systems, whether for moorings, ballast control, or dynamic positioning, are quite effective, but their cost and maintainability entail a serious challenge. Adjustment in the mooring system to restrict the platform's behavior either increases the cable tension or the installation cost of extra mooring lines. Heave plates and helical strakes are the exceptions to the rule. Their side effects are minimal, but increasing the added mass has its limitations, and pushing the systems natural period too far might become more of a burden than an advantage. It is part of the solution indeed, but the literature seems to be missing a universal perspective for achieving a global optimization instead of local enhancements for mitigating fatigue loads on FOWT systems. Geometrical innovation in the field is restricted to simple parametric variations in already existing, O&G-inspired platforms (Karimirad and Michailides 2015; Lai et al., 2014; Liu, Zhou, et al., 2019). This study aims to fill this gap by introducing a novel, globally-optimized alternative floating platform for the application of offshore wind technology (see Chapters 6 & 7).

CHAPTER 3

RESEARCH METHODOLOGY: MODEL COMPONENTS & ASSUMPTIONS

3.1. Assumptions and Conventions

The aero-hydro-mooring dynamic of FOWT the system is simulated. Therefore, the FOWT system is assumed as a rigid body. Assumptions regarding various components of the numerical model are separately described in the next sections.

This study uses a fixed, right-handed axis system with its z-axis pointing upward. The point of origin has two conventions. Chapter 4 uses the same convention adopted in the OC5 study in which the origin O is defined as the point of intersection of the undisplaced tower centerline with the still-water level (SWL). The consecutive chapters take the undisplaced center of gravity $\overrightarrow{CoG} = (x_g, y_g, z_g)$ of the system as the origin O' to discern the independent motions of the body. The two origins are illustrated in Figure 3.1 for the semi-submersible design example. Platform motion is divided into three translational (surge X, sway Y, heave Z) and three rotational (roll RX, pitch RY, yaw RZ). Three of which are vertical, and therefore, intrinsically restorable due to gravity (heave, roll, pitch) while the horizontal others are not (surge, sway, yaw). Figure 3.1 illustrates the DoF convention in their positive directions. Note that the wind turbine is facing upwind (negative x-axis). The main wind and wave direction point to the positive x-direction. All load cases in this thesis obey these rules except when uni/multidirectionality is scrutinized in Chapter 4.

3.2. Model Components

The assessment of FOWT system is carried out using a numerical model that comprises three main components:

1- an in-house aerodynamic model accounting for simulating the forces and moments exerted on the blades of the wind turbine,

2- a hydrodynamic model simulating wave-induced diffraction and non-diffraction forces,

3- a dynamic mooring model solving for the effects of the mooring system on the platform.

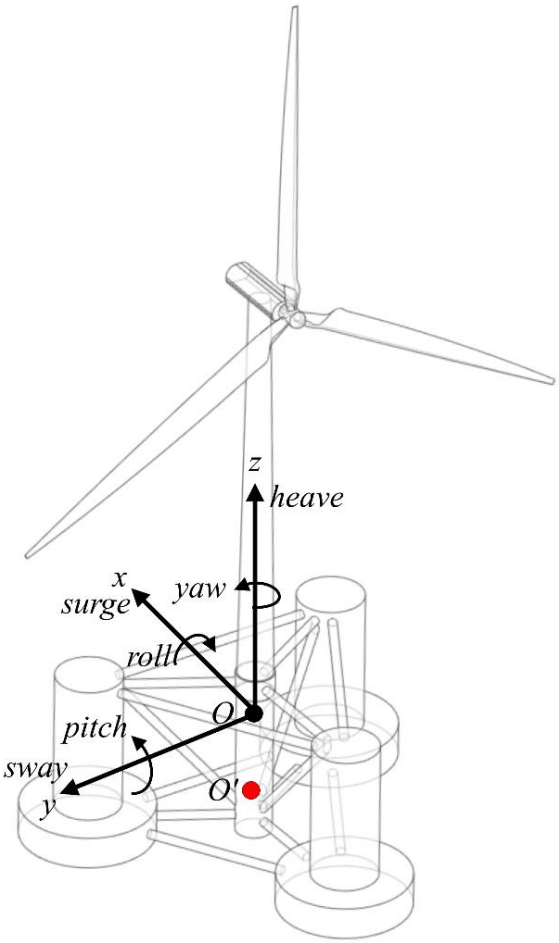

Figure 3.1: DoF conventions with the first convention of the origin point being deployed here.

ANSYS™ AQWA® package is used as the central element of the numerical simulation. One can use AQWA for the investigation of environmental loading effects on floating or fixed offshore structures. Analysis can be run in the frequency-domain (FD) for rapid evaluation of a particular system (useful for the initial stages of a new design) or in the more rigorous time-domain (TD) analysis to simulate real-time motion (ANSYS Inc., 2013). The global equation of motions for one structure in FD and TD respectively are written as:

$$[-\omega^2 M - i\omega C + K]U = F(\omega) \tag{3.1}$$

$$M\ddot{U} = F(t) \tag{3.2}$$

where M, C, and K are the 6×6 matrix of assembled structural mass and added mass, damping, and stiffness matrices, and F is the 6×1 matrix containing the combination of all external forces as a function of frequency ω or time t. It should be noted that in TD, AQWA uses a semi-implicit two-stage predictor-corrector integration scheme to solve for the displacement U and velocity $\dot{U}$ matrices.

3.2.1. Hydrodynamic Model

The hydrodynamic sub-model employs three-dimensional radiation/diffraction panel theory and Morison's equation. It can estimate the static and dynamic characteristics of free-floating or moored-floating system(s).

3.2.1.1. Ocean Waves

The system's motion in real-time can be simulated under regular waves (sinusoidal wave of constant amplitude and period) or irregular waves (a combination of a large number of sinusoidal waves distributed over a range of frequencies and directions), and current environmental loading.

1- Regular waves

A regular wave is sinusoidal with constant wave height H and period T. It is unrealistic. However, it provides real insights as to what type of response to expect under a given wave period T. All regular waves simulated in this study are assumed to be linear (Airy) progressive waves. Namely, the fluid is considered ideal, irrotational, incompressible, and inviscid. The ratio of wave height to water depth must be relatively small for this theory to be applicable. The flow is represented by a velocity potential Φ satisfying the Laplace equation. The wave surface elevation η is defined as:

$$\eta(x,t) = a\cos(kx - \omega t + \epsilon_0) \tag{3.3}$$

where;

$$k = \frac{2\pi}{L};\ \ \omega = \frac{2\pi}{T} \tag{3.4}$$

Here, a is the wave amplitude ε_0 is the initial phase, k is the wavenumber, and L is the wavelength. The dispersion relation and wave celerity c are as follows:

$$L = \frac{gT^2}{2\pi}\tanh kh \tag{3.5}$$

$$c = \frac{gT}{2\pi}\tanh kh \tag{3.6}$$

where g is the gravitational acceleration

2- Irregular waves

In this study, irregular waves are defined according to the Joint North Sea Wave Project (JONSWAP) spectrum, which is a modification of the Pierson-Moskowitz spectrum with an enhanced spectral peak. The definition of the spectrum $S(f)$ as a function of the significant wave height H_s and spectral peak period T_p is written as follows (Goda, 2010):

$$S(f) = \beta_{ij} H_s^2 T_p^{-4} \exp\left[-1.25\left(T_p f\right)^{-4}\right] \gamma^{\exp\left[-\frac{\left(T_p f-1\right)^2}{2\sigma^2}\right]} \tag{3.7}$$

in which

$$\beta_{ij} \cong \frac{0.0624\,(1.094 - 0.01915\ln\gamma)}{0.230 + 0.0336\,\gamma - 0.185(1.9+\gamma)^{-1}} \tag{3.8}$$

$$\gamma = 1\sim7, \qquad \sigma \cong \begin{cases} 0.07: & f \le f_p, \\ 0.09: & f > f_p. \end{cases} \tag{3.9}$$

where γ is the peak enhancement factor. Its value ranges between 1 and 7 with a mean of 3.3, as reported by Hasselmann et al. (1973). It is possible to get a wave energy spectrum in different shapes by changing γ as it controls the spectral peak sharpness. It is worth

mentioning that H_s is the average of the highest 1/3 of wave heights in the wave train defined by a zero-upcrossing method.

3.2.1.2. Hydrostatics of the Floating Body

To ensure vertical equilibrium positioning of a moored-floating body, all vertical forces applied must equal zero:

$$mg + F_B + N_c T_V = 0 \tag{3.10}$$

$$F_B = \rho_f g \nabla \tag{3.11}$$

where m is the overall structural mass of the system, F_B is the buoyancy force, N_c is the number of mooring cables attached to the platform, ρ_f is the density of the fluid, and T_V is the vertical component of the cable's tension. The volumetric displacement ∇ is computed by integrating over the submerged part of the platform at its undisplaced position:

$$\nabla = \int_{-d}^{0} A_{out}(z) \cdot dz \tag{3.12}$$

in which d is the draft of the submerged body and $A_{out}(z)$ is the cross-sectional area of the outer surface of the shell at depth z. From here, and assuming the cut water-plane area A_{wp} is constant for small vertical displacements, we can define the stiffness in the vertical direction k_{33} to be equal to:

$$k_{33} = \rho g A_{wp} + \Delta T_V \tag{3.13}$$

As the platform oscillates upward and downward, the first term on the right-hand side represents the resulting unbalanced buoyancy force and the second term is the addition or reduction in the vertical tension ΔT_V from the mooring lines as more or less of the catenary cable is left suspended. The first term, however, is the dominant part when the mooring system is catenary.

Only vertical equilibrium is not sufficient to ensure the static stability of the floating object. It must resist rotational dislocations as well. The restoring moment in pitch M_Y (and M_X for roll) induced by a rotation θ_2 (in radian) is defined:

$$M_Y = \left[\rho_f g \nabla \overline{GM} + k_{55_m}\right] \cdot \theta_2 \tag{3.14}$$

in which, k_{55_m} is mooring-induced additional pitch stiffness, and $\overline{GM}$ is the metacentric height:

$$\overline{GM} = BM + z_B - z_g \tag{3.15}$$

$$BM = I_{wp}/\nabla \tag{3.16}$$

where z_B is the vertical position of the center of buoyancy, z_g is the vertical position of the center of gravity, BM, represents the distance between the metacenter and the buoyancy center, and I_{wp} is the principal second moment of the water-plane area (see Figure 3.2).

Moorings are responsible for restoring the horizontal directions:

$$k_{11} = k_x = \frac{\Delta \sum T_H}{\Delta u_1}, \qquad k_{22} = k_y \frac{\Delta \sum T_H}{\Delta u_2} \tag{3.17}$$

where u_1 and u_2 are the excursion in surge and sway, respectively and k_x and k_y are the linearized resultant restoring stiffness from all the mooring lines. They can be found through tension-excursion relations where an offset is created in the desired direction (ΔX or ΔY), and the resulting unbalanced horizontal tensions are seen. The same concept can be applied to yaw as well. Finally, the coupled surge-pitch stiffness is given as:

$$k_{15} = k_{51} = k_x \cdot z_f \tag{3.18}$$

where z_f is the vertical location to the fairlead connection.

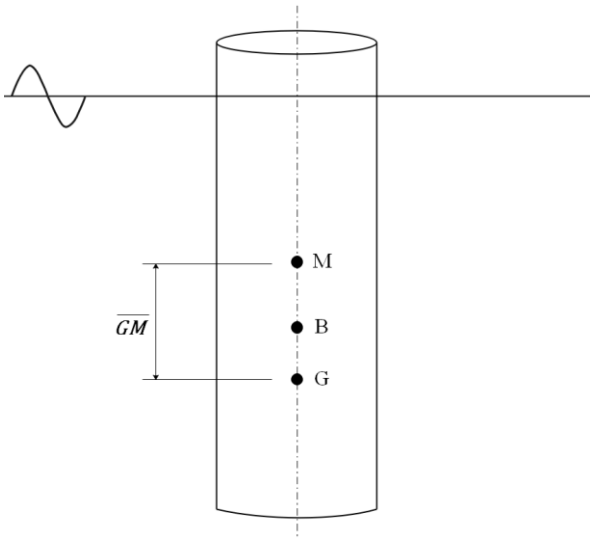

Figure 3.2: $\overline{GM}$ definition.

3.2.1.3. Hydrodynamic Linear Wave Forces

Wave-induced linear forces are categorized into active exciting wave forces and reactive inertial forces. Active forces comprise the direct incident wave force, also known as Froude-Krylov force, which is indifferent to the presence of the body, and diffraction force induced by the disturbance in the wave due to the presence of the body. The problem would have ended here if the body is to be fixed. However, floating bodies react to these excitations by 6-modal body movement creating the second type of forces - radiation forces. Fluid potential theories are frequently utilized for solving these two types of forces.

The mathematical model adopted in AQWA is concisely provided below (ANSYS Inc., 2013). Suppose the following velocity potential term defining the fluid flow field surrounding the floating platform:

$$\Phi\left(\overrightarrow{X}, t\right) = a\, \varphi\left(\overrightarrow{X}\right) e^{-i\omega t} \tag{3.19}$$

The space-dependent term $\varphi\left(\overrightarrow{X}\right)$ can be split into contributions from the incident wave φ_1, diffraction wave φ_d, and the body motion-induced radiation forces φ_{r_j}. Symbolizing the six-rigid body motion excited by a unit amplitude as follows:

$$x_j = u_j, \qquad j = (1,3) \tag{3.20}$$

$$x_j = \theta_j, \qquad j = (4,6)$$

the space-dependent potential due to active and reactive forces becomes:

$$\varphi(\overrightarrow{X})e^{-i\omega t} = \left[(\varphi_1 + \varphi_d) + \sum_{j=1}^{6} \varphi_{r_j} x_j\right] e^{-i\omega t} \tag{3.21}$$

Knowing the wave velocity potential, one can use Bernoulli's equation to solve for the first order hydrodynamic pressure distribution:

$$p^{(1)} = -\frac{\rho \partial \phi(\overrightarrow{X}, t)}{\partial t} = i\omega\rho\varphi(\overrightarrow{X})e^{-i\omega t} \tag{3.22}$$

Integrating the hydrodynamic pressure along the wetted surface S_0, the first order hydrodynamic wave forces and moments are expressed as follows:

$$F_j e^{-i\omega t} = -\int_{S_0} p^1 n_j dS = \left[-i\omega\rho \int_{S_0} \varphi(\overrightarrow{X})\, n_j dS\right] e^{-i\omega t} \tag{3.23}$$

where n_j is the j^{th} unit normal vector for the form:

$$\begin{aligned} (n_1, n_2, n_3) &= \overrightarrow{n} \\ (n_4, n_5, n_6) &= \overrightarrow{r} \times \overrightarrow{n} \end{aligned} \tag{3.24}$$

with $\overrightarrow{r} = \overrightarrow{X} - \overrightarrow{CoG}$ is the position vector of a point on the wetter surface w.r.t the position of the center of gravity of the floating body. The components of the total force in Eq. (3.23) are the j^{th} Froude-Krylov force of the incident wave:

$$F_{1_j} = -i\omega\rho \int_{S_0} \varphi_1(\overrightarrow{X}) n_j dS, \tag{3.25}$$

the j^{th} diffracting force due to the diffraction wave:

$$F_{d_j} = -i\omega\rho \int_{S_0} \varphi_d(\overrightarrow{X}) n_j dS, \tag{3.26}$$

and the j^{th} reactive, radiation force due to radiation wave caused by the k^{th} mode of motion:

$$F_{r_{jk}} = -i\omega\rho \int_{S_0} \varphi_{r_k}(\overrightarrow{X}) n_j dS \tag{3.27}$$

The Source Distribution Method is used as the linear hydrodynamic theory to govern the fluid-structure interaction (FSI) and distribute these forces among the diffracting panel of the body. For more details on this, the reader is referred to (Newman, 1978).

3.2.1.4. Hydrodynamic Second-Order Wave Forces

The Taylor series expansion of the velocity potential solution introduced above and of the hydrodynamic pressure reveals the second-order wave excitation forces:

$$p = -\frac{\rho\partial\Phi}{\partial t} - \frac{1}{2}\rho\nabla\Phi\cdot\nabla\Phi - \rho g Z = p^{(0)} + p^{(1)} + p^{(2)} \tag{3.28}$$

where

$$\begin{aligned} p^{(0)} &= -\rho g X_3^{(0)} \\ p^{(1)} &= -\rho g X_3^{(1)} - \rho\frac{\partial\Phi^{(1)}}{\partial t} \\ p^{(2)} &= -\frac{1}{2}\rho\left|\nabla\Phi^{(1)}\right|^2 - \rho\vec{X}^{(1)}\cdot\nabla\frac{\Phi^{(1)}}{\partial t} - \rho\frac{\partial\Phi^{(2)}}{\partial t} - \rho g X_3^{(2)} \end{aligned} \tag{3.29}$$

Integrating over the instantaneous wetted hull surface $S(t)$ the total fluid force and moment are of the form:

$$\begin{aligned} \overrightarrow{F}(t) &= -\iint_{S(t)} p\vec{N}ds \\ \overrightarrow{M}(t) &= -\iint_{S(t)} p[(\overrightarrow{X} - \overrightarrow{CoG})\times\vec{N}]ds \end{aligned} \tag{3.30}$$

Considering forces only, Pinkster, (1980) formulated the low-frequency second-order force in time-domain as the summation of five components:

$$\overrightarrow{F}^{(2)}(t) = \iint_{S_0} \left(\rho \frac{\partial \Phi^{(2)}}{\partial t}\right) \vec{n} dS + \oint_{WL} \left(-\frac{1}{2}\rho g\left(\eta^{(1)}\right)^2\right) \vec{n} dl + \frac{1}{2}\rho \iint_{S_0} \left|\nabla \Phi^{(1)}\right|^2 \vec{n} dS + \rho \iint_{S_0} \left(\vec{X}^{(1)} \cdot \frac{\nabla \partial \Phi^{(1)}}{\partial t}\right) \vec{n} dS + \vec{\alpha}^{(1)} \times \vec{F}^{(1)} \tag{3.31}$$

where $\vec{\alpha}^{(1)}$ denotes the linearized rotation matrix of the center of gravity of the body. These components are, respectively:

1- contribution of second-order potentials, this term is the most difficult to compute.

2- first-order relative wave elevation,

3- first-order pressure drop,

4- pressure due to the product of gradient of first-order pressure and first-order motion

5- contribution of first-order angular motion and inertial forces

Eq. (3.31) can be rewritten in the frequency domain by considering pairs of sinusoidal waves of frequencies (ω_i;ω_j), amplitudes of $(a_i; a_j)$, and phase shifts of $(\varepsilon_i; \varepsilon_j)$:

$$F_{i,j}^{(2)}(t) = Re\left\{\sum_i \sum_j a_i a_j QTF_{ij}(\omega_i; \omega_j) e^{-i[\omega_i - \omega_j]t + \varepsilon_i - \varepsilon_j}\right\} \tag{3.32}$$

in which QTF is the quadratic transfer function. The real part of QTF_{ij} describes the (i^{th}, j^{th}) amplitude of the second-order force per unitary pair of waves amplitude. When $\omega_i = \omega_j$, the corresponding wave force is constant mean drift force and the difference frequency $\omega_i - \omega_j$ brings forth the slowly-varying motions. Following Pinkster's simplification, the second-order force component is given as:

$$F_{i,j}^{(2)} = Re\left\{F_{i,j}^{(2)} e^{-i[\omega_i - \omega_j]t + \varepsilon_i - \varepsilon_j}\right\}$$
$$F_{i,j}^{(2)} = f_{i,j} F^{(1)}(k_i - k_j) \tag{3.33}$$

$$f_{i,j} = \frac{a_i a_j A_{ij}(\omega_i - \omega_j)}{g}$$

in which $F^{(1)}(k_i - k_j)$ is the first-order wave exciting force caused by a regular wave with the wavenumber $(k_i - k_j)$ of a unit wave amplitude and can be calculated using Eq. (3.23), while A_{ij} is a frequency and water depth dependent coefficient:

$$A_{ij} = \frac{1}{2} g^2 \frac{B_{ij} + C_{ij}}{(\omega_i - \omega_j)^2 - (k_i - k_j) g \tanh(k_i - k_j) h},$$

$$B_{ij} = \frac{k_i^2}{\omega_i \cosh^2 k_i h} - \frac{k_j^2}{\omega_j \cosh^2 k_j h}, \tag{3.34}$$

$$C_{ij} = \frac{2 k_i k_j (\omega_i - \omega_j)(1 + \tanh(k_i h) \tanh(k_j h))}{\omega_i \omega_j}$$

3.2.1.5. Morison's Equation

In the previous two sections, the first order and second-order active and reactive wave exciting and inertial forces are covered. The other type is viscous force, which becomes crucial for slender structures or when large waves occur. One way to categorize the kind of effects on a body is to use the characteristic diameter D to the wavelength L ratio. If this ratio is less than 0.2, the dominance of diffraction forces diminishes, and the drag force becomes more important. The drag component acting on a unit length on a submerged cylinder is proportional to the square of the relative velocity between the body $\dot{u}_j$ at that strip and the wave-induced water particle $\dot{q}$. For translational modes of motion $(j = 1,2)$ Morison force is the summation of a drag component and inertia component:

$$dF_M = \frac{1}{2} \rho_f D C_d |\dot{q} - \dot{u}_j| (\dot{q} - \dot{u}_j) + C_m \rho_f \frac{\pi D^2}{4} \ddot{q} - (C_m - 1) \rho A \ddot{u}_j \tag{3.35}$$

where $C_m = (1 + C_a)$ is the inertia coefficient and C_a is the added mass coefficient.

3.2.2. Aerodynamic Model

An in-house code is built to simulate the aerodynamic-induced forces on the turbine and translate them to the floating platform. The aerodynamic sub-model is an unsteady BEM-based model, which is a combination of the Blade Element Theory (BET) and Momentum Theory (MT). The original description of the theory by Glauert (1935) served to investigate the performance of a rotor with an infinite number of blades. The approach since then has evolved, and more ad-hoc corrections are added to it to enhance its accuracy and relax its assumptions.

Figure 3.3 is an illustration of forces acting on a typical airfoil. The elementary aerodynamic forces p_n and p_t at the radial position r are:

$$p_n = 1/2\rho_a U_{rel}^2 c_r \cdot c_n \tag{3.36}$$

$$p_t = 1/2\rho_a U_{rel}^2 c_r \cdot c_t \tag{3.37}$$

where ρ_{air} is air density $= 1.225\ kg/m^3$, U_{rel} is the relative velocity, c_r is the chord length and c_n and c_t are the projection of lift coefficient $C_l(\alpha)$ and drag coefficient $C_d(\alpha)$

$$c_n = C_l(\alpha)\cos\phi + C_d \sin\phi\,, \qquad c_t = C_l \sin\phi + C_d \cos\phi \tag{3.38}$$

where ϕ is the flow angle:

$$\phi = \tan^{-1}\left(\frac{U_n}{U_t}\right) \tag{3.39}$$

such that U_n and U_t are the normal and tangential velocities. Together, they form the relative velocity:

$$\begin{gathered} U_{rel} = U_n^2 + U_t^2 \\ U_n = U_0(1 - a_B), \qquad U_t = \Omega(1 + a_B') \end{gathered} \tag{3.40}$$

in which $a_B, a_B{}'$ denote the axial and tangential induction factors, U_0 represents the undisturbed wind velocity, and Ω is the angular velocity of the rotor. C_l and C_d are

typically given as a function of the angle of attack α which is the difference between the flow angle and the sum of the local twist angle ϵ, and the blade pitch angle θ_p:

$$\alpha = \phi - (\epsilon + \theta_p) \tag{3.41}$$

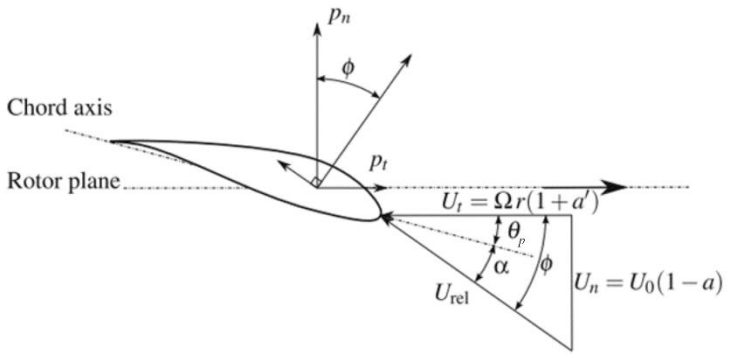

Figure 3.3: Cross-sectional view of an airfoil and velocity components acting on it.

The local thrust dT_{BET} and torque dQ_{BET} from the BET theory is computed as follows:

$$dT_{BET} = \frac{1}{2}\rho_a U_{rel}^2 \sigma_r dA_r \cdot c_n, \qquad dQ_{BET} = \frac{1}{2}\rho_a U_{rel}^2 \sigma_r dA_r c_r \cdot c_t \tag{3.42}$$

where $\sigma_r = N_B c_r / 2\pi r$ is the rotor solidity, and dA_r is the annular area at the radial position r.

BET theory is applied to a finite number of blades, while MT is inherently derived for an infinite number of blades. Due to this fundamental difference, the induction factors ought to be corrected by a tip-loss factor F_{TL} when substituted in the momentum equation:

$$F_{TL} = \frac{2}{\pi}\cos^{-1} e^{-f}, \qquad f = \frac{N_B}{2}\frac{R - r}{r \sin\phi} \tag{3.43}$$

where N_B is the number of rotor blades, and R is the rotor radius. And the resulting local thrust dT_{MT} and torque dQ_{MT} from MT becomes:

$$dT_{MT} = \frac{1}{2}\rho_a U_0^2 dA\,[4a_B F_{TL}(1-a_B)],$$
$$dQ_{MT} = \frac{1}{2}\rho_a U_0^2 r dA\,[4a'_B F_{TL}(1-a_B)\lambda_r] \tag{3.44}$$

Upon equalizing the local aerodynamic from the two theories, i.e., Eq. (3.42) with Eq. (3.44), and using thrust and torque coefficients C_t, C_q instead of forces, one can reach a solution for the induction factors:

$$a_B = f\left(C_{t,BET}\right), \qquad a'_B = \frac{C_{q,BET}}{4F_{TL}(1-a_B)\lambda_r}$$
$$C_{t,BET} = \frac{U_{rel}^2}{U_0^2}\sigma_r \cdot c_n, \qquad C_{q,BET} = \frac{U_{rel}^2}{U_0^2}\sigma_r \cdot c_t \tag{3.45}$$

where λ_r is the speed ratio at the radial position r. The $a_B - C_t$ relation chosen for this study is polynomial of the form:

$$a = k_0 + k_1 C_t + k_2 C_t^2 + k_3 C_t^3 \tag{3.46}$$

Using the fitted coefficients in Branlard (2017):

$$k_0 \approx 0, \qquad k_1 = 0.251, \qquad k_2 = 0.054, \qquad k_3 = 0.089 \tag{3.47}$$

To reach a more realistic representation of aerodynamic forces, the following dynamics are included in the system:

1- Dynamic Wake/Inflow

Any modification in the rotor loading causes a change in the wake and, therefore, the induced velocities. The ability to reach a new steady-state under a new loading happens dynamically. In other words, a steady solution assumes the system is always in equilibrium (quasi-static solution). When introducing a dynamic inflow, an exponential decay between the quasi-static solution and the current state rises. The model is described in the form of two first-order differential equations as follows (Hansen, 2008):

$$W_{qs} + 0.6\tau_1 \frac{dW_{qs}}{dt} = W_{int} + \tau_1 \frac{dW_{int}}{dt}, \qquad W_{int} = W + \tau_2 \frac{dW}{dt} \tag{3.48}$$

where W_{qs} is the quasi-static induction, W is the actual induction at the rotor, and W_{int} is an intermediate term between the actual and the quasi-static solution. As for time constants, they take the form:

$$\tau_1 = \frac{1.1}{1 - 1.3\min(a, 0.5)}\frac{R}{U_0}, \qquad \tau_2 = \left(0.39 - 0.26\left(\frac{r}{R}\right)^2\right)\tau_1 \tag{3.49}$$

In the propagation of time by Δt timestep, the value of the current W_{qs} is a function of its past value:

$$\underline{H} = W_{qs}^t + 0.6\,\tau_1\left(W_{qs}^t - W_{qs}^{t-1}\right) \tag{3.50}$$

Through $\underline{H}$, the intermediate value is found:

$$W_{int}^t = \underline{H} + \left(W_{int}^{t-1} - \underline{H}\right)e^{-\frac{\Delta t}{\tau_1}}, \qquad W^t = W_{int}^t + (W^{t-1} - W_{int}^t)e^{-\frac{\Delta t}{\tau_2}} \tag{3.51}$$

2- Dynamic Stall

Changes in the boundary layer of an airfoil induced by wind shear, tower passage, or frequent motion of the turbine entail dynamic effects that are reflected as a change in the polar data of an airfoil. The model of Øye is followed here (Øye, 1991) in which an interpolation scheme of the airfoil data between a fully separated flow case and an entirely inviscid flow is introduced:

$$C_l(\alpha, t) = f_s(t)C_{l,inv}(\alpha) + \left(1 - f_s(t)\right)C_{l,fs}(\alpha) \tag{3.52}$$

where the separation function f_s acts as a buffer as time progresses. The previously mentioned extreme cases are represented by their lift coefficients in Eq. (3.52); $C_{l,inv}$ for an inviscid flow, and $C_{l,fs}$ for a fully separated one. The inviscid lift coefficient is determined as follows:

$$C_{l,inv} = C_l \sin(\alpha - \alpha_0) \tag{3.53}$$

in which α_0 is that angle attack when the steady lift coefficient is zero. As for the second case, an engineering model to derive $C_{l.fs}$ from the original polar data consisting of a

linear region and a smooth transition back to the original steady C_l at a higher angle of attack. The slope of the linear region is given by:

$$s_{fs} = \frac{1}{2} C_{l,\alpha} \tag{3.54}$$

The angle at which the fully separated curve matches the steady lift curve and becomes equal to C_{l_1} is noted as α_{merge} and is chosen to be $\pm 35^{\circ}$. The angle at which the linear region reaches this mutual value at a lower angle of attack is noted α_1 and given by:

$$\alpha_1 = \alpha_0 + \frac{C_{l_1}}{s_{fs}} \tag{3.55}$$

The extent of the transition region $\Delta\alpha$ is defined as the angle difference between the end of the linear part and the merging point or the angle difference between α_1 and α_0, whichever is minimum. For angles above α_0, the fully separated lift coefficient is obtained according to the following formula:

$$C_{l,fs} = \begin{cases} s_{fs}(\alpha - \alpha_0), & \alpha < \alpha_1 - \Delta\alpha \\ s_{fs}(\alpha - \alpha_0) - s_{fs}\dfrac{(\alpha - \alpha_1 + \Delta\alpha)^2}{4\Delta\alpha}, & \alpha < \alpha_1 + \Delta\alpha \\ C_{l_1}, & \alpha < \alpha_{merge} \\ C_l, & otherwise \end{cases} \tag{3.56}$$

For angles lower than α_0, the same approach is followed. Figure 3.4 displays an example of a dynamic stall model.

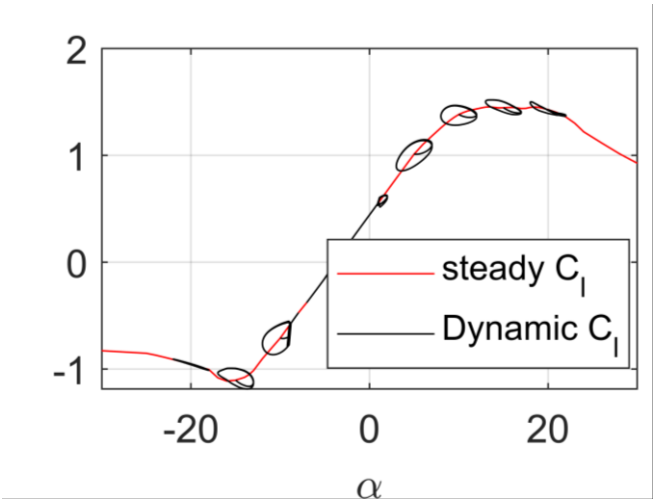

Figure 3.4: Dynamic stall model example.

3- Wind shear

Wind velocity close to the surface boundary is slower than the wind upward. Knowing two free flow wind velocities at different heights ($z_1; z_2$) is sufficient to determine the complete wind profile via the power law (Landberg, 2016):

$$ά = \frac{\ln[U_0(z_1)/U_0(z_2)]}{\ln[z_1/z_2]} \tag{3.57}$$

where ά denotes the wind shear exponent.

4- Tower Shadowing

The tower acts as a source in the velocity potential solution deviating the streamlines of the flow around it, subsequently adding a lateral component of the inflow wind like the one shown in Figure 3.5. Consequently, the upstream velocity encountered by the airfoils is altered (Hansen, 2008):

$$V_{0,r} = U_0\left(1 - \left(\frac{D_T(z)}{2r}\right)^2\right)\cos\theta\,, \qquad V_{0,y} = -V_{0,r}\sin\theta - V_{0,\theta}\cos\theta \tag{3.58}$$

$$V_{0,\theta} = -U_0\left(1 + \left(\frac{D_T(z)}{2r}\right)^2\right)\sin\theta\,, \qquad V_{0,x} = V_{0,r}\cos\theta - V_{0,\theta}\sin\theta \tag{3.59}$$

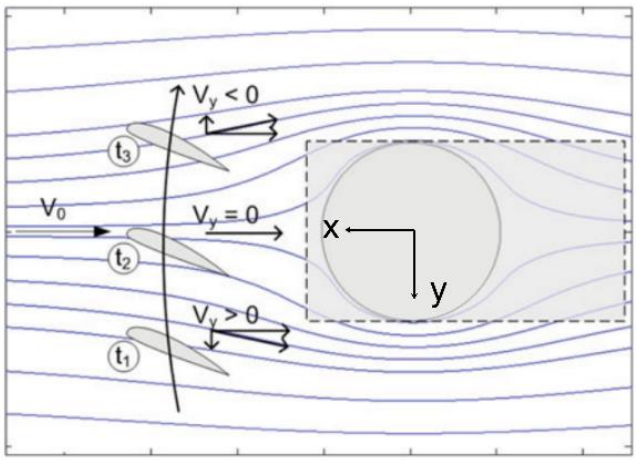

Figure 3.5: Flow deviation in proximity to the turbine tower.

(Source: Branlard, 2017)

The radial position of the blades must always be known in the global fixed reference to capture the tower shadow effect. Figure 3.6 is a demonstration of how the 5MW wind turbine casts a shadow on its blades along the blade length. Note that at the rotor tip, the wind shear and tower shadow effects are more dominant than the points close to the blade's root.

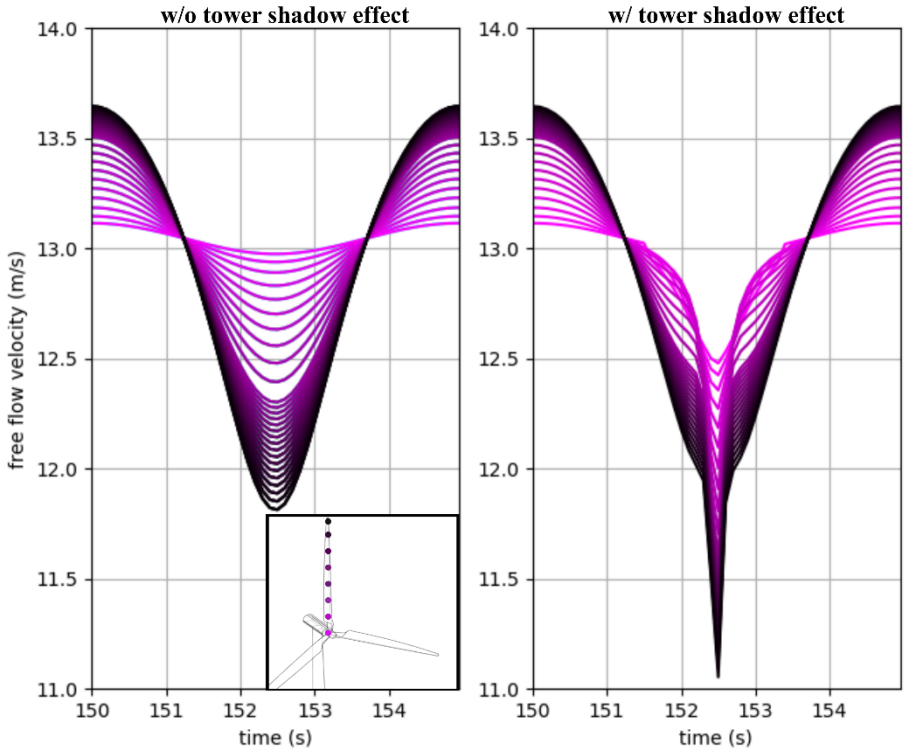

Figure 3.6: Wind shear and tower shadow effect on the free flow velocity encountered by a blade on the 5MW wind turbine (dark colors denote points close to the blade tip).

Briefly, the aerodynamic algorithm follows the following procedure:

1- The undisrupted wind velocity that is influenced by the platform motion, wind shear, tower shadow, and previous induction velocities is projected to the airfoil cross-sections.

2- The normal and tangential velocities U_n and U_t are solved for.

3- The flow angle ϕ and the tip-loss factor F_{TL} is computed.

4- The angle of attack $\alpha = \phi - (\epsilon + \theta_p)$ and its dependents C_l and C_d coefficients are found (dynamic stall is applied here)

5- c_n, c_t, C_t, C_q are computed, and then the axial induction velocities.

6- Quasi-static induction values are estimated with the application of high-thrust correction

7- The dynamic wave model is applied to get the actual induction velocities.

3.2.3. Mooring Model

The mooring system can be modeled using a quasi-static model or a dynamic model. AQWA has both options. The former is used for the initial design stage, and the latter is utilized when a time-domain analysis is conducted.

A quasi-static solution ignores the hydrodynamic drag and inertia forces acting on the cable. Hence, the force acting on the platform from the mooring lines in the j^{th} mode is written as:

$$F_j^{lines} = F_j^{lines,0} - k_{jj_m} \cdot \dot{x}_j \tag{3.60}$$

such that $F_j^{lines,0}$ is the net force acted by the mooring cables on the platform at its undisplaced position. J.M. Jonkman (2007) formulated the analytical solution of an elastic catenary cable suspended in the fluid between the anchor and the fairlead. When a portion of the cable lies on the seabed, and if the cable's physical characteristics are given, then the two unknowns – the horizontal and vertical tension at the fairlead ($T_H; T_V$) can be solved for through these equations (origin here is at the anchor position):

$$x_f(T_H, T_V) = L_c - \frac{T_V}{\omega} + \frac{T_H}{\omega} \sinh^{-1} \frac{T_V}{T_H} + \frac{T_H L_c}{EA} \tag{3.61}$$

$$z_f(T_H, T_V) = \frac{T_H}{\omega}\left[\sqrt{1 + \left(\frac{T_V}{T_H}\right)^2} - 1\right] + \frac{1}{2EA}\left(\frac{T_V^2}{\omega}\right) \tag{3.62}$$

in which the first two terms of Eq. (3.61) represent the laid length $L_B = L_c - T_V/\omega$ where L_c is the cable's length. x_f and z_f are the horizontal and vertical coordinate of the fairlead position, EA is the axial stiffness of the mooring cable, and ω is its weight per unit length.

When the cable dynamics are solved for, the mooring is discretized, as seen in Figure 3.7. Each portion is dealt with as a Morison element over which hydrodynamic wave forces are projected. A single part is shown in Figure 3.8. Neglecting bending stiffness, the equation of motion of an element i is given by:

$$\frac{\partial \overrightarrow{T}}{\partial s_e} + \frac{\partial \vec{V}}{\partial s_e} + \vec{\omega} + \overrightarrow{F_h} = m\frac{\partial^2 \vec{R}}{\partial t^2} \tag{3.63}$$

where $\vec{V}$ and $\vec{R}$ are the shear force vector and position vector at the initial node of the element, $\Delta s_e = \vec{R}_{j+1} - \vec{R}_j$, is the length of the Morison element, m is the structural mass per unit length, and $\overrightarrow{F_h}$ is the combination of the hydrodynamic forces. Tension vector $\vec{T}$ is a function of the axial stiffness of the cable:

$$T = EA\varepsilon \tag{3.64}$$

with ε being the axial strain.

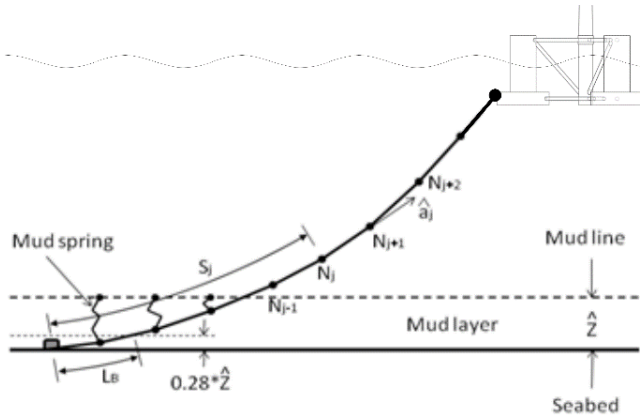

Figure 3.7: Cable discretization and touchdown point.

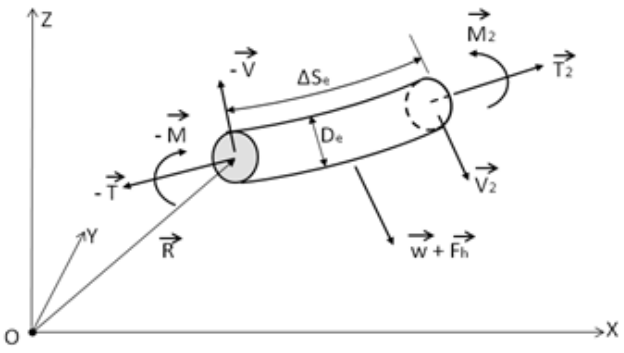

Figure 3.8: Single Morison element.

When applying the appropriate boundary conditions, the dynamic response of the cable is solved numerically by using Lump-Mass model. As for the hydrodynamic forces, the contribution from wave exciting forces is not included. The time-dependent hydrodynamic forces consist of the buoyant force F_B, drag force F_d, and inertial forces:

$$F_h = F_B + F_d - m_a\left[\vec{a}_j, \vec{a}_{j+1}\right]^{\mathrm{T}} \tag{3.65}$$

where m_a is the elementary added mass, and $\vec{a}_j$ is the acceleration at the j^{th} node. Drag forces are calculated just as described in section 3.2.1.5 only without the wave kinematics contribution to the relative velocity.

The seabed exerts a reaction force on the portion of the cable resting on the ground. The cable is said to be laid once the touchdown point reaches below 28% of the mud layer (see Figure 3.8). Suppose a node j has a position $\vec{R} = (x_j, y_j, z_j)$ the reaction force F_{zj} is modelled as a spring and can be written as:

$$F_{zj} = \begin{cases} 0, & z_j > h + \hat{z} \\ \dfrac{m'g}{\hat{z}}\left[d + z_j + \dfrac{\hat{z}}{pi}\sin - \dfrac{\pi\left(h + z_j\right)}{2\hat{z}}\right], & z_j \le h + \hat{z} \\ \dfrac{m'g}{\hat{z}}\left[\hat{z} + 2\left(h + z_j\right)\right], & z_j \le h \end{cases} \tag{3.66}$$

where m' is the net mass, including buoyancy.

3.3. Sub-model coupling

All the sub-models above are fully coupled. Physical information are consistently shared between the codes at each timestep. AQWA package is in charge of running the hydrodynamic and mooring models. The in-house aerodynamic code is written in Python language and is linked to AQWA by an external Dynamic Link Library (.dll) file.

To solve for the body acceleration in Eq. (3.2), the integration in time-domain is carried out through a 2-stage predictor-corrector approach. The external routine is called forth at both stages, but the aerodynamics output (old-time values to be used in successive timestep) are stored at the second stage. Given an initial condition, the predictor stage solves for the intermediate position and velocities:

$$\dot{U}^*(t+\Delta t) = \dot{U}(t) + \ddot{U}(t)\Delta t,$$
$$U^*(t+\Delta t) = U(t) + \dot{U}\Delta t + \frac{1}{2}\ddot{U}(t)\Delta t^2 \tag{3.67}$$

At the second stage, the position, and velocity-dependent forces are substituted back to Eq. (3.2) to solve for the intermediate acceleration at the new timestep $\ddot{U}^*(t+\Delta t)$ and the final position and velocity values are determined:

$$\dot{U}(t+\Delta t) = \dot{U}(t) + \frac{\ddot{U}(t) + \ddot{U}^*(t+\Delta t)}{2}\Delta t$$
$$U(t+\Delta t) = U(t) + \dot{U}\Delta t + \frac{2\ddot{U}(t) + \ddot{U}^*(t+\Delta t)}{6}\Delta t^2 \tag{3.68}$$

The platform is then moved to its new position, and time is incremented by $1\Delta t$.

Figure 3.9, along with Figure 3.10, summarizes the entire methodology followed in this thesis. The two figures use off-page references (A & B) and on-page references (C & D).

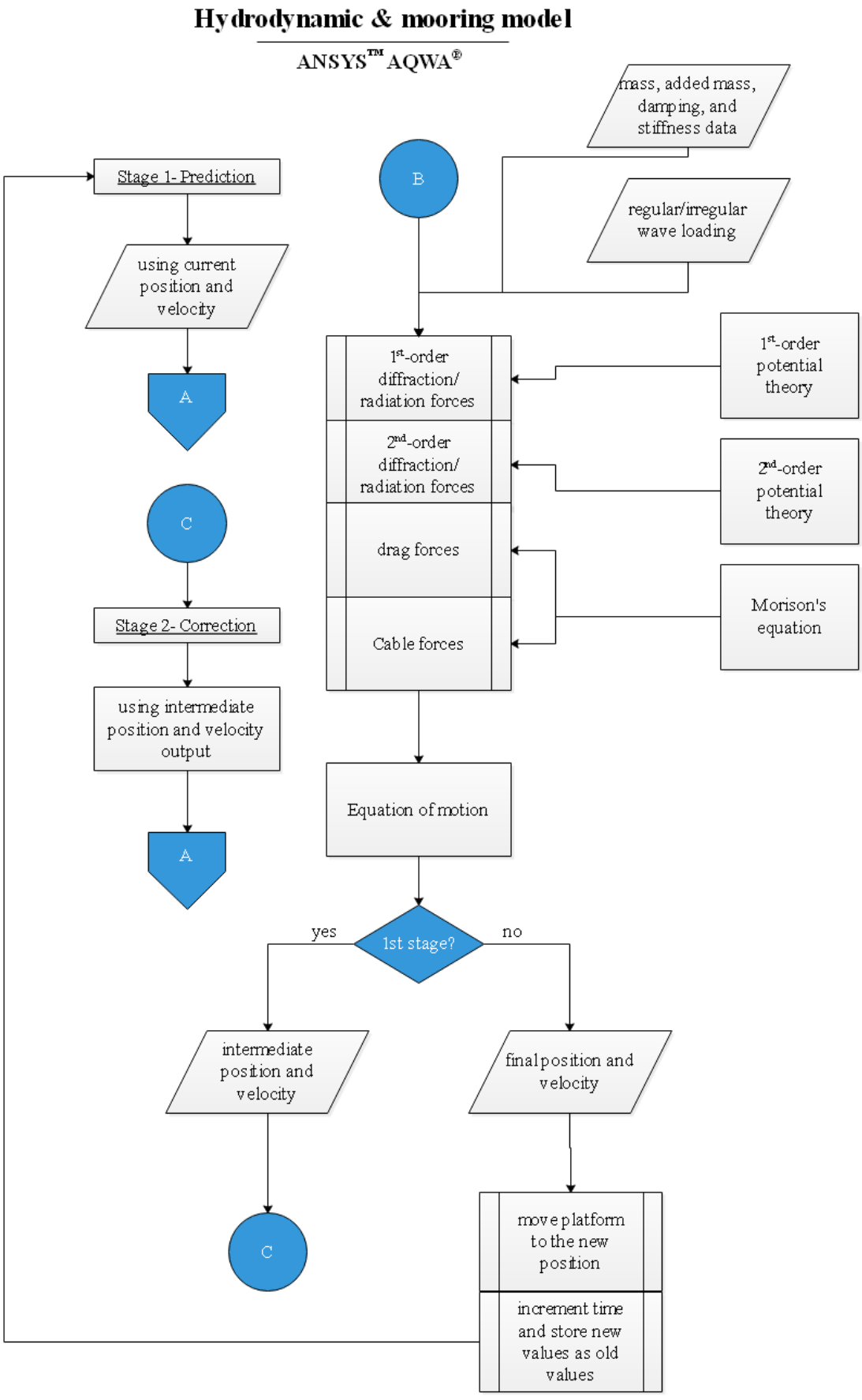

Figure 3.9: Hydrodynamic and mooring model using TD 2-stage integration scheme.

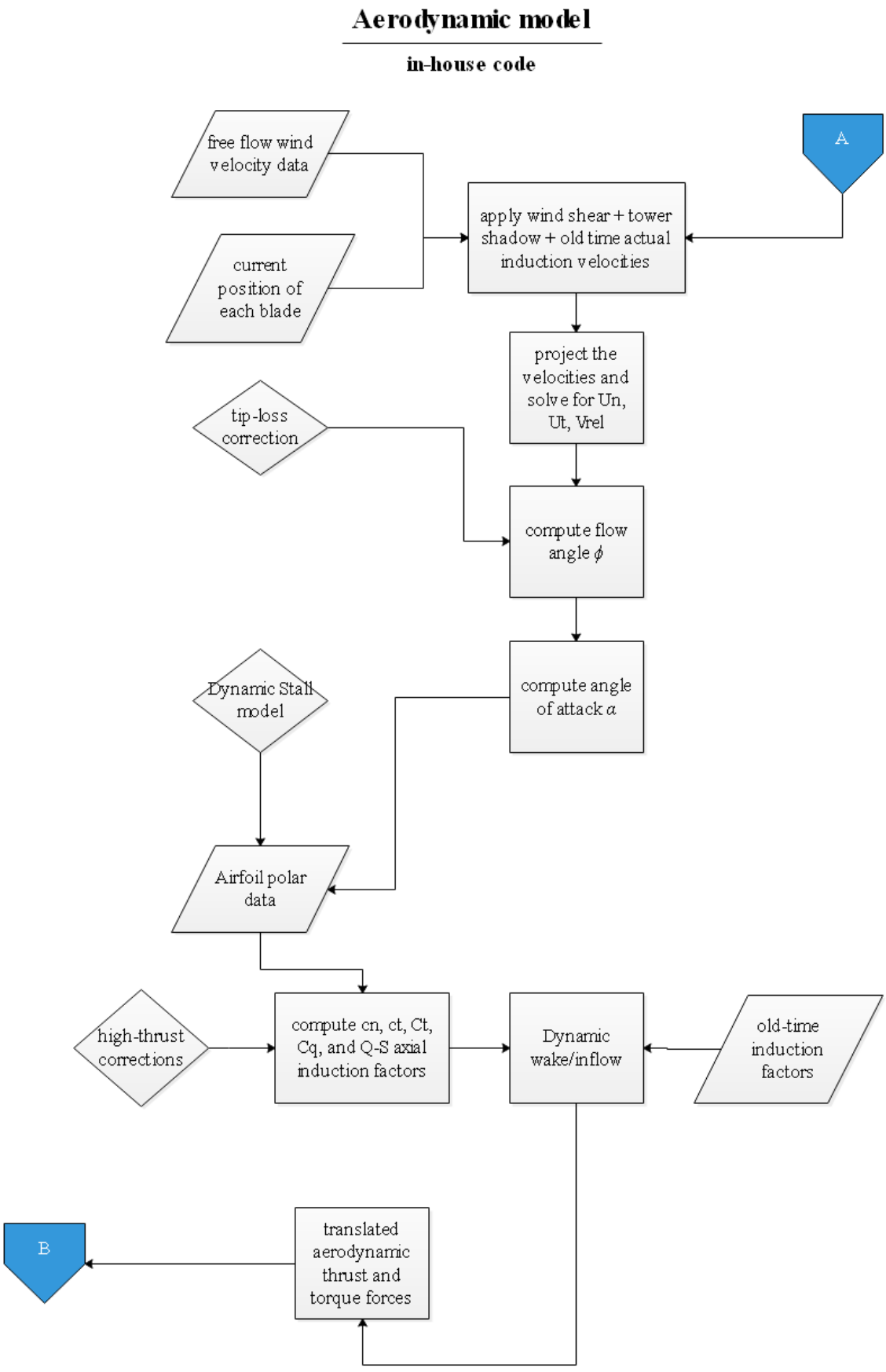

Figure 3.10: Aerodynamic model flowchart.

3.4. Post-Processing Techniques

Massive data must be treated with caution. Commonly used mathematical and statistical methods are adopted in this study. Some loading conditions entail TD analysis, while others are stochastic that an FD analysis must be sought for the data to become appreciable. Data might need some repair after exporting. For instance, during initiation, some amplification in the LF responses might occur even if the loading is fully harmonic. Regular waves can be ramped at the beginning of a simulation run to circumvent this issue. The loading starts at zero initially and gradually increases until it reaches the designated value. The time of ramping is usually chosen to be a value of one wave period. Another solution is to simulate more than the specified duration and post-processingly offset the data to be studied by that amount. This is also helpful to give the system enough time to reach its static value under a given loading.

Under a regular wave loading, Comparisons are conducted by calculating the Response Amplitude Operators (RAO), which is the ratio of the response amplitude to the wave amplitude in a given mode j:

$$RAO_j = \frac{x_{j_{max}} - x_{j_{min}}}{2a} \tag{3.69}$$

In irregular waves only or with wind, the TD response is converted into an FD utilizing Fast Fourier Transform (FFT) to obtain the power spectrum density (PSD) of a particular reaction. The smoothing and windowing parameters are equal between all numerical models and the experiments. To discern a low-frequency excitation from a wave-frequency one, the PSD is divided at the frequency with the lowest energy between the natural frequency and the wave frequency (cutoff frequency) employing low-pass and high-pass 6th-order Butterworth filtering (see Figure 3.9). Then, the amplitude of each response is computed for each portion as follows:

$$a_{FD} \approx 4.00 \times \sqrt{m_0} \tag{3.70}$$

where m_0 is the zeroth moment defined as the area under the portion of the spectrum desired.

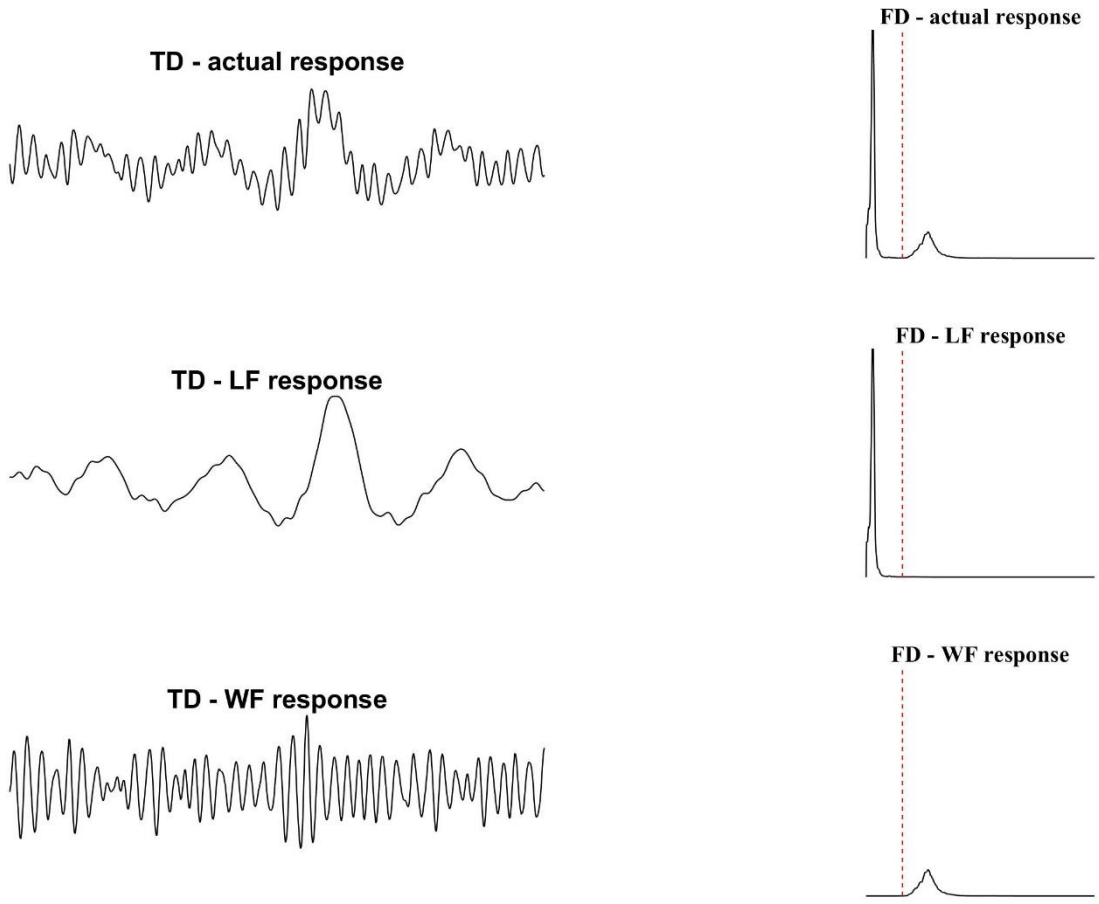

Figure 3.11: Low-pass and high-pass filtering example and its reflection in the time domain. The red, dashed line is the cutoff frequency.

Tension responses are occasionally checked for snap loading. A snap load is said to occur when the platform drifts toward the cable, rendering it slack for a moment until it moves the other direction creating a sudden restrain in the mooring line leading the tension to reach high peaks. The identification methodology of a snap load is the same as the one reported in (Hsu et al., 2017). Briefly, it is based on the definition by (DNV-GL, 2011) that the occurrence of a snap load is linked with the dynamic tension exceeding 90% the static tension and that it is preceded by unloading the cable and then sudden re-loading. Based on that, the snap event is initiated when the tension falls below the slack tension threshold (10% of the pretension value), followed by a local maximum above the pretension value. Applying this minimum-based criterion into the zero-up-crossed tension response gives the number of snap loads. Figure 3.12 portrays an example of a tension record illustrating a sequence of snap load events. Note that a period of a snap load event is usually smaller than the ordinary.

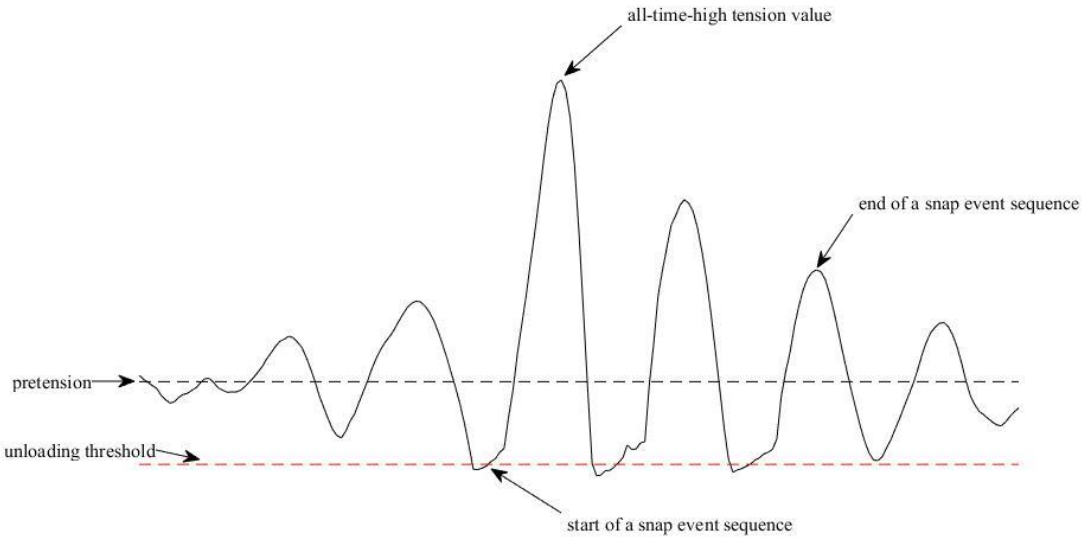

Figure 3.12: Snap load event example.

CHAPTER 4

NUMERICAL MODELING OF DEEPCWIND SEMI-SUBMERSIBLE FLOATING OFFSHORE WIND TURBINE

This chapter deals with the calibration and validation of the dynamic models described in the previous sections by comparing the current numerical model to the physical model data generated for the OC5 campaign project and the associated codes developed by various institutions. It is proceeded by a full description of the wind turbine and the floating system used for testing.

4.1. Wind Turbine Definition

The 5-MW rated baseline wind turbine designed by NREL has its gross properties described by Jonkman et al. (2009) and is described in Table 4.1. The blades are discretized, as shown in Table 4.2, and the mesh is increased closer to the tip for better accuracy.

Table 4.1: Gross properties of the wind NREL 5 MW baseline wind turbine.

Rating	5 MW
Rotor Orientation, Configuration	Upwind, 3-blades
Rotor diameter	126 m
Hub diameter	3 m
Hub height	90 m
Cut-in, Rated, Cut-Out wind speed	3 m/s, 11.4 m/s, 25 m/s
Cut-in, Rated rotor speed	6.9 rpm, 12.1 rpm
Overhand, shaft Tilt, precone	5 m, 0°, 0°
Rotor mass	110 t
Nacelle mass	240 t
Tower mass	347.460 t

Table 4.2: Blade distributed aerodynamic characteristics.

Radius (m)	Twist (deg.)	Chord length (m)	Airfoil type (modeled)
2.87	13.31	3.54	Cylinder
5.60	13.31	3.85	Cylinder
8.33	13.31	4.17	Cylinder
11.75	13.31	4.56	DU40
15.85	11.48	4.65	DU35
19.95	10.16	4.46	DU35
24.05	9.01	4.25	DU35
28.15	7.79	4.01	DU30
32.25	6.54	3.75	DU25
36.35	5.36	3.50	DU25
40.45	4.19	3.26	DU21
44.55	3.12	3.01	DU21
45.62	2.90	2.94	NACA64
46.69	2.69	2.88	NACA64
47.75	2.49	2.81	NACA64
48.82	2.29	2.75	NACA64
49.89	2.08	2.69	NACA64
50.96	1.88	2.63	NACA64
52.02	1.67	2.56	NACA64
53.09	1.46	2.50	NACA64
54.16	1.25	2.43	NACA64
55.23	1.05	2.37	NACA64
56.29	0.84	2.30	NACA64
57.36	0.64	2.24	NACA64
58.43	0.45	2.15	NACA64
59.50	0.29	2.00	NACA64
60.56	0.17	1.77	NACA64
61.63	0.11	1.42	NACA64

In Figure 4.1, polar data are displayed for all NREL 5-MW airfoil geometries. It is worth mentioning that Goupee and Kimball (2015) adjusted these data to calibrate the

performance-matching scaled wind turbine in their test model. Instead of using six different airfoils, they used one airfoil (AG04 Mod) to facilitate the calibration process. Their airfoil data are used in this chapter, and the original airfoil data are used in the subsequent chapters. The calibrated airfoil has its polar data visualized in Figure 4.2.

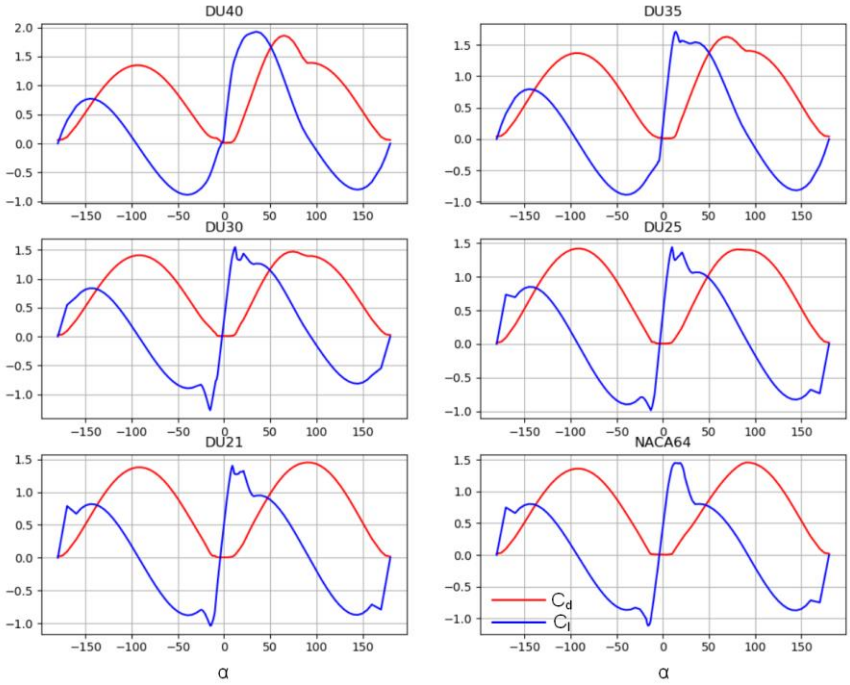

Figure 4.1: Polar data for all airfoils.

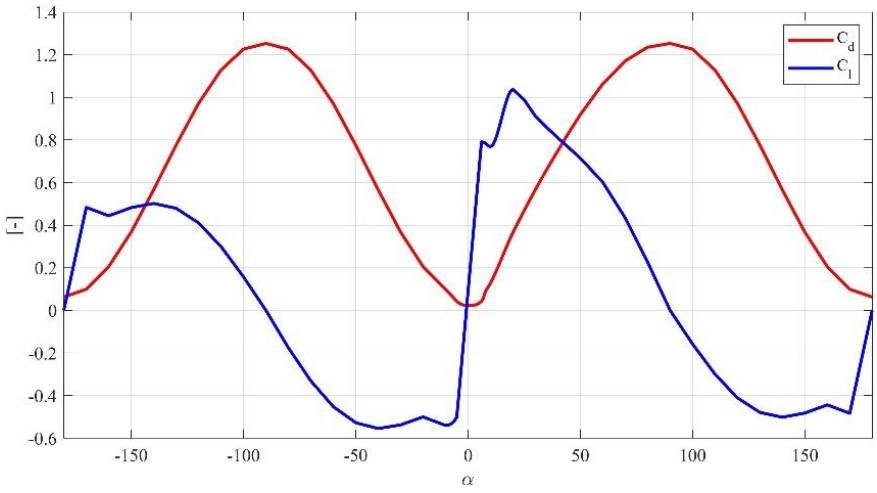

Figure 4.2: Calibrated polar data for OC5 comparison.

The system has a maximum thrust force of approximately 800 kN and a rotor torque of 4100 kN.m. Other steady-state responses of the wind turbine are provided in Figure 4.3.

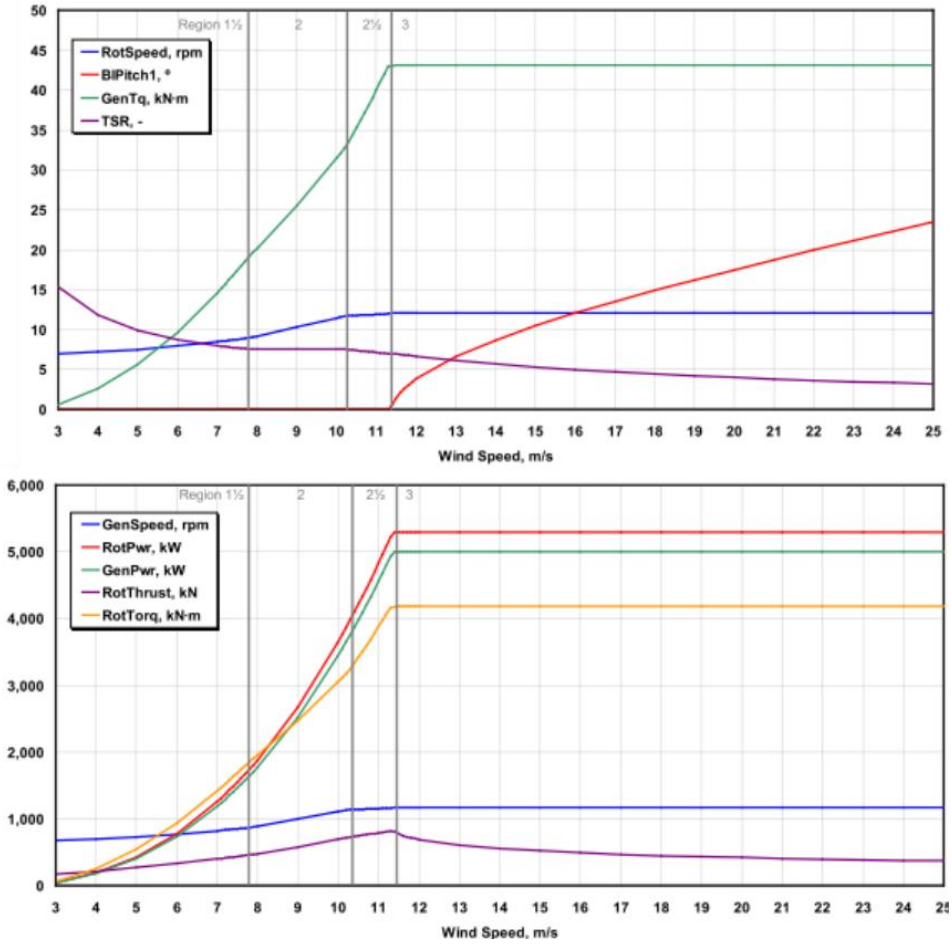

Figure 4.3: Steady-state responses of the 5-MW baseline wind turbine as a function of wind speed.
(source: Jonkman et al., 2009)

Initial validation is run to check the steady values of the numerical model when compared with the full-scale system. The variation of power and thrust coefficients C_P, C_T with the tip speed ratio (TSR) is illustrated in Figure 4.4, and a general agreement is observed.

The thrust force is the main driving force in FOWT systems. C_T values are checked for various blade pitching angles (see Figure 4.5). These steady values sufficiently agree with the data provided in Goupee and Kimball (2015) but not shown here. The wind load cases investigated in this study are moderate with a blade-pitch angle of 1˚ and an extreme case where the blades are pitched by 17˚. Figure 4.6 illustrates the validation of thrust coefficient values with the closest available angles (1˚ and 15˚) corresponding to a moderate and extreme wind loading, respectively.

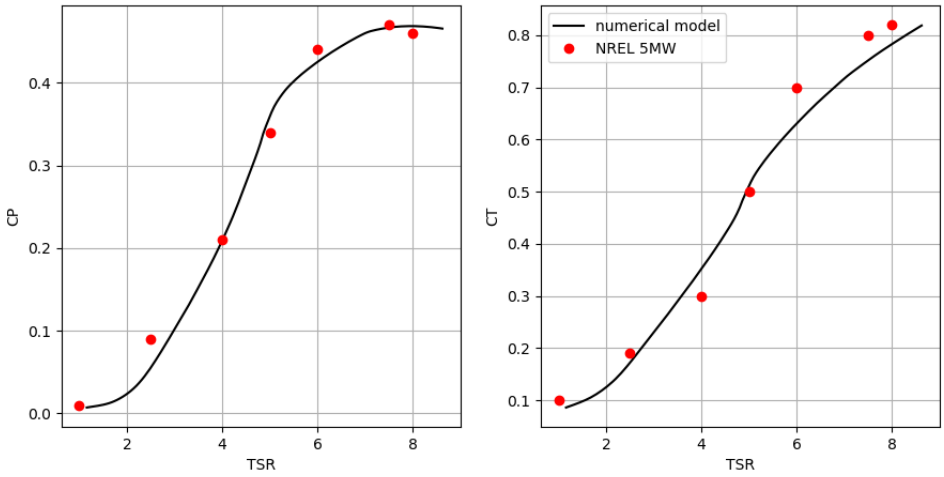

Figure 4.4: Power and thrust coefficient as a function of TSR.

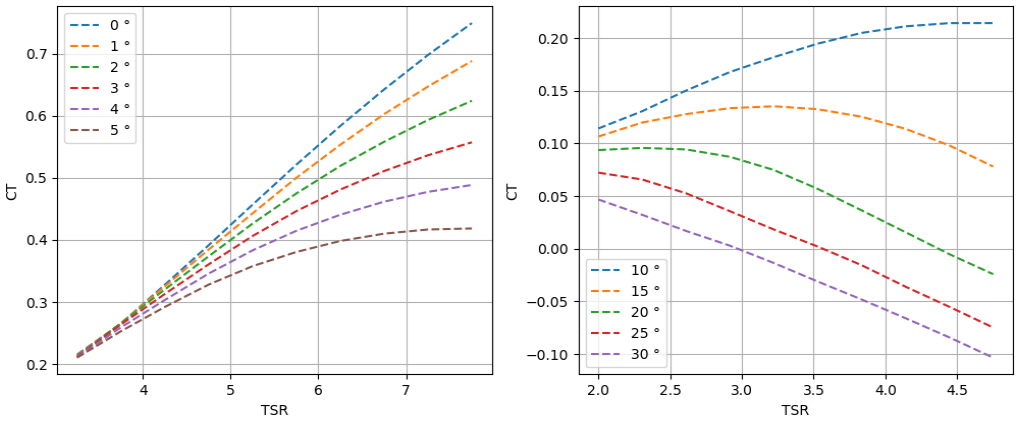

Figure 4.5: Thrust coefficient variation with TSR in various blade pitch angles.

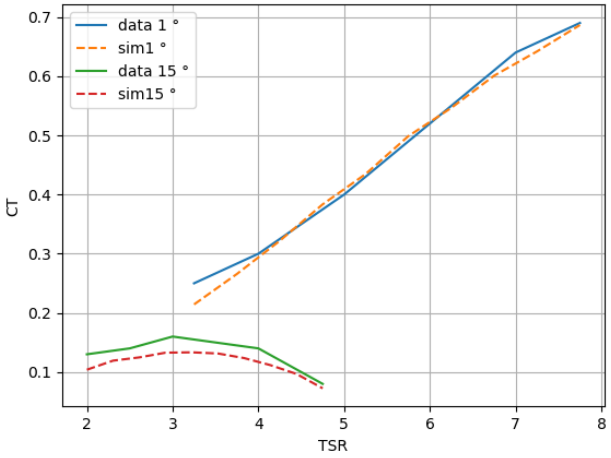

Figure 4.6: Thrust coefficient variation with TSR in two blade pitch corresponding to moderate and extreme wind loading.

4.2. Floating system definition

The floating platform in the OC5-phase II campaign is the DeepCwind semi-submersible shown in Figure 4.7. The overall geometric data are provided in Table 4.3, while structural properties, hydrostatic properties, and mooring system configuration are presented in Table 4.4 through Table 4.6.

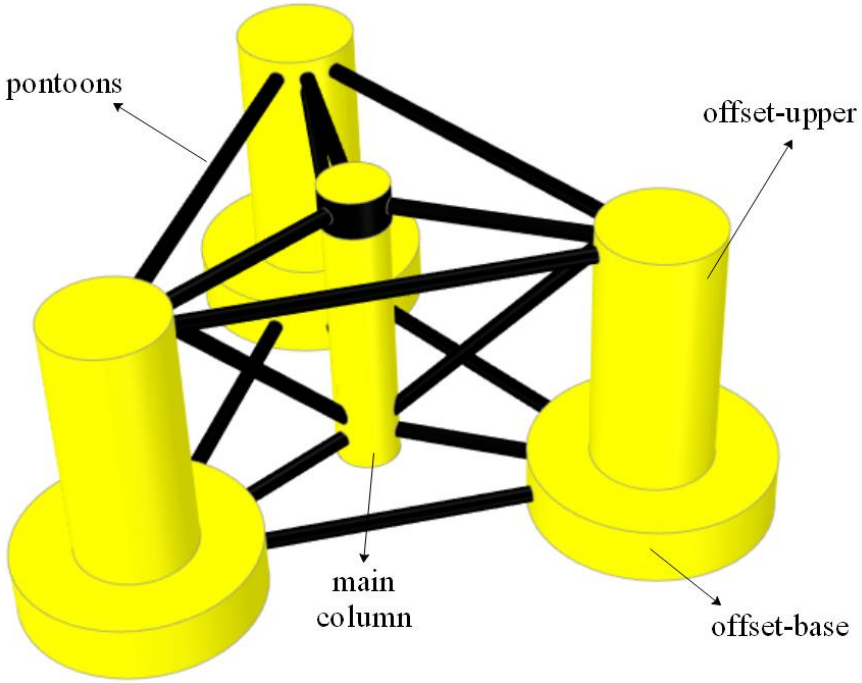

Figure 4.7: Perspective view of the OC5 DeepCwind floating platform geometry.

Table 4.3: Summary of the floating platform geometry and column properties.

Total draft		20 m	
Elevation to the tower base (air gap)		10 m	
Spacing between offset columns		50 m	
Greatest radius from centerline		40.868 m	
Column name	Diameter [m]	Wall thickness	No. of columns
Offset-upper	12	0.06	3
Offset-base	24	0.06	3
Main column	6.5	0.03	1
Pontoons	1.6	0.0175	15

Table 4.4: Structural properties of the floating platform.

Shell mass m_s	3852.2 t
Ballast mass m_b	9620.8 t
Depth to CoG	14.09 m
Ballast type	Water
Roll inertia I_{xx}	7.5534e+06 t · m^2
Pitch inertia I_{yy}	7.5534e+06 t · m^2
Yaw inertia I_{zz}	1.612e+07 t · m^2

Table 4.5: Hydrostatic properties of the DeepCwind floating platform.

Displaced water volume ∇	13988.36 m^3
Depth to CoB	13.19 m
Static buoyancy force F_B	1.3888e+05 kN
Hydrostatic restoring in heave k_{33}	3882.77 kN/m
Hydrostatic restoring in roll k_{44}	15683.47 kN · m/deg
Hydrostatic restoring in pitch k_{55}	15683.47 kN · m/deg
Water-plane area A_{wp}	386.28 m^2
Metacentric height $\overline{GM}$	6.31 m

Table 4.6: Mooring system properties for the DeepCwind.

Number of mooring lines N_c	3
Angle between the mooring lines θ_c	120°
Radius to fairleads from tower centerline	40.868 m
Radius to anchor from tower centerline	837.6 m
Unstretched mooring line length L_c	833.6 m
Linear density in air	0.1166 t/m
Steel density	8.298 t/m^3
Nominal diameter of the chain	0.079 m
Axial stiffness EA	764320 kN

(cont. on next page)

(table cont.)

Volume-equivalent diameter	0.1337 m
Volume-equivalent cross-sectional area	0.0141 m^2
Added mass coefficient C_a	0.5824
Transverse drag coefficient	1.2994
Longitudinal drag coefficient	0.2132
Cable pretension T_o	1124.485 kN

Large columns (offsets and central column) are modeled as diffracting elements, while pontoons and cross braces are modeled as Morison elements (see Figure 4.8). This setup is chosen after checking cylinder diameter to the wavelength (D/L) and KC number that indicates the relative importance of each model technique. The analysis is run over a moderate irregular wave loading and is presented in Figure 4.9.

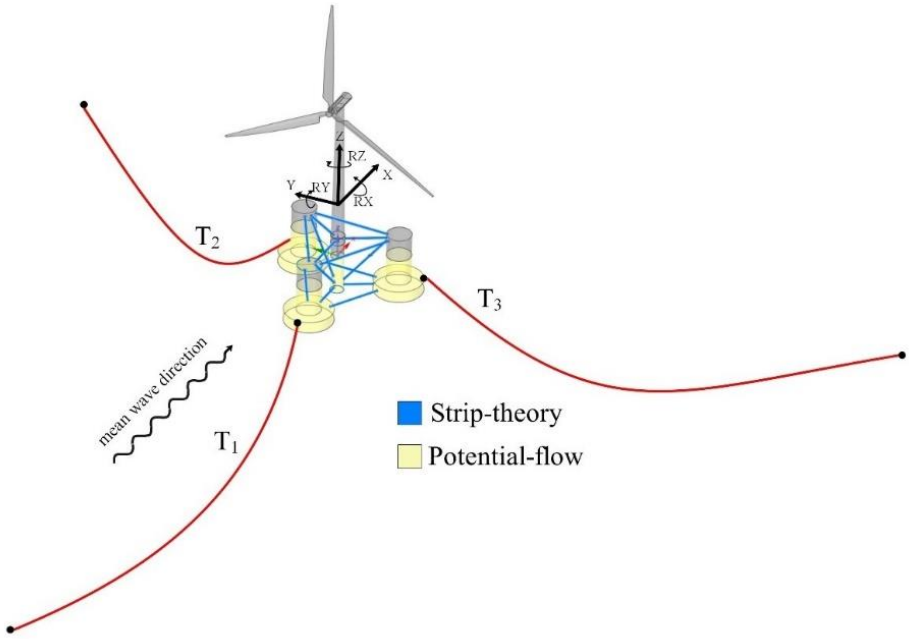

Figure 4.8: Schematic view of the FOWT system and its hybrid modeling features.

The diffracting columns of the platform is meshed with a defeaturing tolerance of 0.8m and a maximum element size not exceeding 1.4m. The resulting mesh is provided in Figure 4.10.

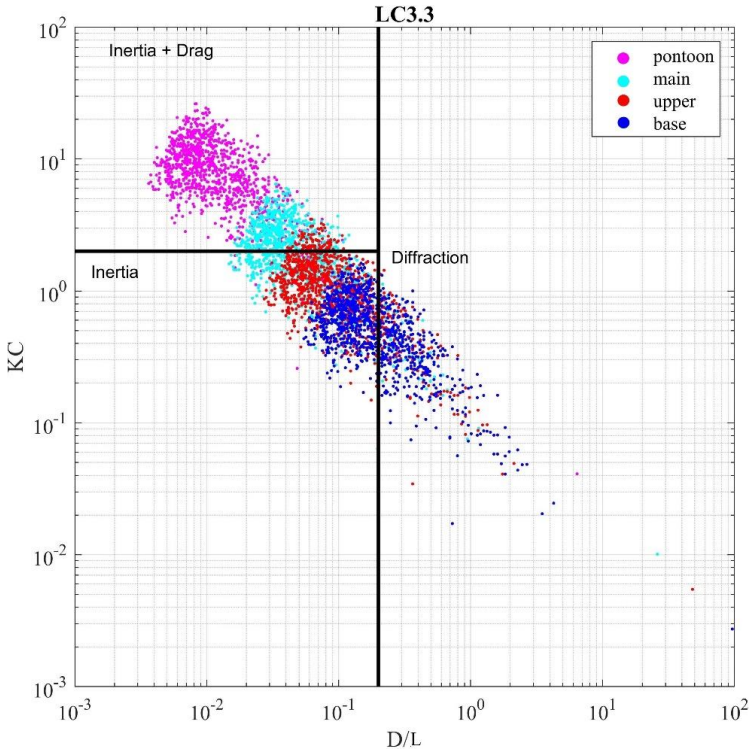

Figure 4.9: Classification of wave forces on the platform columns. The x-axis represents the ratio of column diameter to wavelength, and the y-axis is the Keulegan-Carpenter number.

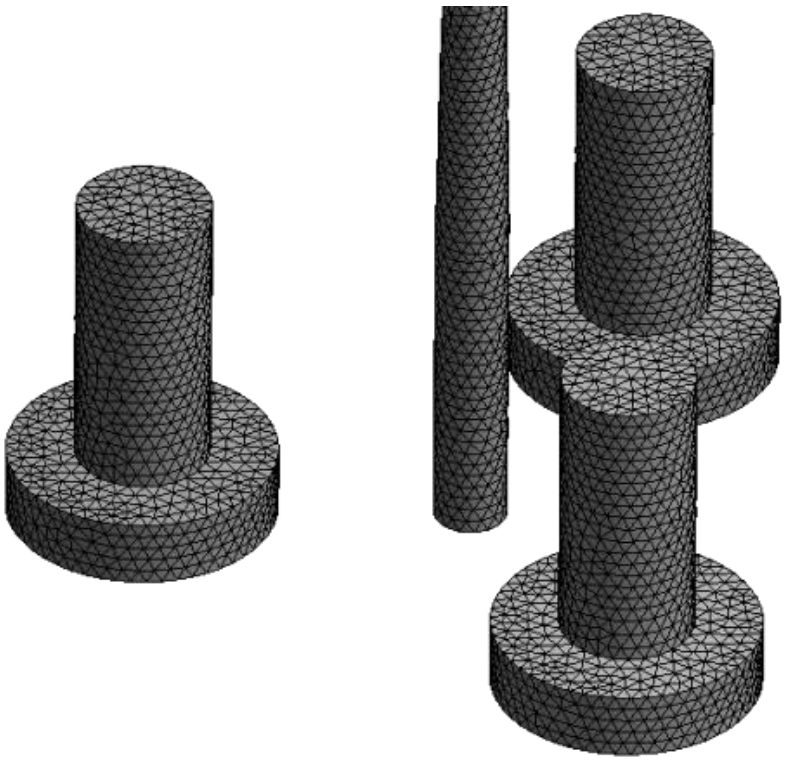

Figure 4.10: Meshed geometry of the diffracting parts of the DeepCwind semi-submersible platform.

Some Mooring properties are adjusted according to the data given by Hall and Goupee (2015) while ensuring all catenary lines have their properties equal to reserve static equilibrium of the system. The line sectional properties are calculated according to DNV GL (2015) and (Ulverston et al., 2010). The normal drag coefficient used is scaled by the nominal diameter to volume-equivalent diameter ratio and by the frontal area of the chain to the typical area ratio.

4.3. Calibration and Validation Procedure

After setting up the OC5 DeepCwind floating platform model, various hydrodynamic models are investigated using different calibration methods. Two calibration methods are used in this study. Then the models are compared and verified using physical model experimental results. Error assessment is then carried out to analyze the accuracy of two major proposed models with OC5 participants. The divergence in these models is of second-order nature, such as the damping and excitations induced by viscous forces. There is high uncertainty of responses in the proximity of the natural resonance of the structure. A full description of these differences is presented next.

4.3.1. Calibration

4.3.1.1. Free Decay Test (FDT)-based calibration

Utilization of free oscillation tests to calibrate the damping of the simulation by providing linear and quadratic damping matrix for all six modes is a well-known practice in the literature (for example: Gueydon et al., 2014; A. N. Robertson et al., 2014). The diagonal linear and quadratic damping forces ($F_{p_{jj}}$, $F_{q_{jj}}$) and moments ($M_{p_{jj}}$, $M_{q_{jj}}$) are proportional to the velocity and the velocity square, respectively:

$$F_{p_{jj}} = -P_{jj} \cdot \dot{u}_j, \qquad F_{q_{jj}} = -Q_{jj} \cdot \dot{u}_j |\dot{u}_j|, \qquad j = 1,3 \tag{4.1}$$

$$M_{p_{jj}} = -P_{jj} \cdot \dot{\theta}_j, \qquad M_{q_{jj}} = -Q_{jj} \cdot \dot{\theta}_j |\dot{\theta}_j|, \qquad j = 4,6 \tag{4.2}$$

where P_{jj},Q_{jj} are the diagonal linear and quadratic damping coefficients, respectively. Therefore, free decay tests (FDT) are carried out to calibrate the hydrodynamic linear and

quadratic damping of the structure. The free decay test results for all six modes are drawn and enveloped, as seen in Figure 4.11. The resulting damping coefficients are stated in Figure 4.12 after doing (p & q) analysis, as described in Helder and Pietersma (2013). The calibrated values are reported in Table 3, and the results fit well with the experimental data.

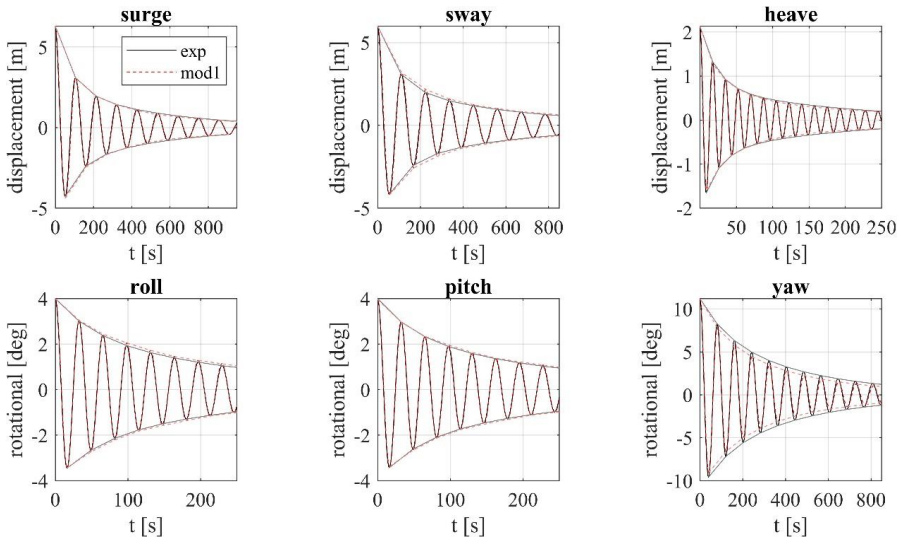

Figure 4.11: Free decay tests in all DoF and the envelope of the experiment's responses and the numerical model. The x-axis is time, and the y-axis is motion.

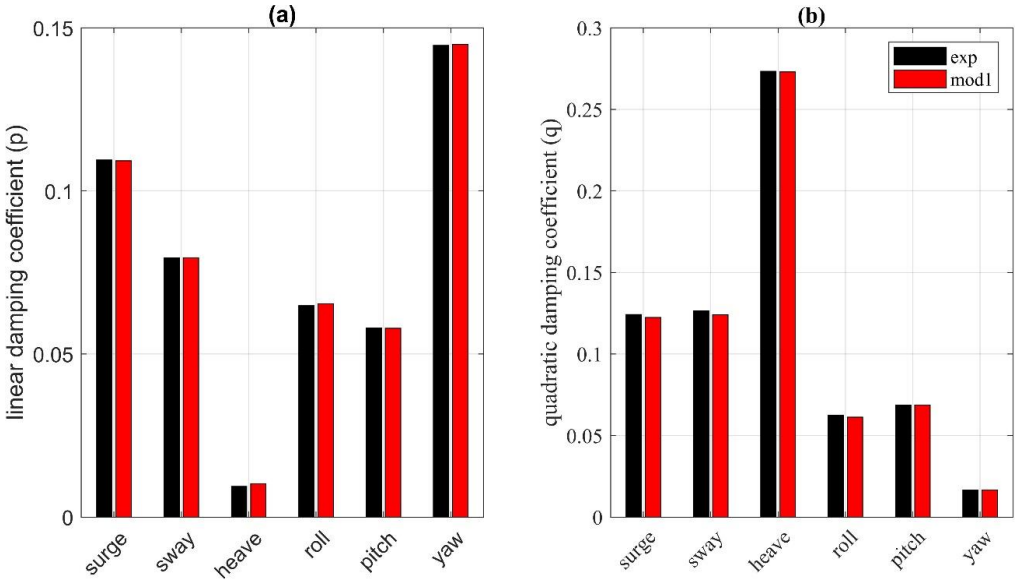

Figure 4.12: Linear and quadratic damping coefficients after calibration.

Table 4.7: Calibrated damping coefficients.

DoF	linear		quadratic	
	P_{jj}	unit	Q_{jj}	unit
surge	32	$\mathrm{kN/(m/s)}$	660	$\mathrm{kN/(m/s)^2}$
sway	18		700	
heave	0		1.4e+03	
roll	1.7e+03	$k\mathrm{N \cdot m/(^\circ/s)}$	2.2e+03	$\mathrm{kN \cdot m/(^\circ/s)^2}$
pitch	1.4e+03		3.7e+03	
yaw	1.2e+03		1.7e+03	

Two models are developed under FDT calibration. These are:

- mod1.a

For second-order wave forces, the model uses Newman's approximation (Newman 1974) for the estimation of the Quadratic Transfer Function (QTF) matrix

- mod1.b: mod1.a + QTF

Even though Newman's approximation is a handy tool for estimating second-order forces in deep waters, its precision is limited to high natural period DoF, such as the horizontal excursions of a semi-submersible. This model uses Pinkster's approach (Pinkster, 1980) to quantify the full quadratic transfer function (QTF) matrix.

4.3.1.2. Wave kinematics and irregular case-based calibration

Because free decay tests are run in still water, the absence of wave can lead to the erroneous calibration of non-linear damping (Chakrabarti, 1995). In the second calibration method, the calibrated linear and quadratic coefficients presented in mod1.a and mod1.b are not used. The wave kinematics is modeled through the calculation of drag term of Morison's equation serving as the non-linear viscous force at the instantaneous position of the structure, and the relative velocity between the wave-induced water particle velocity and the structural velocity is considered. The former is responsible for exciting the structure while the latter dampens it. To calibrate the structural damping, a

synthetic coupling parameter μ_c is associated with the hydrodynamic damping-induced velocity. The drag equation for a unit depth becomes;

$$F_{wk} = \frac{1}{2}\rho C_D D\left(\dot{q} - \mu_c \dot{u}_j\right)\left|\dot{q} - \mu_c \dot{u}_j\right| \tag{4.3}$$

The force is then integrated throughout the spontaneous wetted depth of the column, and the total drag force is calculated by summing the contribution from each column.

Eq. (4.3) results in a mean offset in wave direction. An additional mean drift force is added so that the overall mean drift viscous-induced force satisfies the following equation recommended by DNV (2010);

$$F_v = \frac{2}{3\pi}\rho g k C_D D a^3 \tag{4.4}$$

In case the wave is irregular, a becomes half the significant wave height. Eq. (4.4) is only applied to the columns above the mean water level to the wave crest (splash zone).

Two models are developed under wave kinematics and irregular case-based calibration. These are:

- mod2.a: By assigning a value of unity for the drag coefficient in Eq. (4.3), the coupling parameter equals 1.26 when calibrated according to a surge free decay test (equivalent to surge quadratic damping coefficient in mod1.a and mod1.b). Still, it equals a value of 0.25 (80% reduction) when calibrated through the moderate irregular wave case. A similar study has used 10% of the surge calibrated damping (Coulling et al., 2013).
- mod2.b: mod2.a + complementing mean drift viscous force.

The drag coefficient in Eq. (4.4) is calibrated according to mean surge value in a regular, moderate load case ($= 0.84$). Note that this drag coefficient is different than the one written in Eq. (4.3).

4.3.2. Validation

The aforementioned models are tested under a total of four load cases: two regular and two irregular cases. Each category comprises moderate and an extreme version. Table 4.8 provides a brief description of the cases.

Table 4.8: Wave load cases studied.

Load Case	Description	Conditions			Duration [s]
		H or H_s [m]	T or T_p [s]	γ	
LC 3.1	moderate regular wave	7.37	12.07	-	1,000
LC 3.2	extreme regular wave	9.41	14.3	-	1,000
LC 3.3	moderate irregular wave	7.1	14.1	2.2	11,534
LC 3.4	Extreme irregular wave	10.5	14.3	3.0	11,774

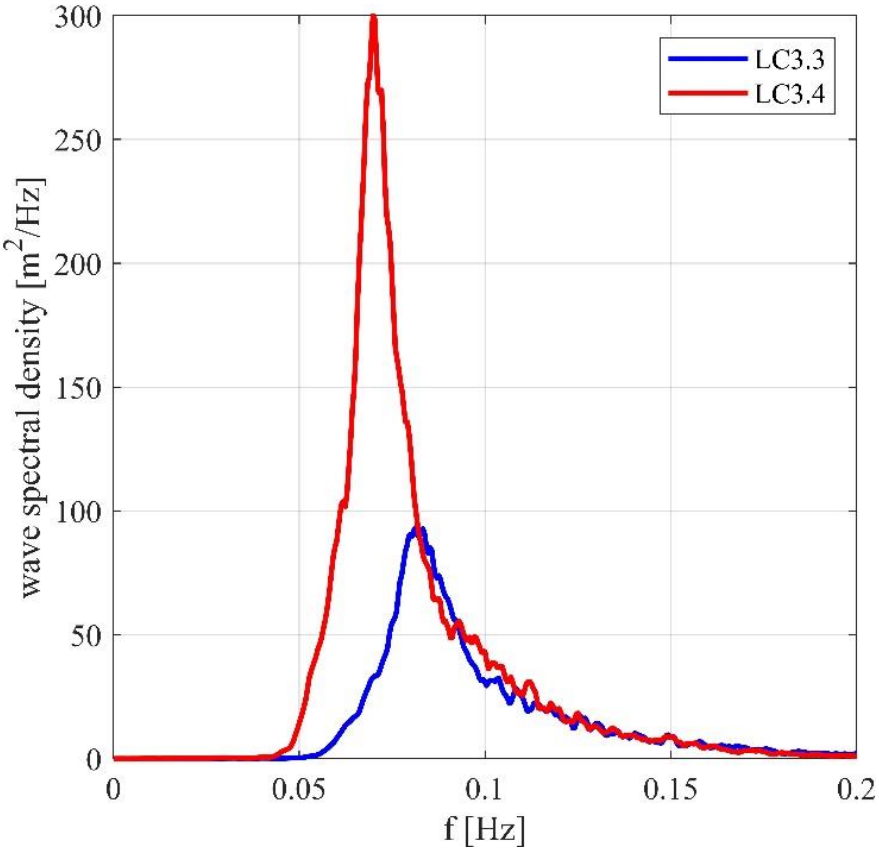

Figure 4.13: Wave energy spectrum for the moderate (LC3.3) and extreme (LC3.4) conditions.

The four models are compared with the OC5 experimental data of a 1/50th-scale tested at the Maritime Research Institute Netherlands offshore wave basin. The mainly excited degrees of freedoms by a 0˚ wave direction are considered, which are the displacements along the X-direction (surge: X), along the Z-direction (heave: Z) and the rotation around the Y-axis (pitch: RY). Additionally, the seaward cable is considered since it is the most exciting cable among the three catenary mooring lines (tension: T). These four responses will be referred to as (DoF^{o}).

- Regular waves

Both moderate and extreme regular wave load cases are employed. Under periodic wave and no wind condition, the structural response in surge can be divided into a dynamic component (analyzed through RAO) that expresses the amplitude of the response and a mean drift component due to viscous forces. Even though mean drift forces do not heavily influence RAO results in the surge, it must be included in the calculations as cable tension dynamics are directly interrelated with the mean surge drift of the structure. The results are presented in Figure 4.14 for DoF^{o}. Participants in the OC5 project have their TD values averaged since their phases match. A general agreement is seen for all models. Mod1 (refers to mod1.a as QTF is not applicable in regular wave case) seems to slightly under-predict mean drift in the wave direction, and mod2.b over-predicts it. Heave and pitch are in agreement with the experiment. The discrepancy is slightly growing with the extremity of the condition.

Tensions in the cable are directly influenced by the change in cables configuration due to fairlead motion as depicted in Figure 4.15. To illustrate the relation this relation, Figure 4.16 demonstrates the fairlead position in time versus cable tension where arrows on the left side of the figure show the direction of the fairlead horizontal excursion. The horizontal axis denotes the distance between fairlead and anchor, as demonstrated in Figure 4.15. As the platform oscillates, tensions do not change linearly, and maximum and minimum tension values do not coincide with the greatest or shortest distance but somewhere in the middle. However, under harsh environment, maximum and minimum tension values shift to the furthest position by 20%, creating a snap load-like effect. It can be seen that due to the application of a mean drift force in mod2.b, the dynamics of the tension is further corrected. It is even more prominent under extreme conditions.

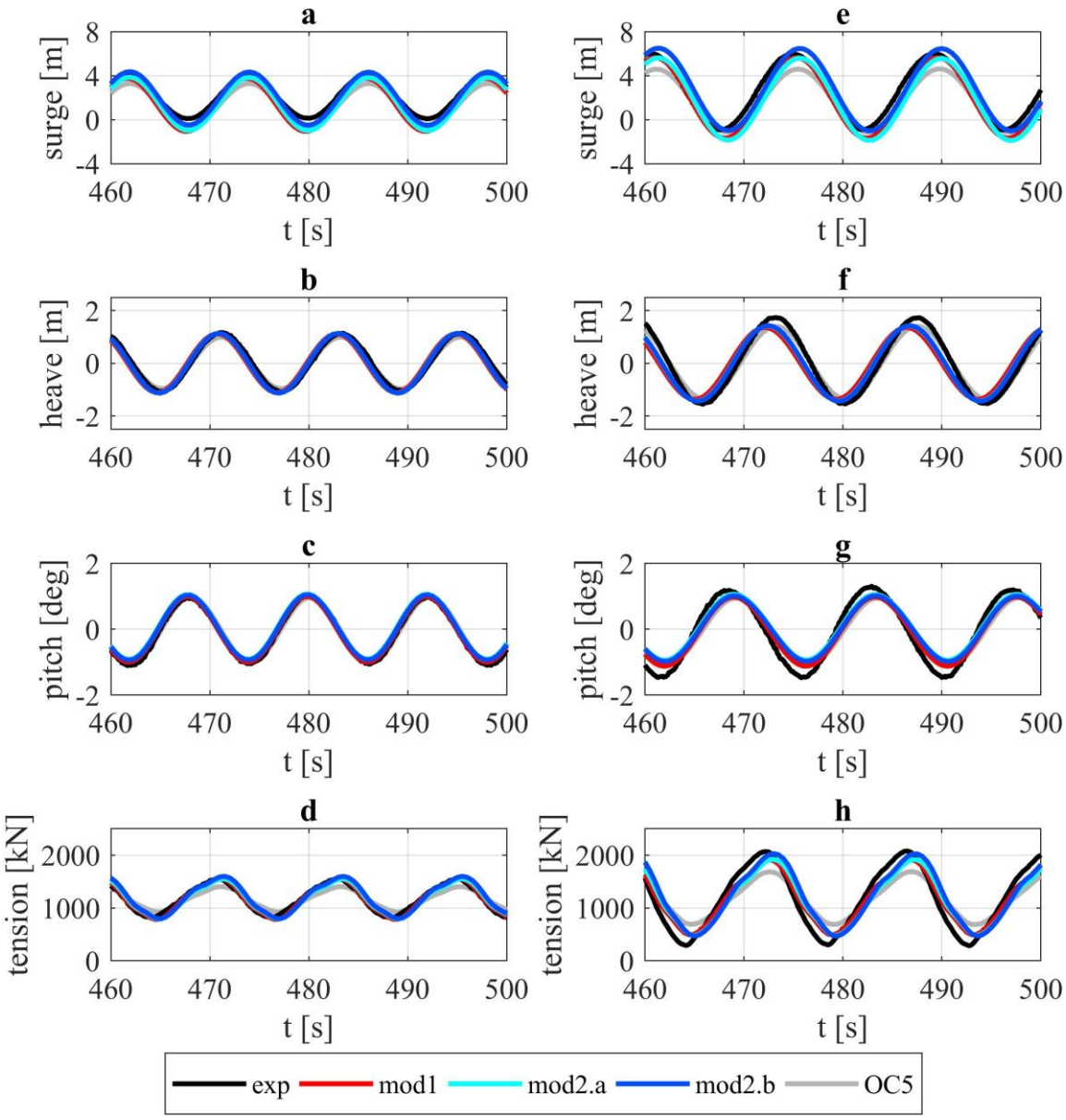

Figure 4.14: DoF^{o} responses under moderate [a-d] and extreme [e-h] regular wave loading

- Irregular waves

Due to the randomness induced by wave irregularity, the analysis is shifted to the frequency domain. Figure 4.17 illustrates the structural response in all models for DoF^{o} for the moderate case and Figure 4.18 for the extreme situation. Codes who have participated in the OC5 project have their frequency amplitude results averaged. The main differences are noticeable in surge and hence in tension. Mod 2b agrees very well to the experimental results.

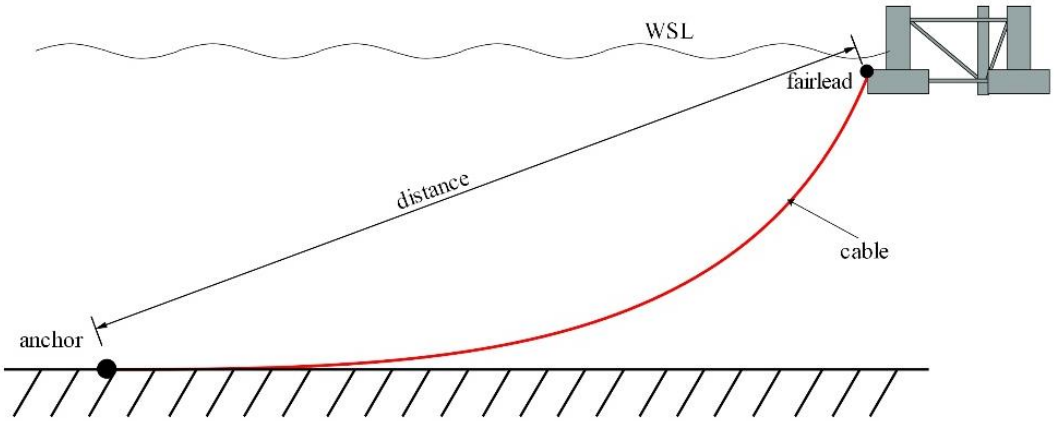

Figure 4.15: Schematic sketch showing the catenary mooring connection.

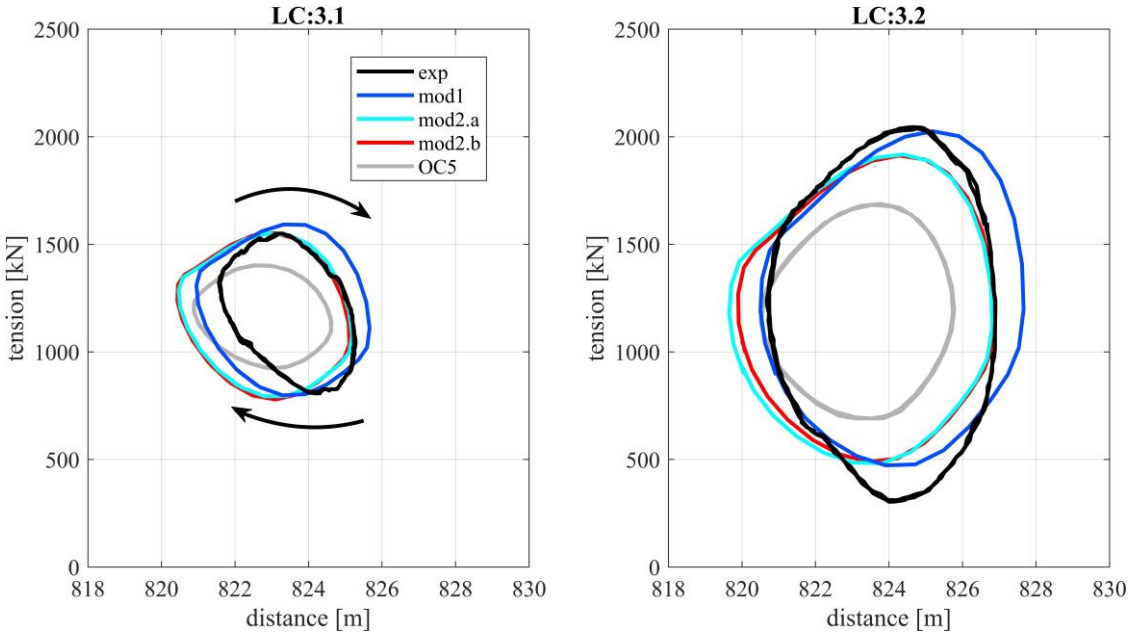

Figure 4.16: Motion-tension relation under moderate and extreme regular wave loading. The x-axis is the distance from anchor to fairlead.

LF responses in DoF^{o} are filtered according to the method mentioned in section 3.4 and are shown in Figure 4.19. The slowly varying oscillations are enhanced as upgrading the model, particularly in surge and tension. That being said, the response in wave frequency does not differ between the models and is equally accurate compared to the experimental data, especially in moderate excitations. As for design loading, the models show slight over-prediction in surge and under-prediction in pitch in the wave frequency. The same pattern is also observed in the regular wave cases (check Figure

4.14). The resonant response in all DoF^o is exclusively better when $\mu_c = 0.25$ regardless of the extremity of the loading. Mod2.a creates a slight over-prediction in low frequency of surge but the inclusion of a mean drift force in the direction of the wave enhances the peak values while making tension values agreeing more with the experiment. This correcting effect is more conspicuous in extreme conditions. Although calibrated according to the moderate case, mod2.b reserves its accuracy under severe conditions, which emphasizes the applicability of the upgraded model under various environmental conditions. Since the damping of the system is dependent upon the extremity of the loading (Gueydon et al., 2014), employing free decay tests as the sole source of calibration does not provide accurate results. In contrast, water particle velocity and mean drift viscous force impeded in Mod2.x are proportional to the wave height, which accentuates the dynamics counted in these models dissimilar to mod1.x. If the damping matrix is to be used along with the potential flow solution, it is suggested to calibrate the coefficients based on a forced oscillation test (the analysis of second-order oscillation initially induced by the application of monochromatic wave loading) for various wave heights and periods to enhance the fidelity of the hydrodynamic model (Chakrabarti, 1995).

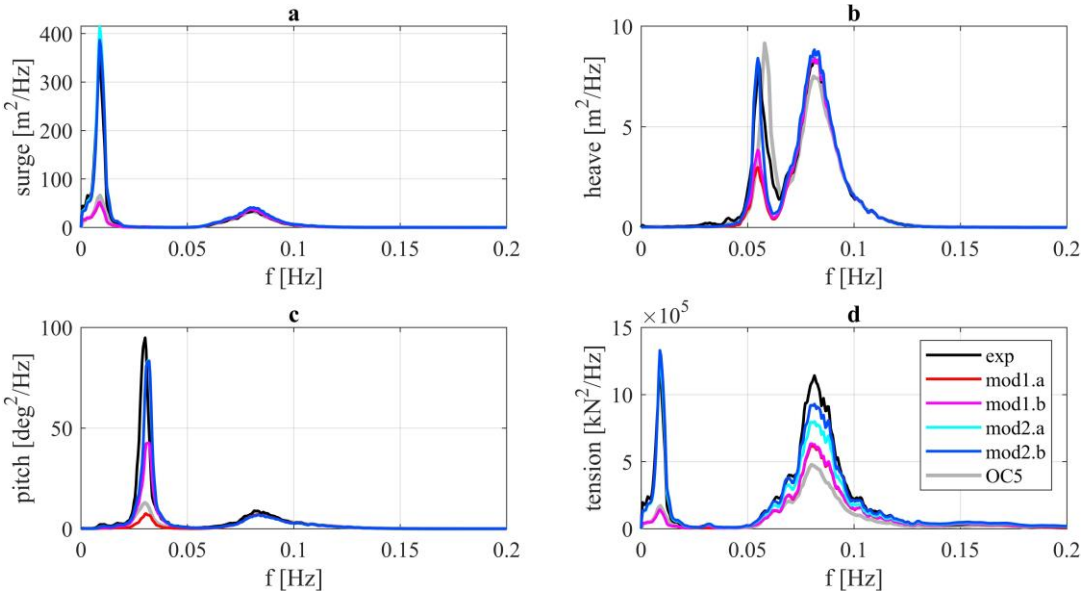

Figure 4.17: Frequency-domain comparison of DoF^o under moderate, irregular wave excitation.

Table 4.9 provides statistical analysis platform responses under extreme conditions for all the models and the experiment. Table 4.10 concludes the main

improvement of the models mentioned above. Mod2.b is the most recommended model. The enormous correction occurred when wave kinematics are modeled in a vast range of frequency and responses.

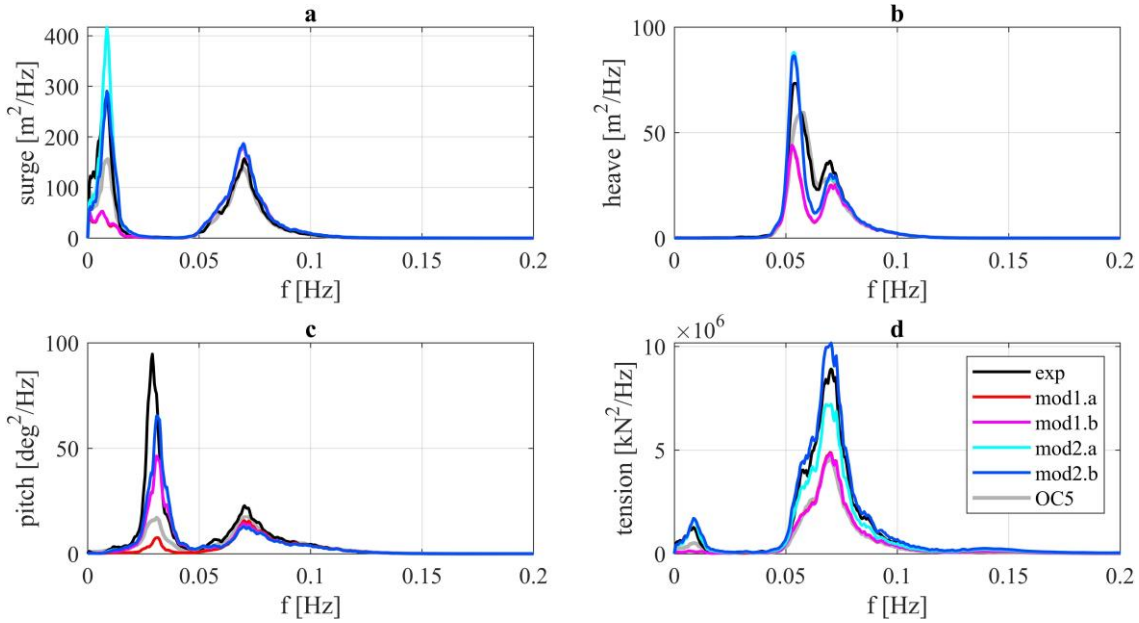

Figure 4.18: Frequency-domain comparison of DoF° under extreme, irregular wave excitation.

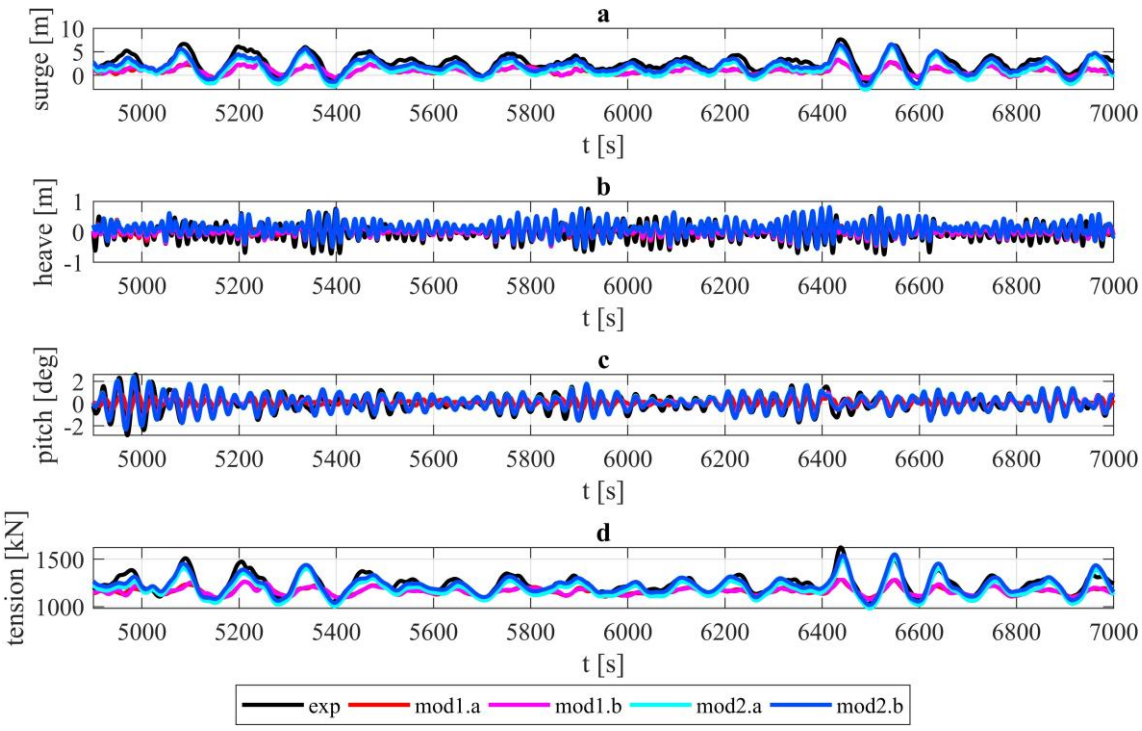

Figure 4.19: Low-frequency motion in time-domain for DoF° under moderate, irregular wave excitation.

Table 4.9: Statistical summary of LC3.4 responses.

statistic	Mod1.a	Mod1.b	Mod2.a	Mod2.b	Exp
	X				
Mean	0.85	0.83	1.59	3.74	3.17
Std. Dev.	1.97	1.98	2.50	2.38	2.27
Max.	9.40	8.87	14.48	16.01	16.31
Min.	-7.42	-7.56	-6.18	-3.84	-2.92
	Z				
Mean	0.13	0.13	0.13	0.13	-0.03
Std. Dev.	0.89	0.90	1.09	1.09	1.14
Max.	3.79	3.68	4.09	4.09	4.47
Min.	-2.87	-2.84	-3.91	-3.91	-4.45
	RY				
Mean	0.08	0.08	0.10	0.00	0.03
Std. Dev.	0.68	0.92	1.00	1.00	1.14
Max.	3.79	3.68	4.09	4.09	5.43
Min.	-2.49	-3.45	-3.84	-4.09	-4.56
	T				
Mean	1158.10	1155.70	1207.30	1334.90	1265.80
Std. Dev.	330.42	332.14	419.11	489.28	448.13
Max.	3667.10	3651.70	5243.80	5690.00	5414.20
Min.	-21.83	-219.23	-169.94	-127.86	-29.93

Table 4.10: Frequency region at which the improvement of each setting is observed.

	reduced damping				wave kinematics		mean drift force	QTF	
DoF^o	X	Z	RY	T	X	T	T	Z	RY
frequency range	LF	LF	L	L	LF	LF* WF	WF	LF	LF

LF*: enhancement is seen at even lower frequencies (0 - 4E-03 Hz)

4.3.3. Error assessments

The absolute percentage error APE is used for error calculations and has the form;

$$APE = 100\% \left|\frac{A - F}{A}\right| \tag{4.5}$$

where A is the actual observed value, and F is the model value. Two models of the proposed ones are compared here; the most upgraded model from each family (mod1.b and mod2.b) to highlight the distinction between the two methods of calibration. As for participants in OC5 project, they are categorized according to the utilized hydrodynamic model into three categories (summarized in Table 4.11):

1- PF: potential flow-based models with the inclusion of damping matrix

2- hybrid: potential flow-based models with the addition of drag term from Morison's equation

3- ME: Morison-only (strip-theory) models

and according to the mooring model into two categories:

1- DMM: dynamic mooring model

2- QSMM: quasi-static mooring model.

Table 4.11: Summary of OC5 participants categories.

	Hydrodynamic Model			Mooring Model	
	PF	hybrid	ME	DMM	QSMM
number of participants	1^{st*}: 3 2^{nd*}: 0	1^{st}: 6 2^{nd}: 6	6	18	3
investigated response	X, Z, RY			T	

1^{st*}, 2^{nd*} indicates the order of the potential flow model used

For a regular wave case, since QTF does not apply in here, mod1.b becomes mod1.a. RAOs are compared and shown in Figure 4.20 for the DoF of interest. The difference between the two models is small and both less than 25%. Other codes have most of their errors concentrated in the tensions. Dynamic mooring model users

performed better in both cases. 2nd order potential-flow models have higher accuracy, especially in LC3.2. Nevertheless, models are close to each other, and errors are generally amplified when conditions are extreme. It should be noted here that the present model results are better than other codes in terms of tension, heave and pitch in moderate wave conditions. In extreme case the present model results are similar to the other codes except tension. In fact, tension performance of the present study is the best among them.

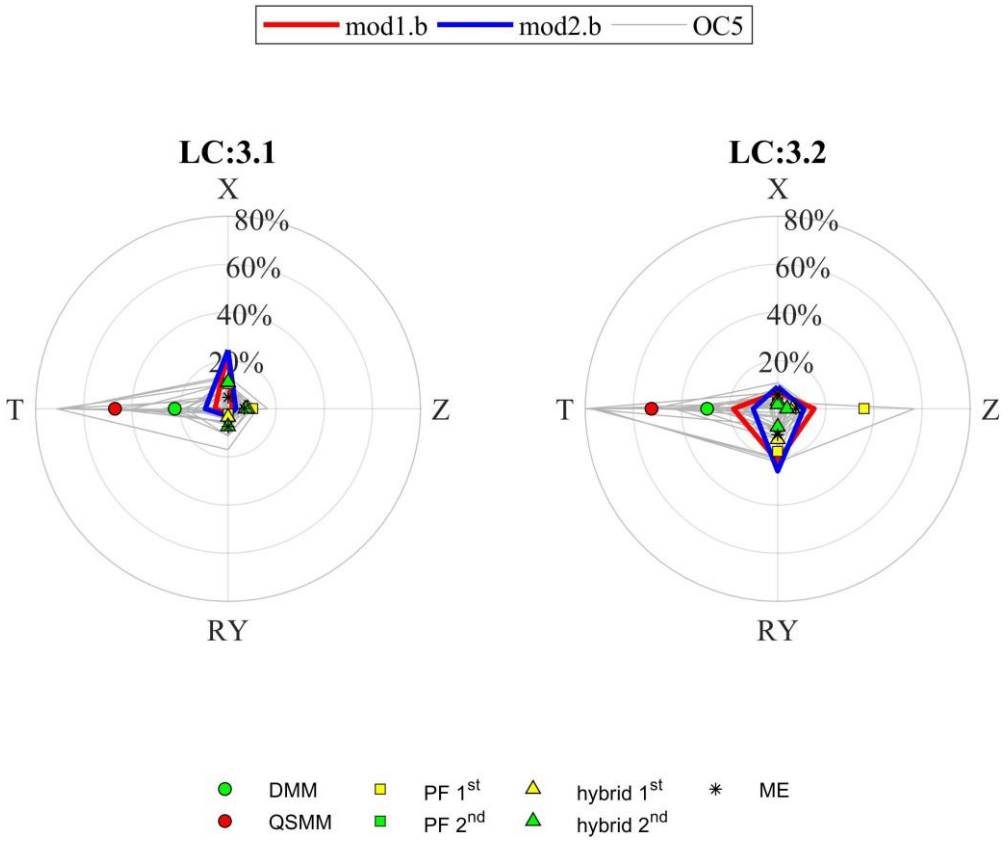

Figure 4.20: RAO response error assessment for regular wave cases in DoFº. The radii are the absolute percentage error (APE).

As for irregular wave cases, the error in the frequency response is calculated by comparing the amplitudes of the low frequency (LF) and the wave frequency (WF) response with the experimental amplitudes. Figure 4.21 presents the absolute percentage error for the two cases of the magnitude of LF (drift) and wave responses between the models and the experiment. Discrepancies in drift motions between the models are more scattered than in wave response. The lines connecting (X) and (T) in drift is almost always parallel with a slope of unity due to the direct proportionality between surge motions and tension responses. The two models show a considerable discrepancy in the resonance excitation region with mod2.b being more accurate amongst other responses. The wave

part, however, does not vary that much. The only case where mod1.b generates more excellent results is in a surge wave frequency response.

Considering participants' codes in OC5. Quasi-static models have their mean errors reach 80% in WF, but even when using dynamic models for the cables, the error is still in the range of 30%. It is evident that capturing 2nd order motions are crucial for reducing the error in tensions. 1st order potential-flow based models with only damping matrix included have the most significant errors between the other codes. The inclusion of 2nd order terms in hybrid models lessens the error as anticipated. Error results of mod2.b, while close in their WF values to the average error from participants' codes, are too minuscule in the LF part. For instance, while the average participants have errors in proximity to 50% for X, RY, and T, mod2.b, errs around 7%.

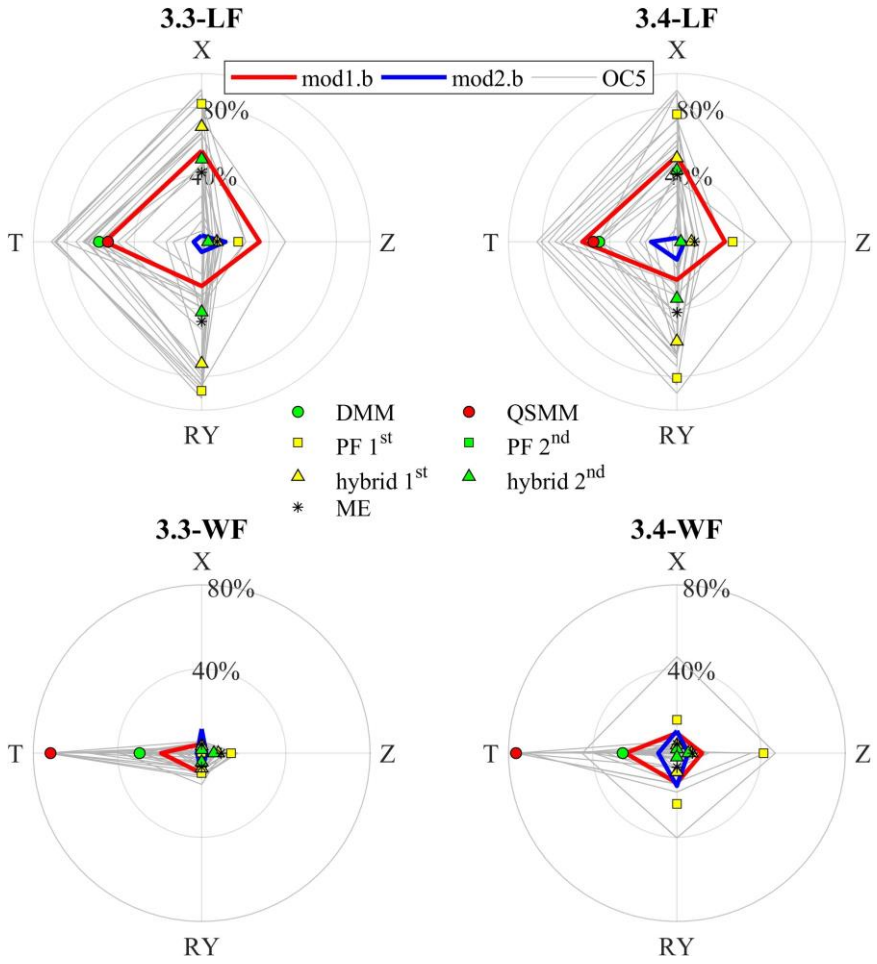

Figure 4.21: Absolute percentage error of the drift and wave response amplitude comparison of the two proposed models and OC5 numerical models with the experimental data for both moderate and extreme irregular wave cases. The radii are APE.

Finally, a time-domain comparison is carried out by calculating the regression between the two proposed models and the experiment, and the results are plotted in Figure 4.22 for moderate and Figure 4.23 for an extreme case. Unlike frequency-domain, point-to-point comparison in time denotes that amplitude, mean drift values, and signal phases are involved variables for the overall accuracy assessment. Mod2.b provides better matching with the experiment in all responses with regressions above 0.9 except for pitch. This discrepancy results from the small difference of natural frequency of pitch between the model and the test model that is also manifested by a slight peak shift in LF amplitude (Figure 4.17 and Figure 4.18). As the environmental conditions become extreme, discrepancies increase except in the front cable tension.

Additionally, the regression line equation of each model indicates the tendency to whether the model under or over-predict the results. For instance, the line equation for surge response in Mod2 under a moderate case has a slope of unity. Still, it intersects with the y-axis at -0.6, denoting a proper agreement in the deviation of the response but an under-prediction of the mean surge. Tension T2 is slightly under-predicted in a moderate wave loading but is slightly over-predicted in the extreme case.

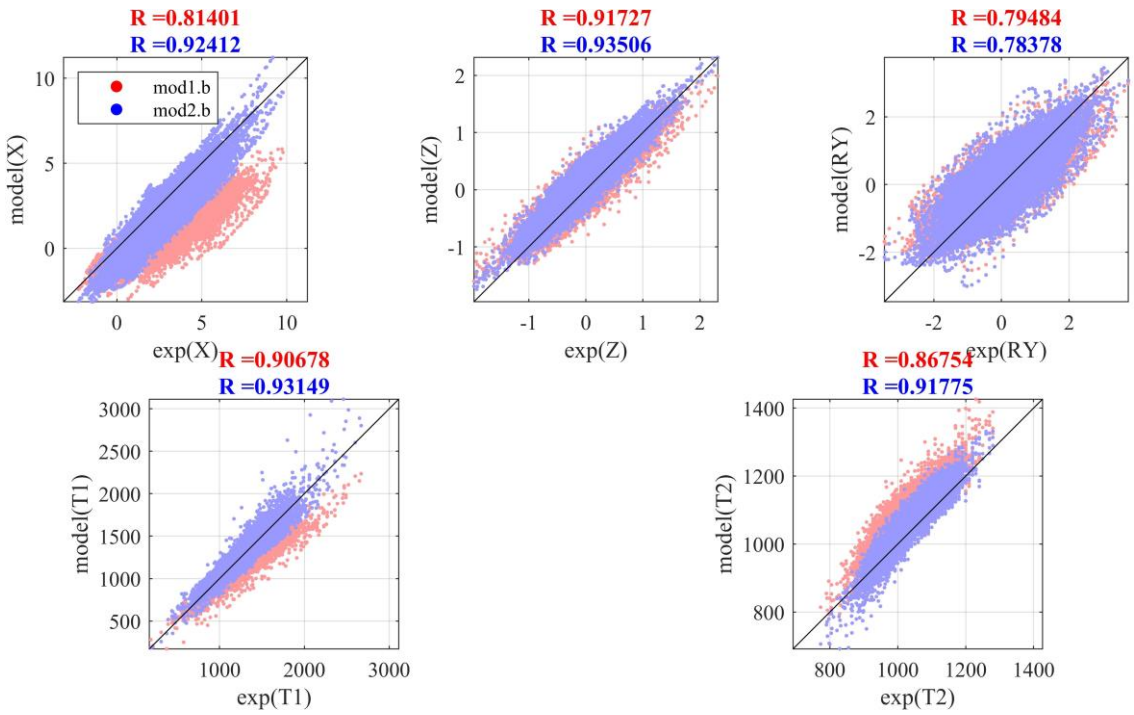

Figure 4.22: Regression plots between the two models and the experiment in the surge, heave, pitch, one leeward, and seaward cable tension in moderate condition.

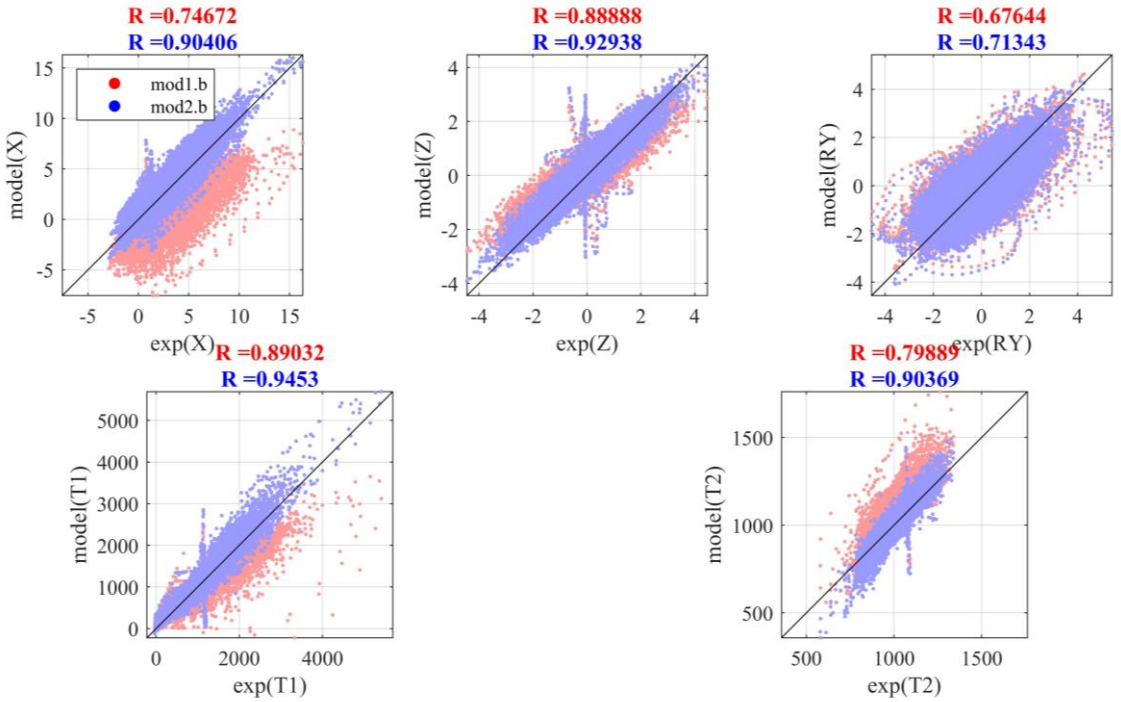

Figure 4.23: Regression plots between the two models and the experiment in the surge, heave, pitch, one leeward, and seaward cable tension in extreme condition.

4.4. Wind and Wave Load Case

The final stage in the validation process is to test the system under the stochastic excitation of wind and wave simultaneously. Wave properties are the same as LC3.3 (see Table 4.8). Additionally, dynamic-wind formulated according to the Norwegian petroleum directorate (NPD) spectrum with a mean wind velocity of 13 m/s and has the following spectral density definition:

$$S_U(\omega) = \frac{\left(\frac{320}{2\pi}\right)\left(\frac{U_{10}}{10}\right)^2\left(\frac{z_{hub}}{10}\right)^{0.45}}{(1+t^n)^{5/3n}}$$
$$t = \left(\frac{172}{2\pi}\right)\omega\left(\frac{U_0}{10}\right)^{-0.75}\left(\frac{z_{hub}}{10}\right)^{2/3} \quad (4.6)$$

where $U_{10} = 10.8\,m/s$ is the one-hour mean wind speed at height 10m above sea level and z_{hub} is the nacelle height and $n = 0.468$. The resulting spectrum is given in Figure 4.24.

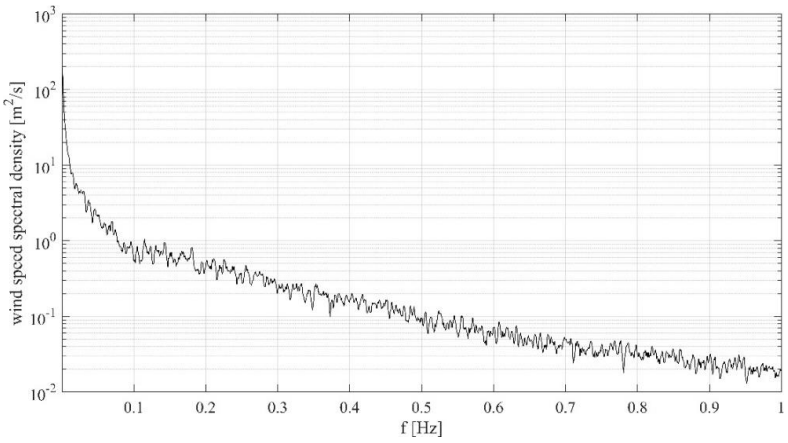

Figure 4.24: Wind energy spectrum.

The spatial variation of the experimental wind speed data is considered. The measured wind speed 2-D map in front of the rotor (see Figure 4.25) is interpolated throughout the swept area, as displayed in Figure 4.26.

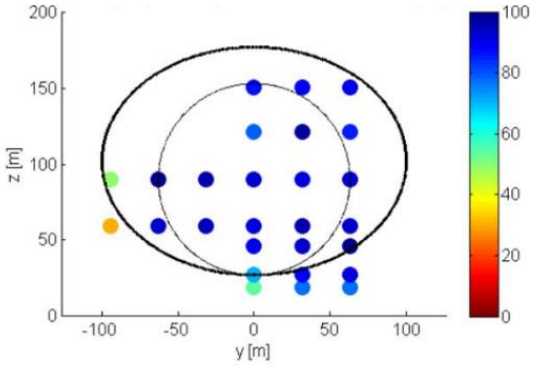

Figure 4.25: Wind velocity as a percentage of the maximum wind velocity.

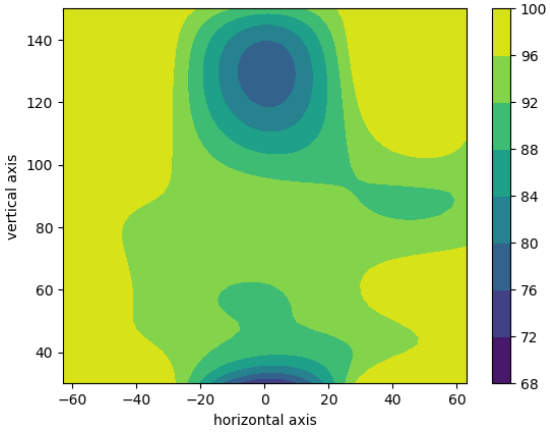

Figure 4.26: Interpolated wind velocity contour map as a percentage of the maximum wind velocity.

The external force exiting the aerodynamic model is isolated, and its PSD is drawn in Figure 4.27. Its resemblance to the wind spectral density is not a surprise. Some energy is observed at the low frequency where the platform's natural frequency in surge resides. Additionally, two peaks at 0.6 Hz and 0.8 Hz corresponding to the third and fourth harmonics of the blade-passing once-per-revolution frequency (1P). Although it is common to see 3P in three-bladed turbines, 4P is more ambiguous. It is believed that spatial variation of wind might be the cause of 4P excitation or at least a contribution to it.

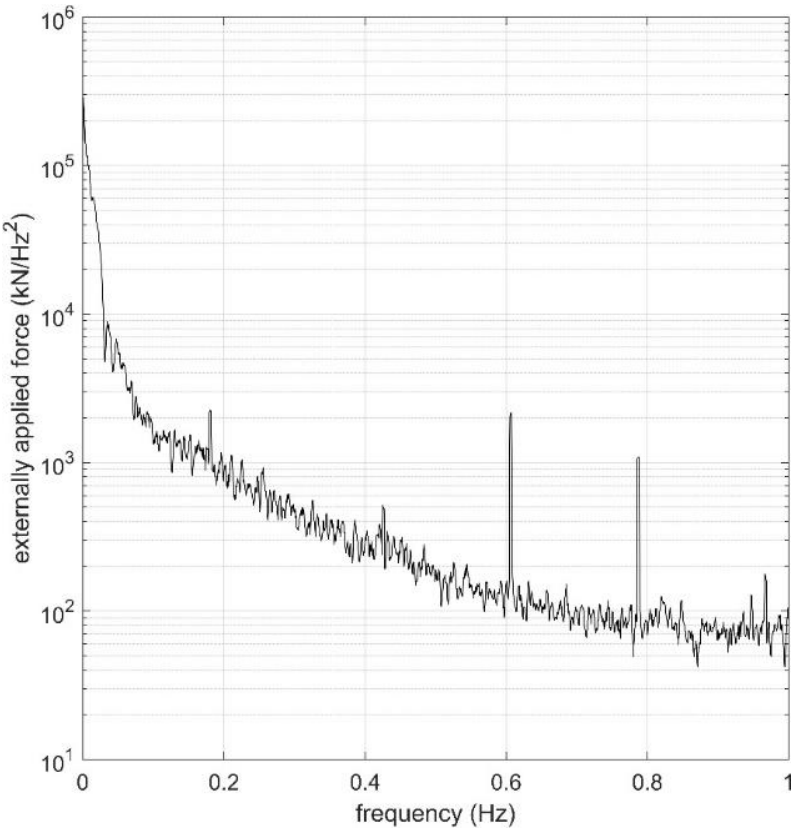

Figure 4.27: Power spectrum density of the aerodynamic force applied at the CoG of the platform.

The hydrodynamic model adopted here is mod2.b. the whisker plots represent a statistical summary in Figure 4.28. The model failed to simulate the same range of oscillation occurred in the thrust force measured. This variation originated a high swing in the horizontal excursion X and the tension of the seaward cable as well. That is evidence that steady calibration of the aerodynamic, while gives satisfactory results in terms of getting the proper mean values, is not sufficient to capture the dynamic

component of the excitation. The mean value of the surge is under-predicted in the simulation, which reflects the same effect on the primary cable tension T2. This discrepancy, however, might be due to some uncertainties in the experimental value. It is reported in Robertson et al. (2017) that the equilibrium position prior to testing for wave only cases was recorded and subtracted from the data but not when wind was present. Surge equilibrium variation might be caused by the mooring line being dragged to a new position after numerous testing. Surge mean excursion is a function of the mean thrust force and mean drift caused by waves. Since the numerical model (mod2.b) captured (and even over-predicted) the mean drift in the wave-only loading case (see Table 4.9), and the mean thrust coefficient is identical, nothing else justifies the additional excursion in the experimental results. Nevertheless, Other DoF values seem to have reached satisfactory agreement with the experimental data.

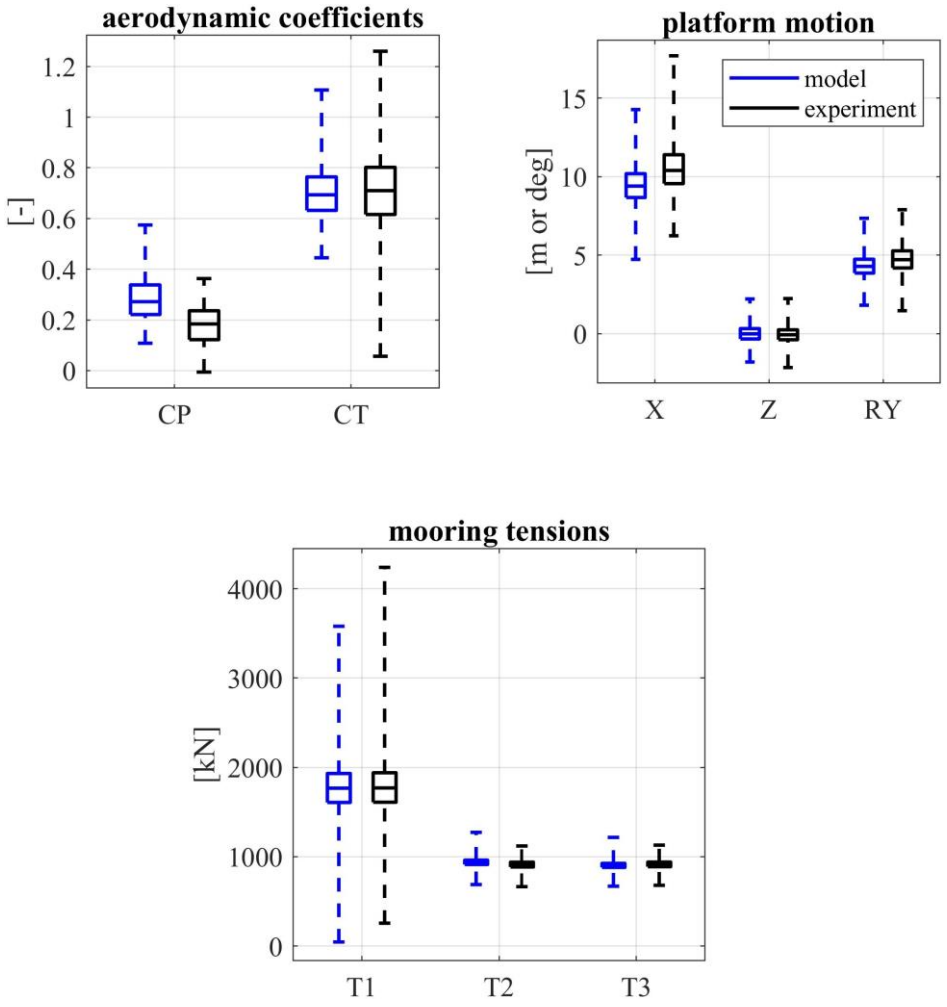

Figure 4.28: Whisker plot on the aerodynamic coefficients, platform motion, and mooring tensions for the model and the test data.

4.5. Effect of Wave Irregularity on the Structural Response

Irregularity is an important feature that characterizes realistic sea waves. Frequency spectrum and directional spreading are the known representations of the wave irregularity. In this study, after validation of model 2.b, the effects of frequency spectrum shape and directional spread on the floating wind turbines' responses are investigated in low and wave frequencies.

4.5.1. Effect of frequency spectrum shape

Storm waves generated by strong winds in a relatively small sea area are known to have a feature that the wave energy is concentrated in a narrow frequency range; i.e., the frequency spectrum exhibits a sharp peak. The peak enhancement factor γ presented in Eq. (3.7) controls the spectral sharpness. By alteration of γ, four spectral shapes are investigated as listed in Table 4.12. 3-hours-long time series are created synthetically using DSA (Deterministic Spectral Amplitude) method by keeping the significant wave height H_s and peak period T_p constant but changing the peak enhancement factor γ. Different time series can be obtained in DSA method by setting up the target spectrum and using random numbers for phase angles. Seed definitions used for generating the profiles are delicately chosen so that the spectrum width, wave height distribution, and wave groupiness are different in those four cases.

The spectral narrowness is determined by the parameter of Longuet Higgins, (ν) that has the definition given below:

$$\nu^2 = (m_0 m_2 - m_1^2)/m_1^2 \tag{4.7}$$

where

$$m_n = \int_0^\infty f^n S(f) df \tag{4.8}$$

The parameter ν takes the value between 0 and 1. The closer it is to zero, the narrower the spectrum becomes. As can be seen in Table 4.12, the spectral shape becomes tighter and sharper as going from I to IV.

Individual wave heights of actual ocean waves are known to follow the Rayleigh distribution approximately. According to Rayleigh distribution which is derived based on the narrow spectrum, the ratio $H_{10}/H_s = 1.27$. H_{10} is the mean of the highest one-tenth wave heights in the wave profile. The ratio of H_{10}/H_s can be used to check the deviation of wave height distribution from the Rayleigh. H_{10}/H_s values corresponding to four spectral shapes are given in Table 4.12. Table 4.12 shows when the spectrum becomes narrower, H_{10}/H_s ratio is close to 1.27.

Table 4.12: Synthetic wave spectrum settings for testing wave irregularity effects.

Spectrum Case	γ	ν	H_{10}/H_s
I	1.0	0.37	1.23
II	3.3	0.32	1.25
III	7.0	0.28	1.26
IV	10.0	0.25	1.27

The basic definition of a wave group can be given as the sequence of high waves in a wave train. Up to now, many parameters and different methodologies have been used to characterize wave groups. In this study, the mean run length mrl defined by Goda (2010) is used to check the wave grouping. The run length is the number of waves exceeding a specified value of the wave height (e.g., the significant wave height $\overline{H}$ in this study) without falling below that height. A succession of such high waves is called a *run* of high wave heights. mrl is the sum of run lengths divided by the number of runs in a wave series. Mean run lengths for the four cases given in Table 4.12 are calculated for both a moderate wave with $H_s = 7.42\,m$ and an extreme wave with $H_s = 9.72\,m$. Frequency spectrums and the calculated mrl values are offered in Figure 4.29. It should be noted that the difference in the significant wave height is less than 5 % in the time series corresponding to the given four spectral shapes. As anticipated, groupiness in the wave train is pronounced as the wave spectrum becomes narrower (Longuet-higgins, 1957, Ozbahceci et al., 2002).

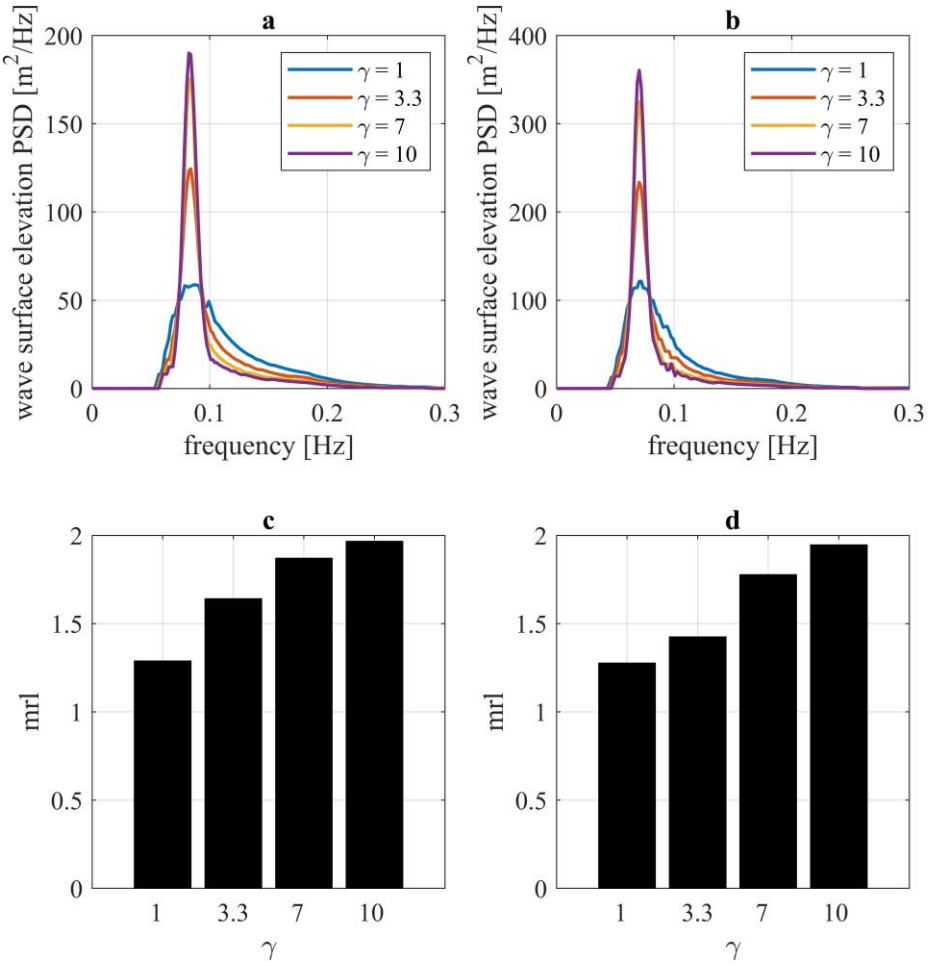

Figure 4.29: Power spectral density for the synthesized wave surface elevation and groupiness factor mrl of each spectrum shape (a and c for the moderate wave, b, and d for the extreme wave.

The moderate case is used to examine the influence of spectrum shape upon the resonant (drift) and wave response of the structure, while the extreme case examines that influence upon the mooring tension and snap load events. Drift and wave response amplitudes for surge (X), heave (Z), pitch (RY), and tension (T) corresponding to four different spectral shapes are compared in Figure 4.30. The amplitude of resonant response for the drift seems to decrease as the spectrum shape becomes narrower. The reason behind this reduction is due to the concentration of energy into a smaller wave frequency bandwidth as the spectrum becomes narrower. The decrease in the drift response amplitudes is almost 20% when γ is increased from 1.0 to 3.3. When the spectrum is very narrow (γ=10) the decrease in the drift amplitudes becomes 40%. Responses at wave frequency, however, has an opposite reaction: an increase correlated with an increase in the peak enhancement factor caused by the concentration of energy to this particular

frequency. Heave response is the most influenced by this change. While the rise in the pitch and tension response amplitudes are less than 10%, it is between 10 and 20% for the surge and heave amplitudes as the spectrum becomes narrower.

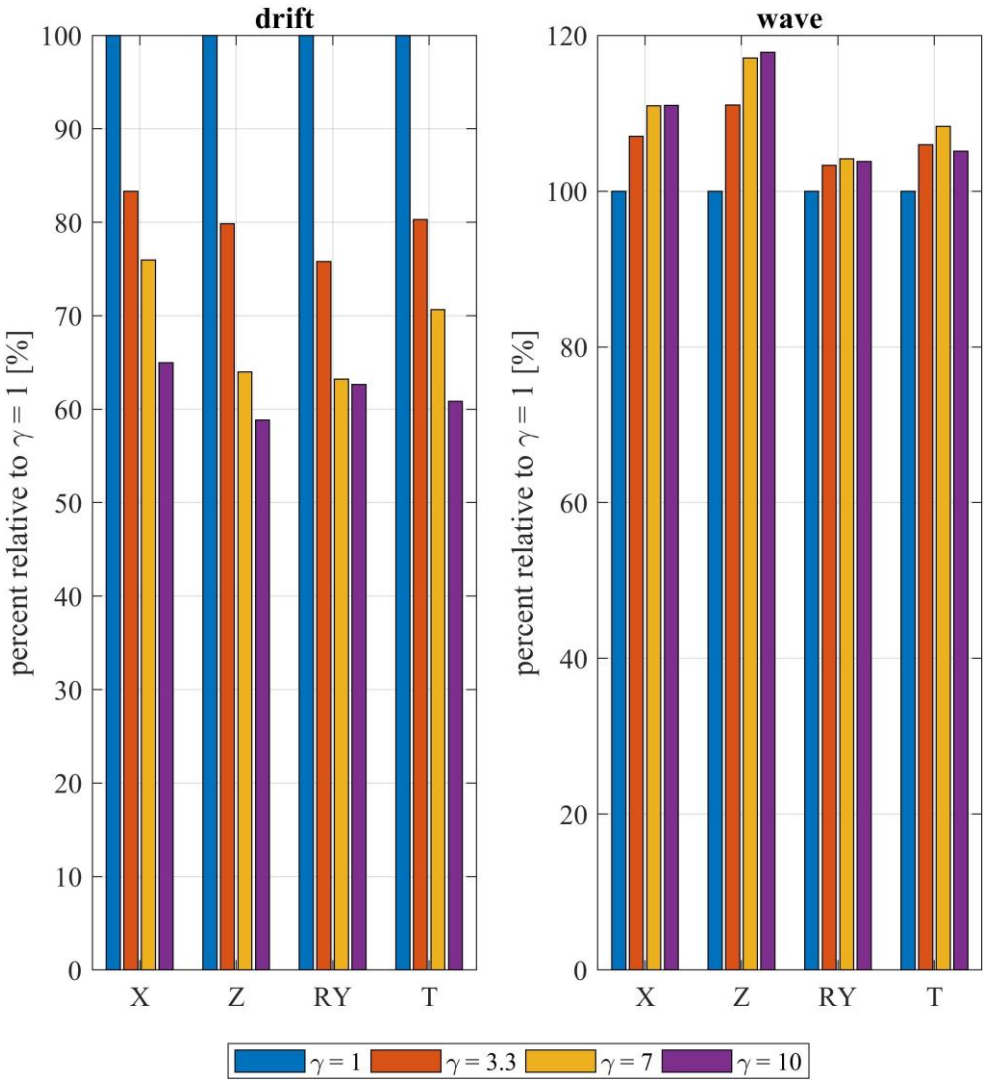

Figure 4.30: Percent change of drift and wave amplitudes in different spectral shape cases relative to the spectrum case with γ=1.0 (moderate case).

Snap load events are inspected as well for various spectral shape loading. The methodology of identifying a snap load event is described in section 3.4. Since the moderate wave is not sufficient to produce any snap loading under any wave groupiness value, snap load is only investigated for the extreme state, and the output is delineated in Figure 4.31. Snap loads increase by 64% when γ increases to 3.3. When the spectrum becomes narrower (higher γ value) the wave groupiness is more pronounced and successive snap loads start to occur and increase as Figure 4.32 demonstrates.

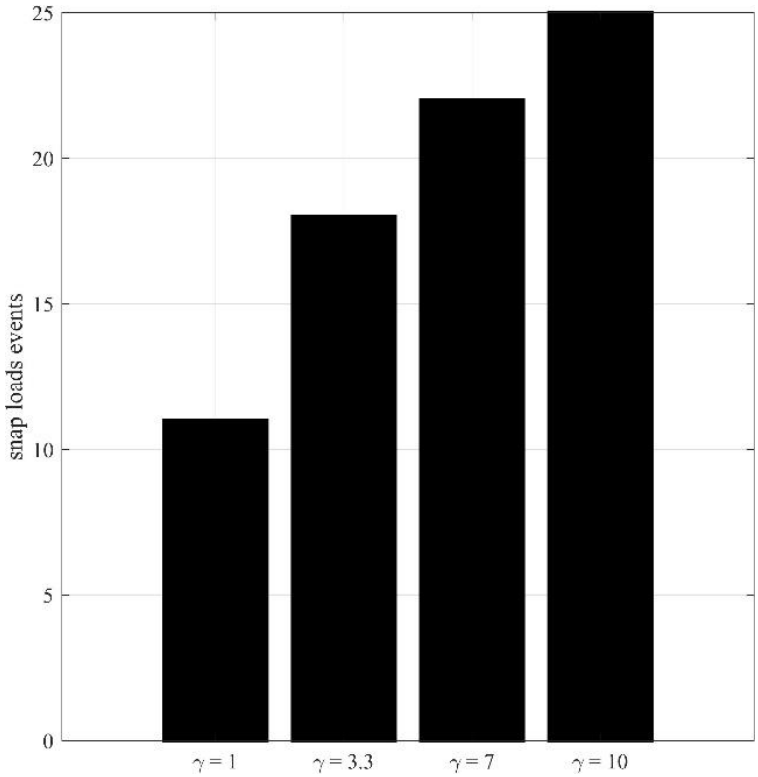

Figure 4.31: Snap load occurrences in the most loaded cable under moderate and extreme waves of different γ values.

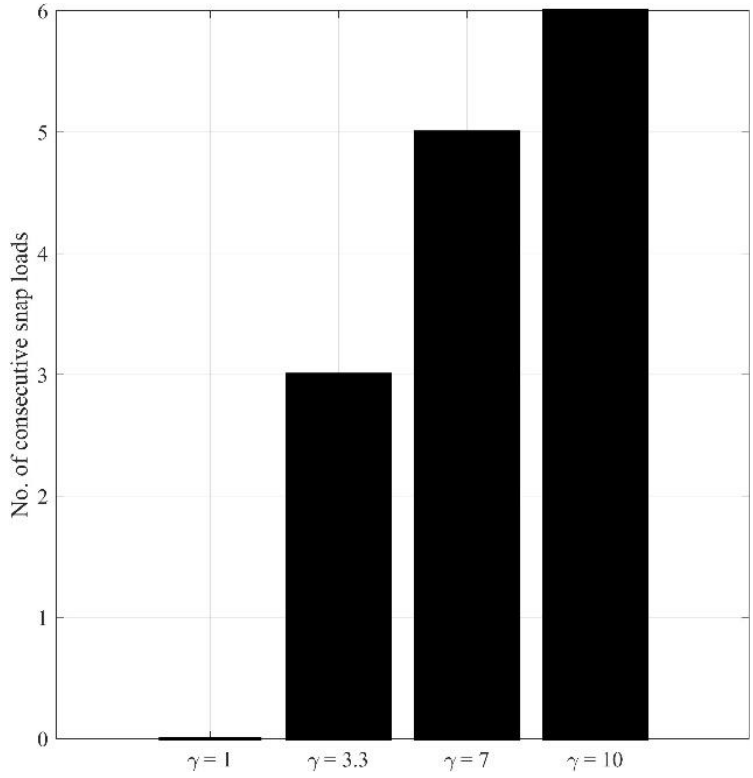

Figure 4.32: Number of successive snapping loads in the most loaded cable under extreme waves of different γ values.

4.5.2. Effect of directional spreading for various wave angles

The spectrum of real sea waves is a function of both frequency and direction $S(\omega, \chi)$:

$$S(\omega, \chi) = G(\omega, \chi)S(\omega) \tag{4.9}$$

in which $G(\omega, \chi)$ is the n^{th}-powered cosine directional spreading function and can be defined as follows:

$$C\cos^n\left[\frac{\pi}{\Delta\chi}(\chi - \bar{\chi})\right] \quad for \quad -\frac{\Delta\chi}{2} < \chi < \frac{\Delta\chi}{2} \tag{4.10}$$

in which n represents the spreading parameter, $\bar{\chi}(\omega)$ is the mean wave direction for each frequency. The constant C is chosen to satisfy that the total energy in both multidirectional and unidirectional spectra are equal. Therefore:

$$\int_{-\frac{\Delta\chi}{2}}^{\frac{\Delta\chi}{2}} G(\omega, \chi) \cdot d\chi = C\int_{-\frac{\Delta\chi}{2}}^{\frac{\Delta\chi}{2}} cos^n\left[\frac{\pi}{\Delta\chi}\chi\right] \cdot d\chi = 1 \tag{4.11}$$

Figure 4.33 illustrates an example of a generated multidirectional wave spectrum with a spreading parameter of $n = 2$ between $-\pi/2$ and $\pi/2$ for the case of a 0° mean direction. As n increases directional spreading decreases and for very high values of n wave becomes closer to being unidirectional.

In this section, sensitivity analysis of the semi-submersible platform response in all DoF and all cable tension to both directions of the wave and wave spreading is performed while keeping other spectral parameters such as wave height and wave peak period constant. Viscous forces are not included in this section due to the difficulty of applying wave kinematics under multidirectional wave excitation, and hence mod1.b is utilized without the damping matrices. The mean direction $\bar{\chi}$ ranges from 0° (aligned with the upwind mooring T1) to 120° (aligned with one of the downwind mooring T3) in intervals of 30°. The arrows in Figure 4.34 depicts the mean direction of waves and arcs highlight the spreading of the multidirectional waves at diverse angles.

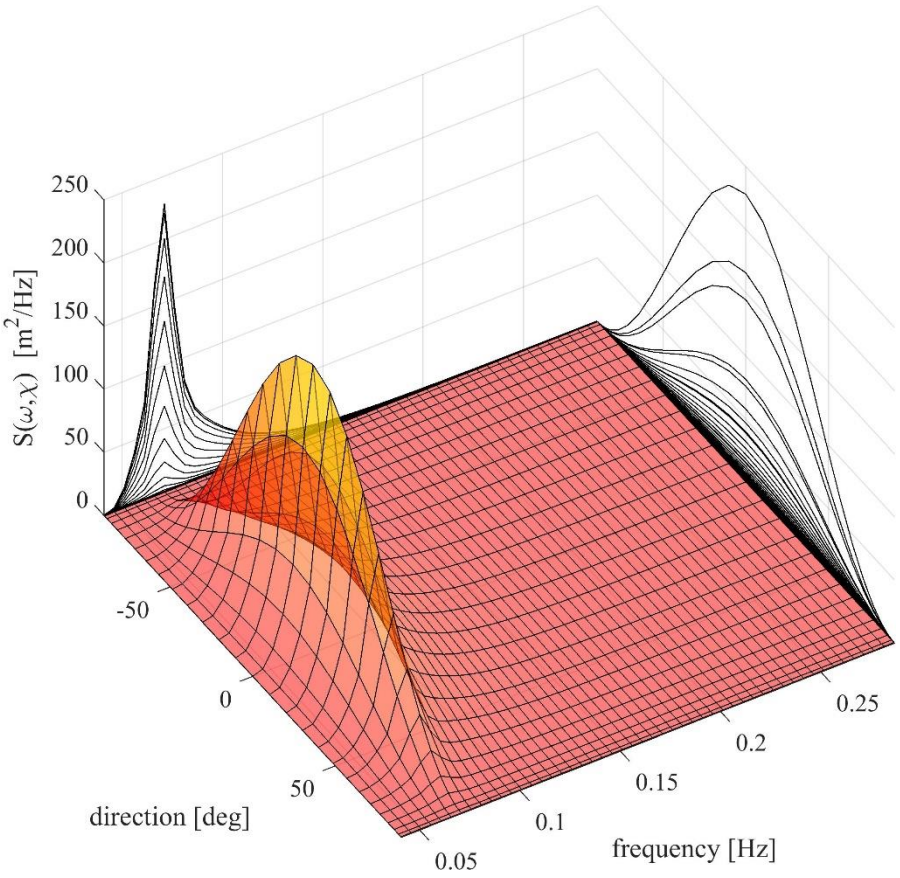

Figure 4.33: Multidirectional wave spectrum as a function of frequency and direction for a mean direction of 0° and a spreading parameter of $n = 2$.

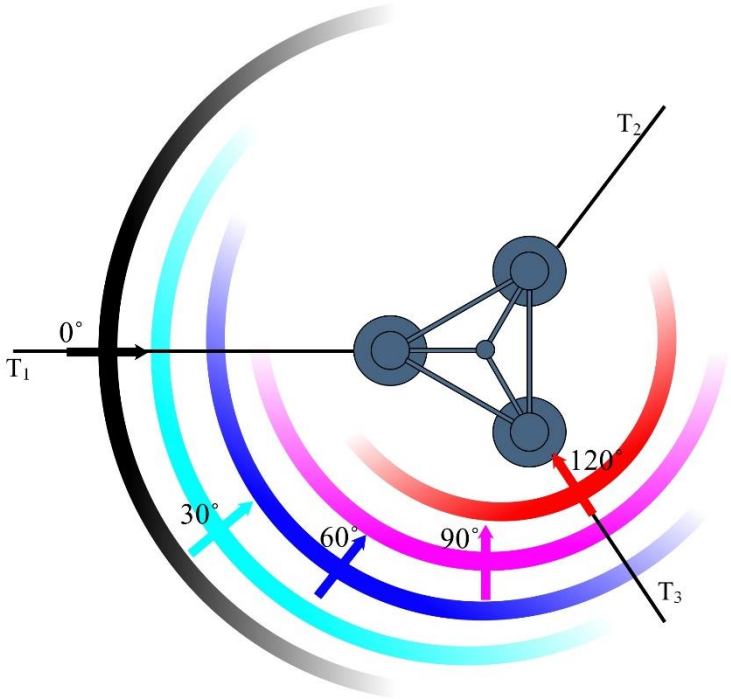

Figure 4.34: A sketch of various angles of uni/multidirectional waves.

The amplitudes of low frequency (LF) and wave frequency (WF) responses are calculated according to the previously mentioned procedure for a unidirectional case and a multidirectional one. The geometrical symmetry of the submerged portion of the platform implies identical responses at different angles and, therefore, results are replicated for the remaining directions.

Figure 4.35 is an illustration of amplitudes under a unidirectional and multidirectional wave excitation from all angles of attack. According to the figure, models using unidirectional waves are conservative (over-predictive) compared to when multidirectional loading is used as far as the axial responses are concerned (surge & pitch in $0°, 180°$; sway & roll in $90°, 270°$), similar to the results of previous studies (Zhang and Ishihara 2016; Waals 2009). However, this pattern reverses for lateral responses (sway & roll in $0°$, $180°$; surge & pitch in $90°, 270°$) where multidirectional waves overpower a uni-directional loading. Therefore, concluding uni-directional being always conservative is not quite truthful.

That said, responses due to multidirectionality surpass those due to unidirectionality only in one-third of all the directions in the horizontal transitions and vertical rotations (X, Y, RX, and RY), especially for the responses in the wave frequency region. The remaining two DoFs (Z, RZ) diverge in their behavior. Uni-directionality provokes more heave, but a multidirectional WF Yaw is seen higher than that excited by a unidirectional load when the wave is aligned with any of the offset columns ($0°, 60°, 120°, 180°, 240°,$ and $300°$), but in low-frequency, multidirectional yaw is small compared to misaligned unidirectional yaw.

Multidirectional amplitudes are generally less susceptible to variance in direction. For instance, as uni-directional surge and pitch take an ∞-like shape, and sway and roll make an 8-like pattern, multidirectional response takes an elliptic form. Heave amplitude does not alter with direction rendering it utterly transparent to where the wave is coming from. Similar transparency is also observed in the WF response of multidirectional yaw.

When comparing LF with WF amplitudes, it is common to observe that in the same direction, the existence of a WF response ensures an LF response as well. Nevertheless, it is noteworthy to underline that, for some cases, despite the absence of a WF motion in a given direction, the structure can still oscillate at low-frequencies in that direction. One example is the uni-directional wave with $90°$ angle. This wave generates

WF fluctuations in sway but not in surge. However, the sway motion creates restorations in the surge direction due to the particular mooring configuration of the OC5 semi-submersible FOWT, which lead to LF surge motions. Such lateral drifts are the reason why slight peaks in LF tension exist at the cable perpendicular to the wave (T1 in 90° and 270°; T2 in 150° and 330°; T3 in 30° and 210°).

Tensions are a function of the absolute fairlead position, which makes their responses asymmetric. They inflate when the wave is aligned with the cable due to the wave-induced mean drift effect. Although it is of a 2^{nd} order nature, it is manifested in the WF response as well because the cable keeps experiencing fluctuations in that frequency while the fairlead is being drifted. The inflation range is $\pm 30^\circ$ and is more apparent in uni-directional events.

Snap loads in the mooring cables under unidirectional and multidirectional waves are also investigated. Although snap loads do occur in uni-directional loading, their presence is significantly reduced when the wave energy is distributed over a wide range of directions. Table 4.13 summarizes the number of snap load occurrences and the mooring line that snap load is detected at for wave directions between 0° and 120°. Snap loads do occur in most directions for a uni-directional event but only in the aligned direction for the multidirectional case. Aligned loading induces the maximum number of occurrence of a snap load such as in T1 and T3 for the directions 0° and 120°, respectively. Under a 30° of misalignment, T1 and T3 are experiencing less than half the number of snap loads when excited by a uni-directional loading compared to an alignment case. When the wave makes a 180° with the cable, tension does peak but snap loads are avoided because the wave induces the platform to drift toward the cable reducing the fairlead-anchor distance, hence reducing the overall tension as seen in the case of 60° with cable T2. These findings are supported by Figure 4.36, which illustrates the horizontal translations of the platform for both uni-directional and multidirectional excitations at the designated directions. The energy is concentrated the most when the surge-sway response shows a straight line, and for this reason, snap load events take place. But even when the wave creates scattering behavior in the surge-sway plane, snap load events can still happen. The energy is well dispersed in the multidirectional incident that the platform does not abruptly cause snap-inducing motions. But investigating snap loads as a function of the spreading of the wave is crucial.

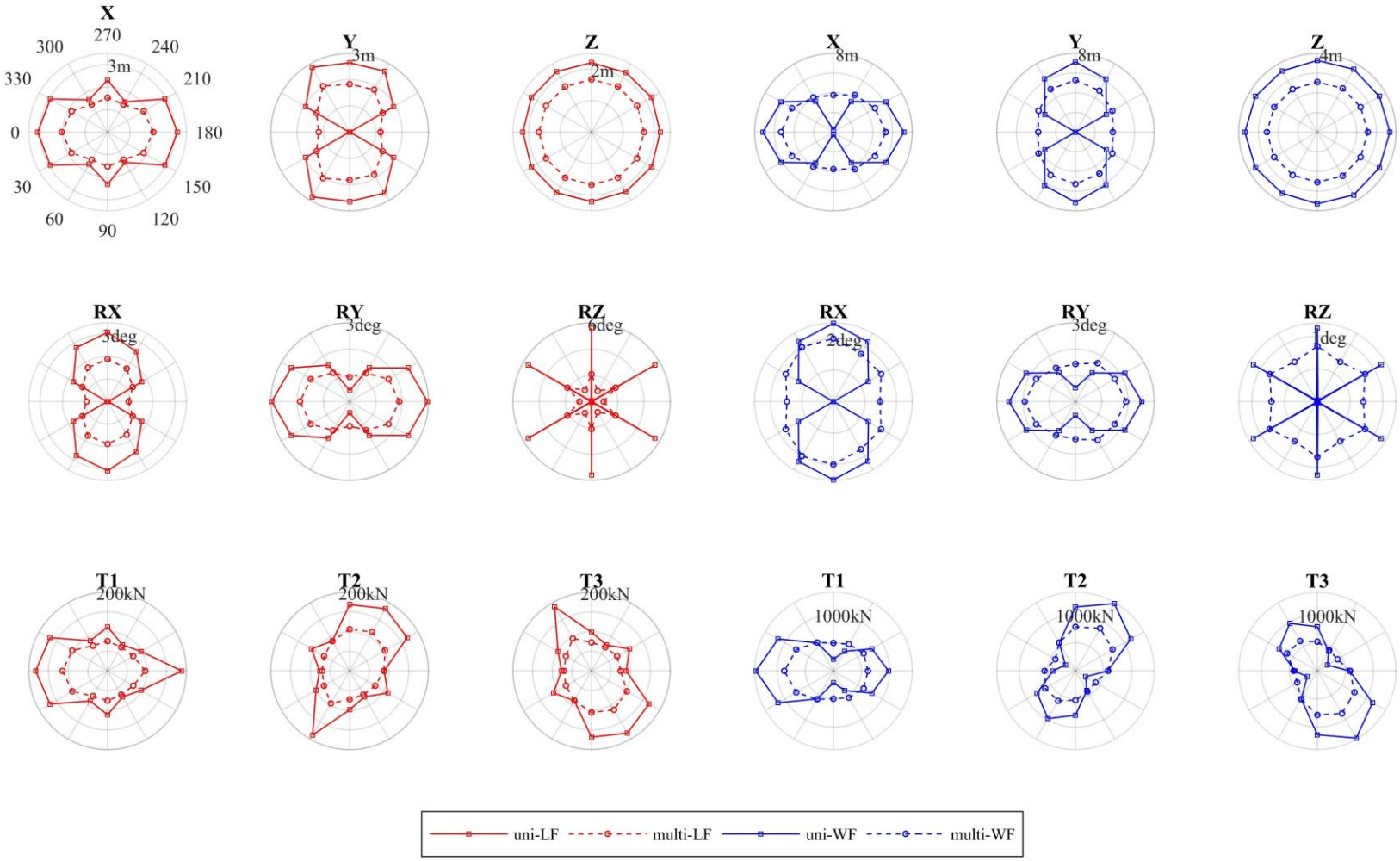

Figure 4.35: Rose plots showing LF and WF response as a function of wave mean direction for both unidirectional and a multi-directional wave excitation. The radii are the responses.

Table 4.13: Snap load occurrences in unidirectional loading at various wave direction.

	Wave direction				
	0˚	30˚	60˚	90˚	120˚
	Uni-directional				
mooring line	T1	T1	-	T3	T3
Snap load occurrence	23	10	-	10	23
	Multidirectional				
mooring line	T1	-	-	-	T1
Snap load occurrence	3	-	-	-	3

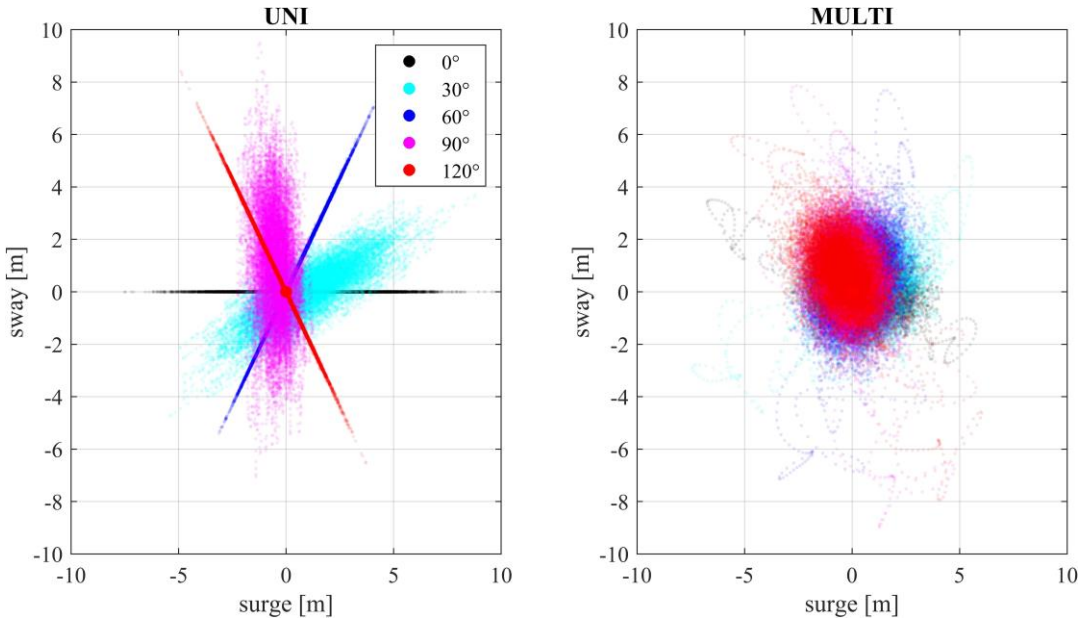

Figure 4.36: Motion in the xy-plane (surge vs. sway) at different wave directions.

To explore the change under various levels of wave multidirectionality, the structure is excited under five spreading parameter values: 2, 4, 6, 20, and 200 for a mean direction of 0˚. The resulting motion is illustrated in Figure 4.37. As anticipated, as the wave becomes less multidirectional, responses approach the unidirectional asymptotic values. Heave does not react to variations in the wave spreading.

Figure 4.37 also shows that the unidirectional assumption produces conservative results, and the slightest spreading ($n = 200$) can marginally lower the primary responses such as surge and tension in T1. Subsequently, this conservatism has a high impact on the number of snap load events, as provided in Table 4.14.

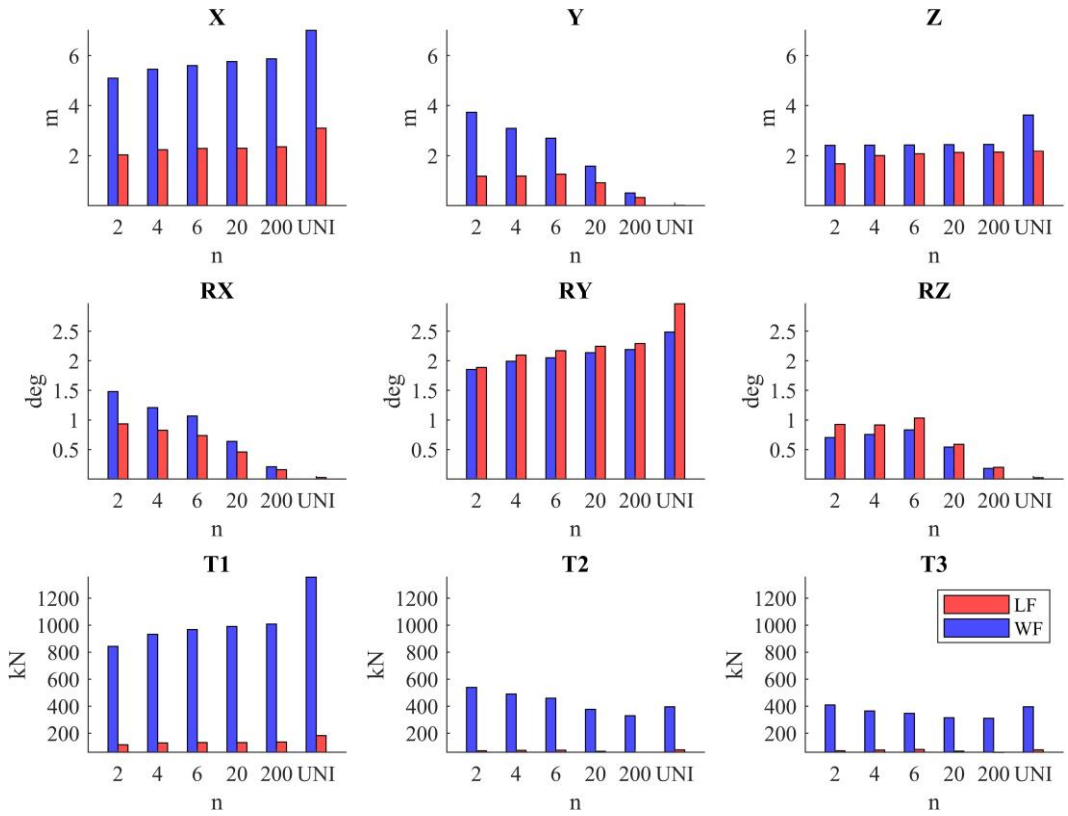

Figure 4.37: Structural motion and cable tensions showing the gradual change between a unidirectional and a multidirectional excitation (n=2,4,6,20, and 200).

Table 4.14: Snap load events as a function of the spreading of the wave.

	Multidirectionality					Uni-directionality
	Spreading parameter (n)					
	2	4	6	20	200	
Snap load occurrence	3	4	6	6	6	23

CHAPTER 5

DESIGN AND NUMERICAL MODELING OF SPAR TYPE PLATFORM

A parametric study is carried out to design a floating spar platform supporting a 300-kW wind turbine. The model is tested numerically, and a 1/40 scaled model is manufactured and will be experimented in the hydraulics lab of the Civil Engineering Department at Izmir Institute of Technology. This chapter focuses on the design of the substructure while considering the masses and inertia of the wind turbine based on hydrodynamic, mooring, and aerodynamic constraints.

5.1. System Definition

The 300-kW wind turbine has the parameters given in Table 5.1 and steady-state thrust values in Figure 5.1. The scaled geometry of the design is illustrated in Figure 5.2 and the parameters used for design optimization. The following constraints are obeyed in the initial stage of the design process:

1- Achievement of hydrostatic equilibrium (see section 3.2.1.2).

2- Assurance of obtaining natural periods (especially in heave and pitch) further from the wave-dominated frequencies.

3- Securing the integrity of the mooring cables under maximum loading possible.

4- Acceptable performance under static wind heeling moment excitation.

Natural periods are computed based on the simplified theoretical approach for calculating added mass explained in Zhu and Lim (2017). Figure 5.3 clarifies the application of their approach to the spar design in this study. Assuming unidirectional loading of 0˚, mass, added mass, and stiffness matrices can be simplified as:

$$M = \begin{bmatrix} m & 0 & mz_g \\ 0 & m & 0 \\ mz_g & 0 & I_{yy} \end{bmatrix} \tag{5.1}$$

$$A = \begin{bmatrix} a_{11} & 0 & a_{15} \\ 0 & a_{33} & 0 \\ a_{51} & 0 & a_{55} \end{bmatrix} \tag{5.2}$$

$$K = \begin{bmatrix} k_{11} & 0 & k_{15} \\ 0 & k_{33} & 0 \\ k_{51} & 0 & k_{55} \end{bmatrix} \tag{5.3}$$

To solve for the uncoupled, undamped natural periods T_{n_j}in surge heave pitch, the following applies:

$$T_{n_j} = 2\pi \sqrt{\frac{m_{jj} + a_{jj}}{k_{jj} + k_{jj_m}}}, \qquad j = 1,3,5 \tag{5.4}$$

Table 5.1: Gross properties of the 300-kW wind turbine.

Rating	300 kW
Rotor Orientation, Configuration	Upwind, 3-blades
Rotor diameter	36 m
Hub height	39 m
Cut-in, Rated, Cut-Out wind speed	2.9 m/s, 9.98 m/s, 25 m/s
hub mass	4.42 t
blade mass	1.77 t
Tower mass	34.90 t

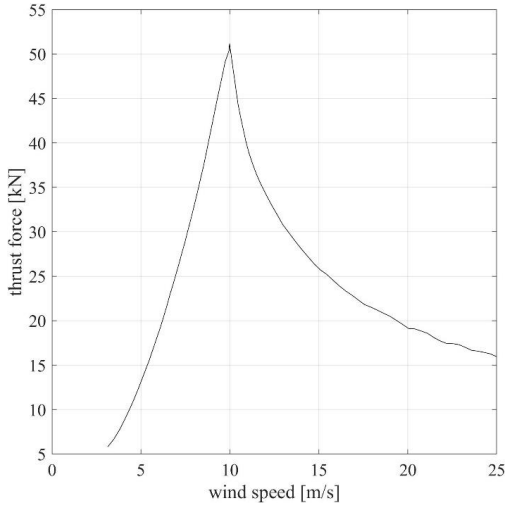

Figure 5.1: Thrust force of the 300-kW as a function with wind speed.

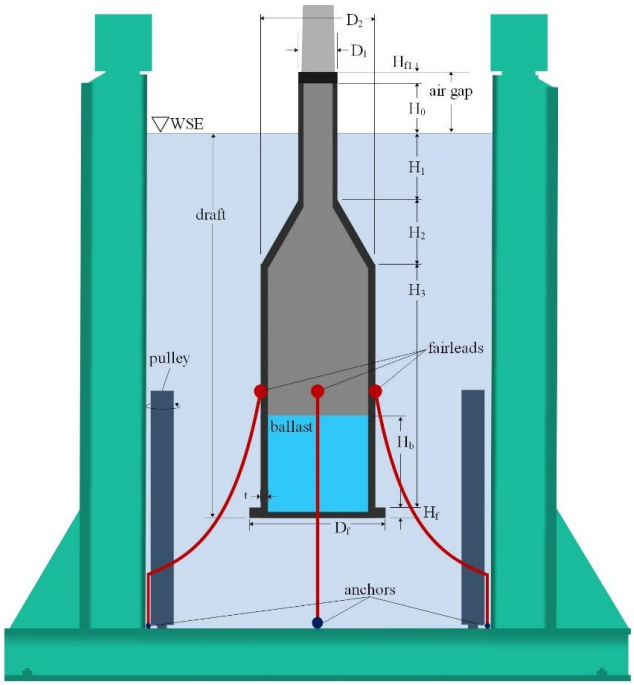

Figure 5.2: Schematic view of the spar-buoy design to be tested (dimensions not to scale).

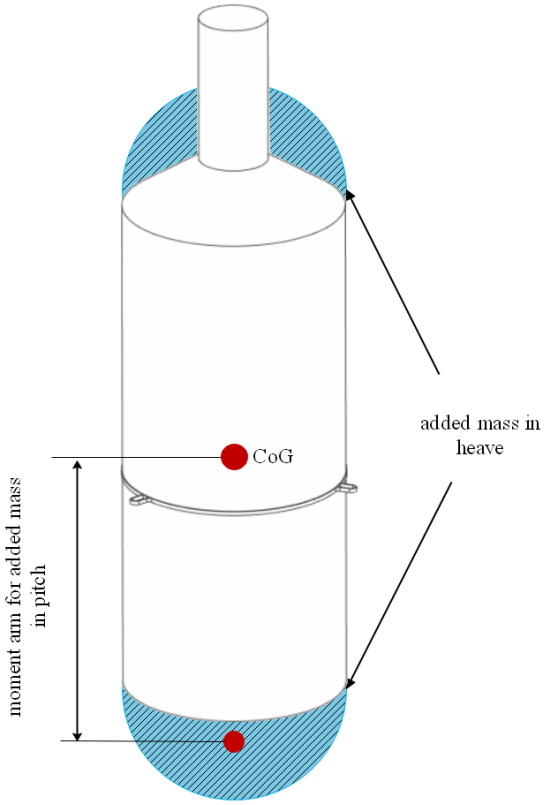

Figure 5.3: A simplified theoretical approach for calculating added mass in heave and pitch.

The application of maximum thrust force F_T at the hub height z_{hub} induces excitations in surge and pitch in a coupled manner:

$$\begin{bmatrix} k_{11} & k_{15} \\ k_{51} & k_{55} \end{bmatrix} \begin{bmatrix} X \\ RY \end{bmatrix} = \begin{bmatrix} F_T \\ M_T \end{bmatrix} \tag{5.5}$$

where M_T is the thrust-induced moment on the platform. It is noteworthy to mention that due to the linear assumption of the mooring restoring stiffness, Eq. (5.5) might not be accurate at high excursions, which is the case under such loading. Nevertheless, it gives an initial judgment and fair comparison between different design points throughout the parametric study.

The problem is implicit since cable design and the structural geometry are dependent upon each other. Therefore, an iterative method is needed. Mooring stiffness value is chosen to allow structural excursion without a snap load occurrence. The fairlead position is best kept at the center of gravity level, where the structure rotates about to avoid any surge-pitch coupling motions.

5.2. Load Case Selection

The design of FOWT requires the joint distribution of wind and wave simultaneously. Wind and wave data are extracted from the DHI MetOcean Data Portal between the years 2010 and 2018 at a specified location along the Turkish coast. The designated region has a depth of 40 m. 50-year return period environmental loading is formulated using these row data through applying a Modified Inverse First Order Reliability Method (I-FORM) (Eckert-gallup et al., 2014). The procedure is explained in Appendix A. This results in a contoured surface originating from a standard normal space shown in Figure 5.4. Along the 50-year contour surface lies the selected load cases (LC) for this study. These load cases comprise irregular waves and steady wind excitation. LC1 represents the highest extremity w.r.t wave height (wave-dominant LC), while LC2 is the most extreme case under wind turbine operation. LC3 embodies moderate thrust and wave height, and LC4 signifies the wind speed that has the highest thrust impact on the turbine (wind-dominant). Table 5.2 summarizes the studied load cases. Note that the mean value of $\gamma = 3.3$ is chosen for all LCs. A constant force of the magnitude prescribed

in Eq. (4.4) to account for the neglected viscous effects. Wind and waves are assumed aligned.

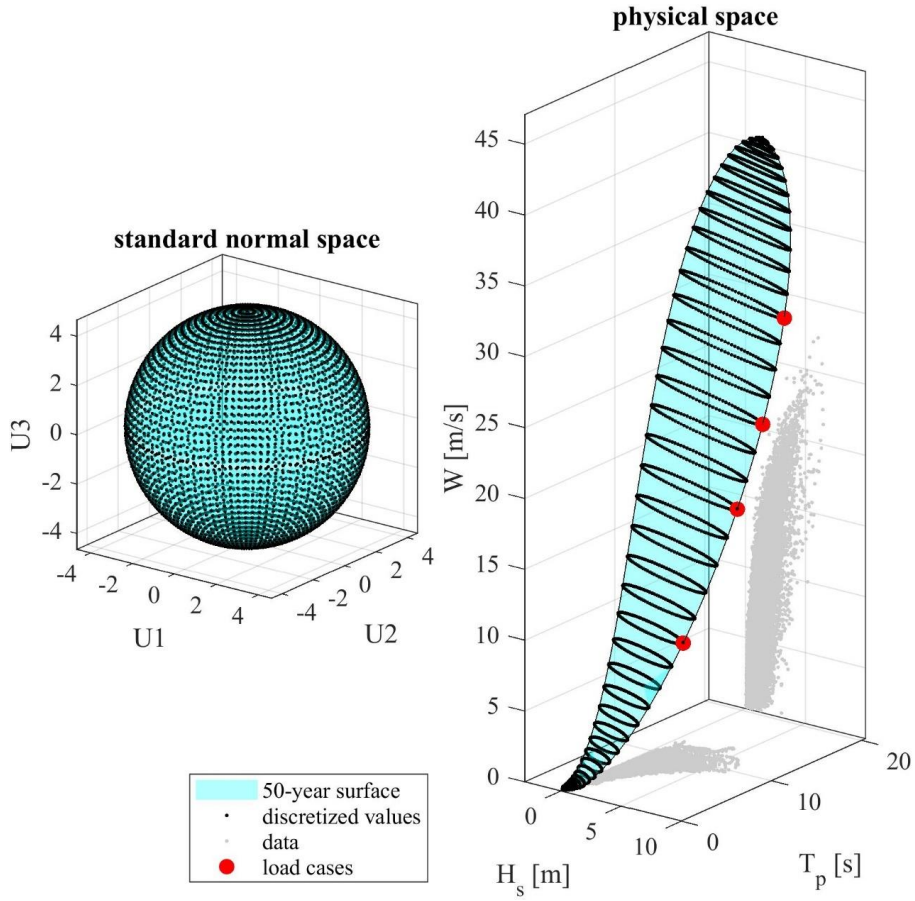

Figure 5.4: Transformation from the standard normal space to the physical space and the load cases' location at the 50-year contour surface.

Table 5.2: Description of load cases used in the design process.

Load case	Wave		Static wind $(W\|H_s)$ [m/s]	Thrust force [kN]	Mean drift viscous force [kN]
	H_s [m]	$T_p\|H_s$ [s]			
LC1	9.67	11.86	32.05*	0	60.65
LC2	9.03	10.33	24.85	16.11	65.04
LC3	7.86	9.07	18.97	20.47	55.30
LC4	5.14	6.70	9.623	48.00	28.50

* over the cut-out wind speed. The wind turbine is shut down. The effect of wind drag forces over the tower and blades is neglected.

5.3. Mooring Design Investigation of Spar-buoy Design

Following the design recommendations in both DNV-GL (2018) & DNV GL (2015), the design tension T_d is described as:

$$T_d = \gamma_{mean} \cdot T_{c,mean} + \gamma_{dyn} \cdot T_{c,dyn} \tag{5.6}$$

where $T_{c,mean}$ is the characteristic mean tension value caused by pretension, static wind, current, and mean drift forces on the structure while $T_{c,dyn}$ is the characteristic dynamic tension induced by the oscillatory nature of the environmental loading, such as the low-frequency and wave-frequency responses. γ_{mean} and γ_{dyn} are load factors taken as 1.3 and 1.75, respectively, for an ultimate limit state (ULS) of consequence class 1 (DNV-GL, 2018). For time-domain analysis, $T_{c,mean}$ is simply the mean tensile force of the most loaded cable and the characteristic dynamic tension is the most probable maximum of the response T_{MPM} minus the mean value:

$$T_{c,dyn} = T_{MPM} - T_{c,mean} \tag{5.7}$$

Load cases are run ten times each, with a sea-state duration of 3-hours. The maximum tension values are then fit to an Extreme Value Distribution (Gumbel). T_{MPM} corresponds to the 37% percentile of the distribution (see Figure 5.5).

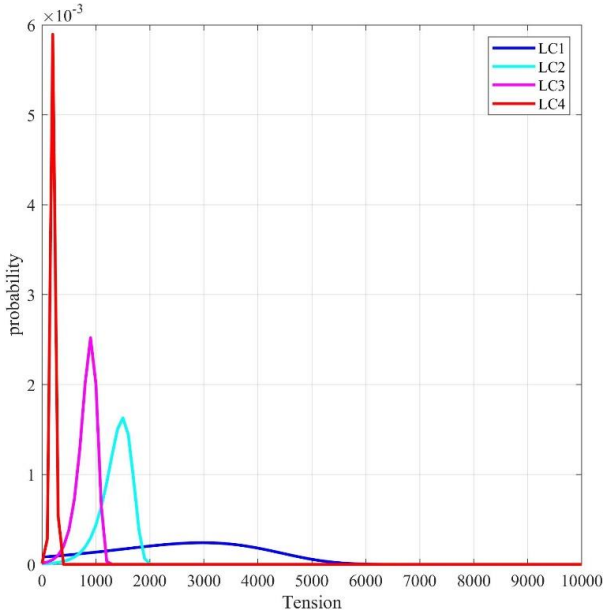

Figure 5.5: Gumbel distribution of 3-hour maximum tension values in all load cases.

Design tension is contrasted with the characteristic capacity of the chain used. Assuming the weakest chain grade of R3, the minimum breaking capacity is (IACS, 2013):

$$S_{mbs} = 0.0223d^2(44 - 0.08d) \tag{5.8}$$

Such that d is the nominal diameter of the chain in mm. The characteristic capacity (S_c) is:

$$S_c = 0.95\, S_{mbs} \tag{5.9}$$

Figure 5.6 illustrates that load case 1 must be adopted as it leads to the highest design tension. It seems thrust force and mean surge of the structure is not the governing factor (LC1>LC2) but rather the dynamic tensions resulting from severe wave excitations. Design tension is safe under the mooring properties initially chosen. When checking for snap loads, it was revealed that pretension must be slightly reduced to eliminate any tensions that are higher than the characteristic capacity. The final choice is a pretension of $T_0 = 34\ kN$. With this option, snap load peaks are reduced below the threshold, as seen in Figure 5.6.

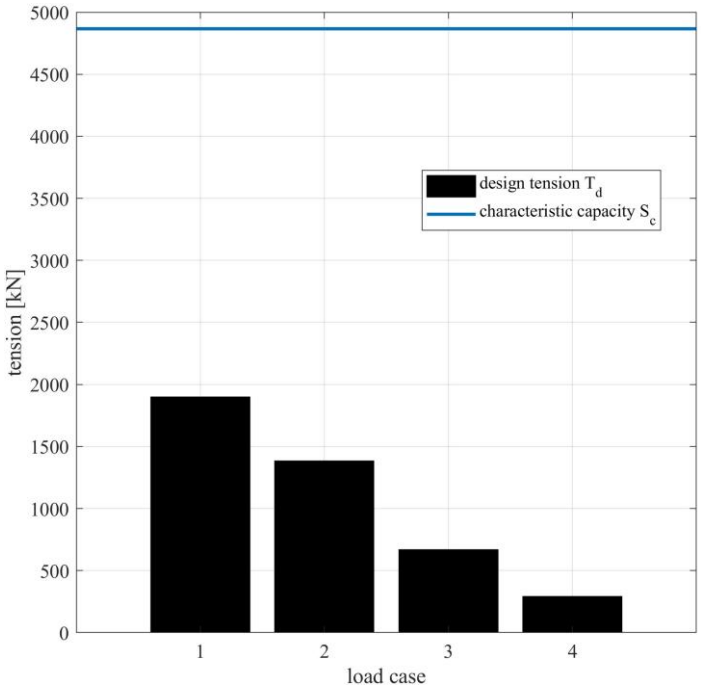

Figure 5.6: Design tension for different load cases compared to the characteristic capacity of the chain.

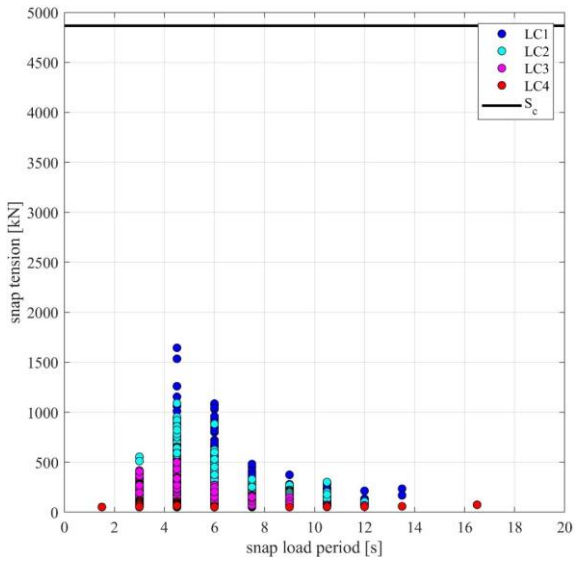

Figure 5.7: Snap load events in all load cases.

Mooring stiffness is delicately chosen to reduce snap peaks while allowing for surge acceptance excursion of up to $\pm 10\ m$ without the cable being taut. The cable is deprived of its slackness when it is fully suspended in the fluid, and no portion is kept laid on the seabed. Therefore, laid length only reaches zero when maximum surge excursion is reached. Figure 5.8 portrays the seaward cable geometry in the accepted excursion region, and the resulting laid portion length is plotted in Figure 5.9.

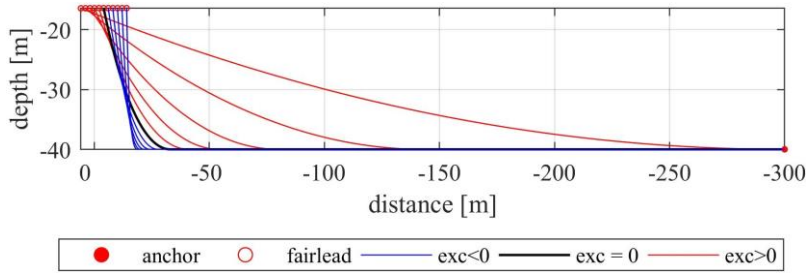

Figure 5.8: Catenary cable geometry with platform excursions of the range exc = $\pm 10\ m$.

The experiment is to be run in a wave flume instead of a basin, which imposes restrictions on the mooring lines configuration. The downwind cables are to be truncated. But, to preserve the angle between the mooring lines and their geometrical and elastic compliances, an original vertical pulley-based system is introduced where the cable direction is deviated and kept inside the wave flume as delineated by Figure 5.2 and Figure 5.10. The main advantage of this truncated system is that it keeps mooring-induced

stiffness relatively similar for a wide range of excursions (see Figure 5.11). Table 5.3 specifies the final mooring design adopted.

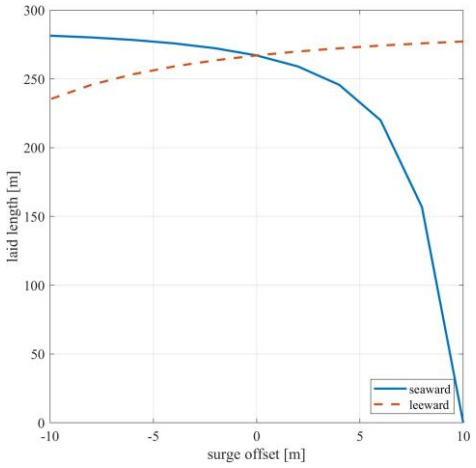

Figure 5.9: Laid length of the cable as a function of static surge offset in the seaward and leeward cable.

Table 5.3: Mooring system properties of the spar-buoy design.

Property	Value
Chain type	Catenary line - Studless chain
Mass per unit length in air	0.121 t/m
Mass per unit length in water	0.112 t/m
Nominal diameter	0.0779 m
Equivalent diameter	0.1404 m
Axial Stiffness, EA	5.1989e+05 kN
Angle between lines	120°
Cable pretension	34.814 kN
Radius to fairlead from the centerline	4.08 m
Depth to fairlead below water level	16.44 m
Radius to anchor from the centerline	300 m
Depth to anchor below water level	40 m
Seaward cable length	306.23 m
Seaward initial cable laid length	270.11 m
Truncated leeward cable length	166.80 m
Truncated leeward initial cable laid length	130.75 m

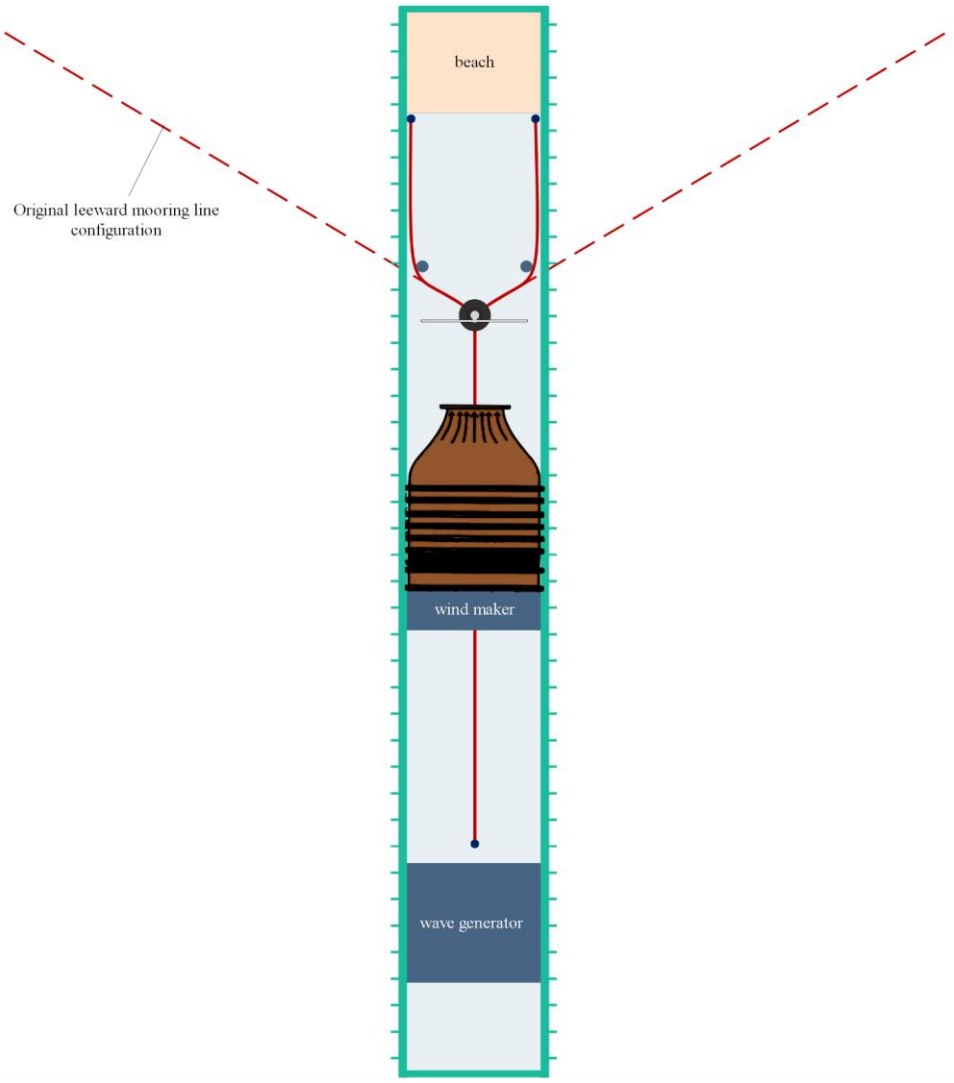

Figure 5.10: Top-view of the wave flume and the original and truncated configuration of the mooring system.

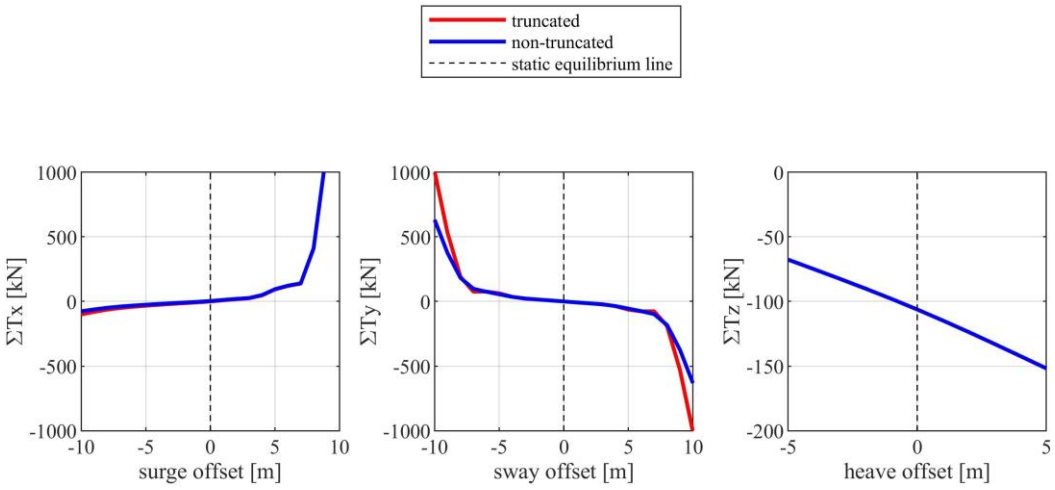

Figure 5.11: Mooring stiffness for truncated and non-truncated configurations as a function of static translational offsets.

5.4. Parametric Optimization

The spar design optimization comprises two objective functions; maximizing metacentric height $\mu_1(x)$ while keeping the natural periods far from the wave-dominated region $\mu_2(x)$. These two objectives are contradictory to one another. Increasing $\overline{GM}$, provides static restoring moment but lessens the pitch natural period. Therefore, a set of optimal solutions is obtainable. These solutions are referred to as Pareto optimal solutions in which the enhancement in one objective results in the worsening of the other (Mattson, Mullur, and Messac, 2004). Hence, a trade-off must be done. Figure 5.12 illustrates the design point and the feasible region based on what data points satisfy all the constraints previously mentioned. The desired solution along the Pareto frontier is chosen by giving arbitrary weights $(w_1; w_2)$ that indicate the importance of each objective:

$$J(x) = w_1\mu_1(x) + w_2\mu_2(x) \tag{5.10}$$

where $J(x)$ is the aggregate objective function (AOF). The anchor points are attained when optimizing one of the objective functions regardless of the other. Giving equal importance to the two objectives, we get the desired solution.

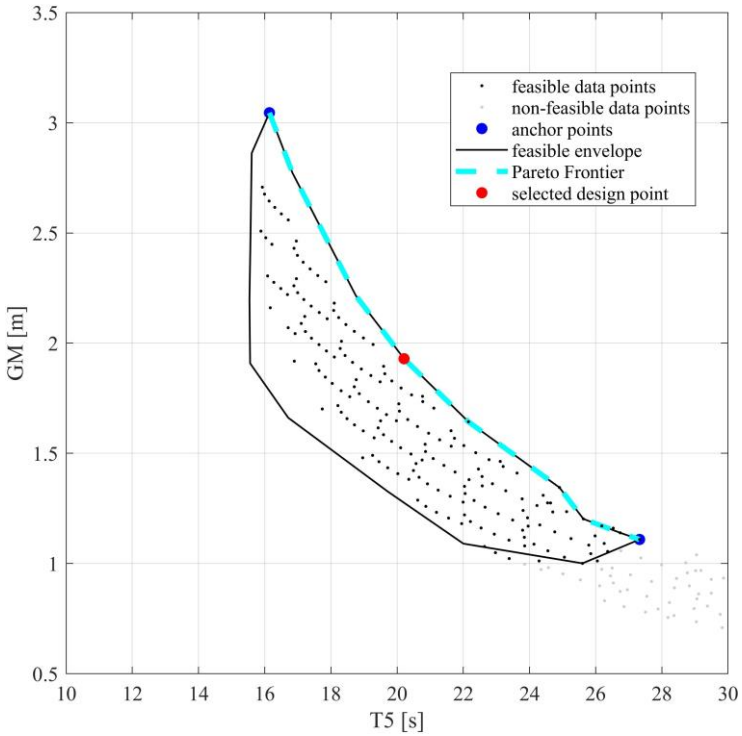

Figure 5.12: Feasible space, Pareto Frontier, and the selected design point. The x-axis is natural period in pitch, and the y-axis is the metacentric height.

The natural periods are in the safe zone as seen in Figure 5.13. The optimal design has the characteristics given in the tables below. Figure 5.14 also provides detailed sketch of the geometric parameters in the model scale.

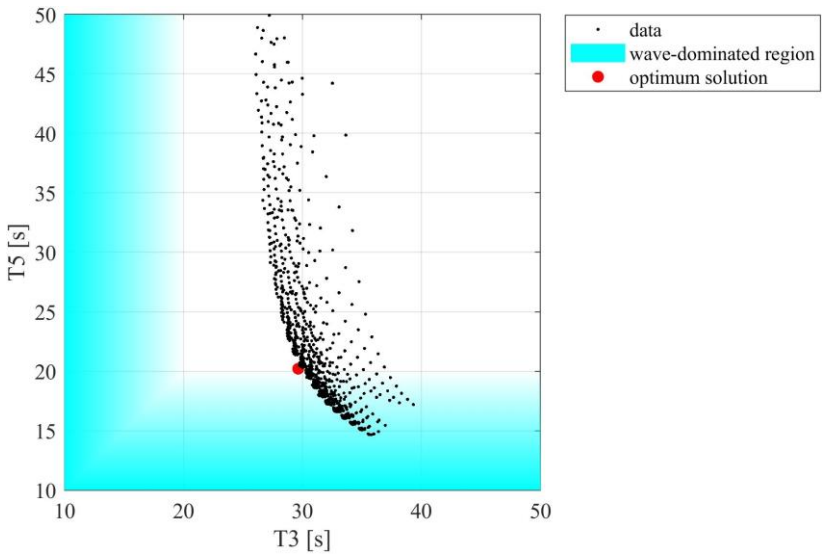

Figure 5.13: Natural period resulting from the parametric study and their proximity to the wave-dominated region and the optimum solution in the heave-pitch natural period plane.

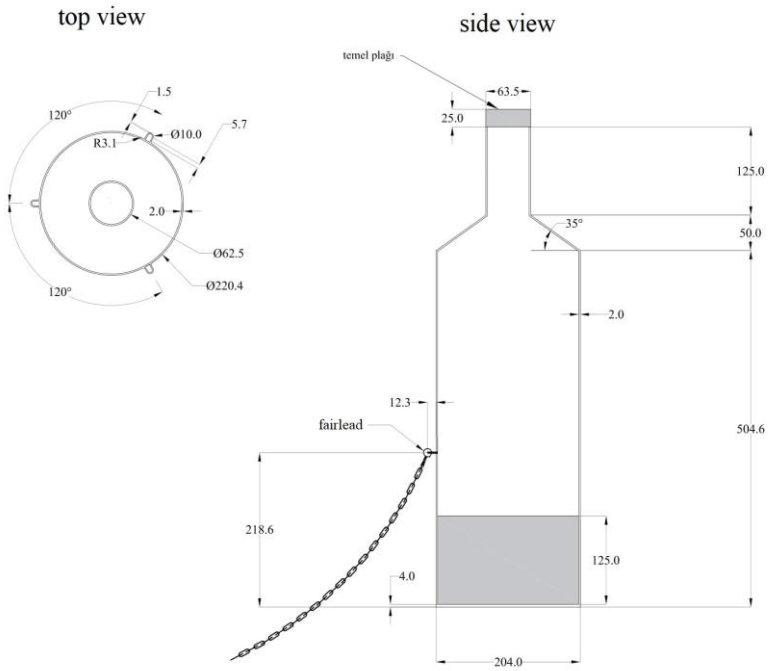

Figure 5.14: Side and top view of the scaled model dimensions after optimization (dimensions are in mm).

Table 5.4: Spar-buoy structural and hydrostatic properties.

Property	Value
Mass	1.100e+03 t
Draft	25.344
Volumetric displacement	1.121e+03 m^3
Roll inertia	1.965e+05 $t.m^2$
Pitch inertia	1.965e+05 $t.m^2$
Yaw inertia	4.155e+03 $t.m^2$
CoG below water level	16.439 m
CoB below water level	14.516 m
Metacentric height GM	1.925 m
Water-plane area	5.067 m
Static buoyancy force	11.068 kN
Heave hydrostatic stiffness	49.39 kN/m
Roll hydrostatic stiffness	369.558 kN.m/deg.
Pitch hydrostatic stiffness	369.558 kN.m/deg.

Table 5.5: Structural material used for spar-buoy design.

Material	Structural part	Density
Concrete	Ballast, the foundation layer	2.40 ton/m3
Steel	Tower, RNA assembly	7.90 ton/m3

Table 5.6: Optimized parameters for spar-buoy design.

Parameter	Value [m]
D_f	8.16
D_2	8.16
D_1	2.54
H_f	0.16
H_b	5.00
H_3	20.18

(cont. on next page)

(table cont.)

H_2	2.00
H_1	3.00
H_0	2.00
H_{f_1}	1.00
t (thickness)	0.08

5.5. Full-System Analysis

The second reference system described in section 3.1 with the origin O' is at the CoG of the platform is used here The first test done is to ensure the structure is statically stable by running an equilibrium test in still water with no environmental loads. The mean offsets in all DoF are presented in Table 6. The greatest offsets are in surge direction and pitch rotation, which corresponds to the small eccentricity in the center of mass of the full system projected by the masses of hub and blades. Surge and pitch excursions due to maximum thrust force on the hub are given in Table 5.8.

Table 5.7: Static equilibrium values of displacement and rotational modes for spar-buoy.

Surge	Sway	Heave	Roll	Pitch	Yaw
0.08 m	1.3e-4 m	0.025e-2 m	-2.84e-5°	-0.31°	-9.77e-5°

Table 5.8: Wind heeling moment responses for spar-buoy.

Surge	6.13 m
Pitch	6.845°

Next are the fully coupled, damped natural periods of the system. It must be assured they lie in regions far from primary excitations of wind and wave, natural modes of the tower, and blade-passage frequency. They are calculated using the method of Eigen analysis. The platform tested here is the one with the truncated mooring cables. The theoretical values of heave and pitch calculated at the initial stage of the design agree well with the output of Eigen analysis.

Table 5.9: Natural periods of the spar-buoy platform.

DOF	Surge	Sway	Heave	Roll	pitch	yaw
Natural periods [s]	49.49	156.92	29.92	20.39	20.27	21.04

The system is then tested under the same 50-year random waves in time-domain with the application of two-point forces, one at the hub height representing a static thrust force and another at the center of mass mimicking a mean drift viscous force as described in Table 5.2. The responses in FD are displayed in Figure 5.15. While motion responses peak at two frequencies (LF & WF), tensions tend to rise at the high-frequency (HF) as well, especially in extreme conditions. Snap loads are characterized by low periods and are responsible for these excitations. For the sake of illustration, the actual tension response is filtered through low-pass and high-pass filters, and the results are provided in Figure 5.16 in TD and FD to demonstrate the slowly/fast varying responses. HF signal is observed to peak when snap load or near-snap load events occur. A time-domain statistical summary is provided in Table 5.10 for the major responses.

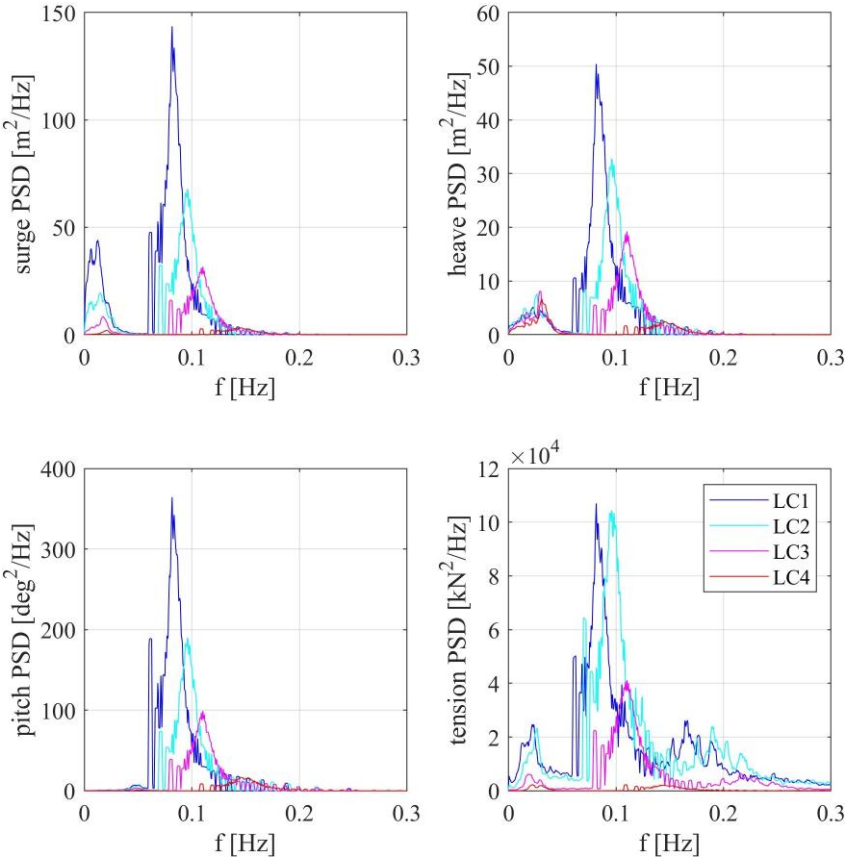

Figure 5.15: Spectral density of primary responses under various wind and wave loading.

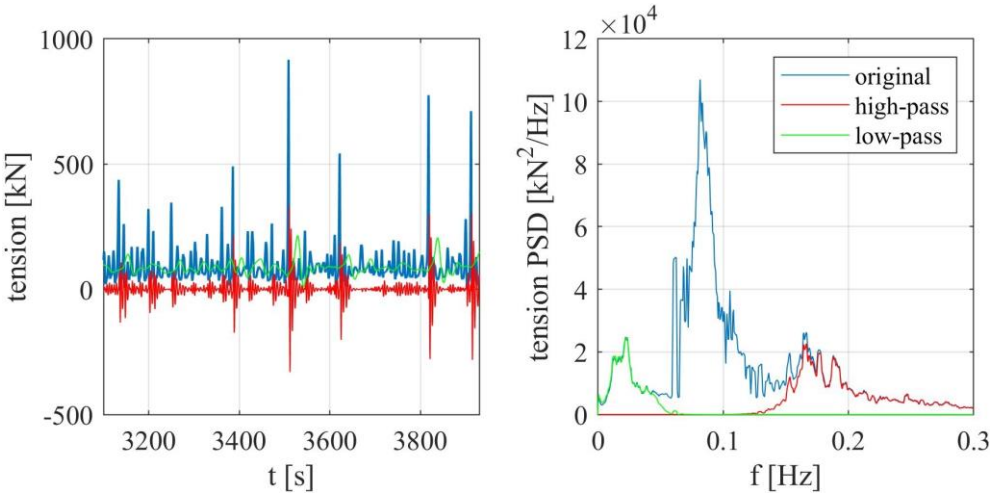

Figure 5.16: Actual response and a low and high-pass filtered response of the tensile forces in the seaward cable in time (left) and frequency (right) domain for LC1.

Table 5.10: Time-domain statistics for the main DOF and the cable tension.

statistic	**LC1 (wave dominant)**	**LC2**	**LC3**	**LC4 (wind dominant)**
	X			
Mean	4.18	5.02	5.11	5.22
Std. Dev.	1.90	1.44	0.99	0.38
Max.	8.96	8.69	7.85	6.48
Min.	-6.23	-2.69	0.54	3.76
	Z			
Mean	-16.07	-16.13	-16.13	-16.22
Std. Dev.	1.11	1.00	0.81	0.45
Max.	-11.44	-11.98	-12.64	-13.59
Min.	-19.70	-19.34	-18.65	-17.79
	RY			
Mean	-0.29	1.88	2.52	6.34
Std. Dev.	2.85	2.25	1.70	0.82
Max.	10.07	10.03	8.90	9.59

(cont. on next page)

(table cont.)

Min.	-11.20	-7.36	-4.38	2.84
	T			
Mean	88.32	107.66	102.27	103.54
Std. Dev.	70.76	72.23	42.19	11.90
Max.	1575.10	1223.20	696.64	230.32
Min.	-172.17	-209.16	-54.09	41.42

CHAPTER 6

INNOVATIVE DESIGN

This chapter is dedicated to the development of an innovative geometry for the floating platform supporting the 5-MW wind turbine described in section 4.1. The design is supposed to be simple and economically feasible while inherently providing sufficient resistance to wave actions. The initial design procedure mentioned in the previous chapter is borrowed with some additional adjustments.

The novel design geometry is thought to be an intermediate solution between a high-draft platform, such as OC3-Hywind spar-buoy, and a high water-plane area that characterizes semi-submersible designs while inheriting the reduced heave response of a spar and the pitch response of the semi-submersible. Regions in proximity to the wave surface ought to have a smaller exposed area than the lower ones. The proposed geometry has an inverted funnel shape (Figure 6.1). The side curves are circular arc (they can be any other function), and the geometrical properties that define the form are the arc angle θ_{arc}, the neck diameter D_N, and the draft d. By changing these parameters (especially D_N and d), the resemblance of the new design to the spar-buoy and the semi-submersible can be controlled. The parametric search for the best arrangement is based on the variation of these parameters.

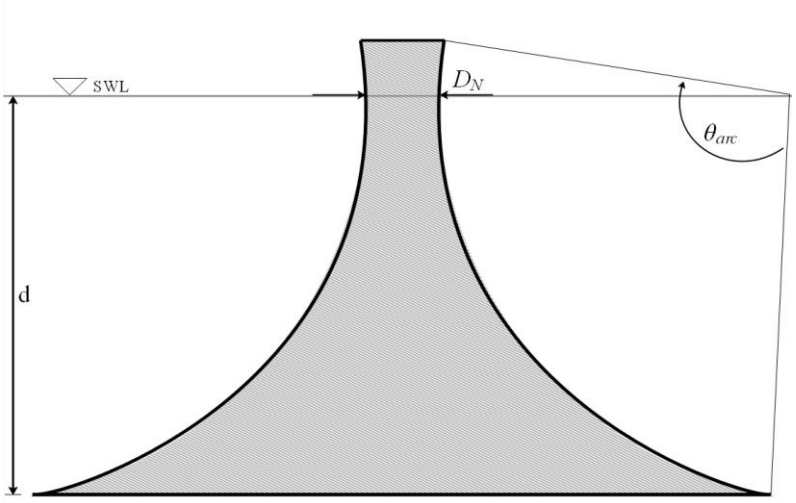

Figure 6.1: Proposed shape for the innovative platform.

For one set of alternating parameters, the procedure for achieving a design is illustrated in Figure 6.2. The novel design aims to achieve sufficiently reduced excitations in the vertical DoFs. Hence, the platform design is restricted to the following constraints:

1- Vertical equilibirium must be ensured through Eq. (3.10).

2- Wind heeling-induced pitch rotation must be less than 3°, a value arbitrarily chosen to be lower than the 10° limit recommended by Wayman (2006) for better static stability.

3- Natural periods in the vertical DoF (heave, roll, & pitch) must be well above the wave-dominated region for better dynamic stability.

4- Material cost must be limited.

5- High inertia in roll and pitch rotation.

The geometry is firstly tested for a vertical equilibrium without internal ballast. If it is light to support the wind turbine under the prescribed draft, the extra weight to be added to the system defines the mass of the internal ballast m_b. The ballast must be the right combination of light and heavy material (sand and seawater are used here) that produces the center of ballast C_B to get the desired CoG subjected to the wind heeling moment constraint (pitch rotation set to not more than 3°). Then, vertical equilibrium is rechecked. Usually, this gets satisfied from the first loop, but if that is not the case, the meshing size is refined, and the procedure repeats itself. When reaching a design, shell thickness is checked against buckling loads. If the shell wall is made of steel, it is arbitrary to add a constraint restricting the thickness of the steel to keep steel mass equal to that of the DeepCwind semi-submersible platform.

The neck diameter D_N must be chosen to provide sufficient hydrostatic heave stiffness, while keeping the natural period in that mode high enough. The high draft has a direct effect of increasing buoyant force, and therefore, the additional ballast mass to be added to counterweigh that force. The more internal ballast, the higher the inertia of the system becomes, raising the natural period in the rotational modes (see Eq. (5.4)). The roll and pitch inertia is preferably chosen to be higher than $2e+07\ t \cdot m^2$. Table 6.1 sums up the constraints and limitations. A design example is proposed here, and the chosen parameters and platform properties are provided in Table 6.2, hydrostatic features in Table 6.3, and mooring system in Table 6.4. Note that there are two proposed designs

that have identical geometries. One with a steel shell and the other is made of concrete. They are named as Bell and BellC, respectively, due to their bell-like shape (see Figure 6.3 & Figure 6.4). When the properties of the two designs are different, their names are assigned to their values.

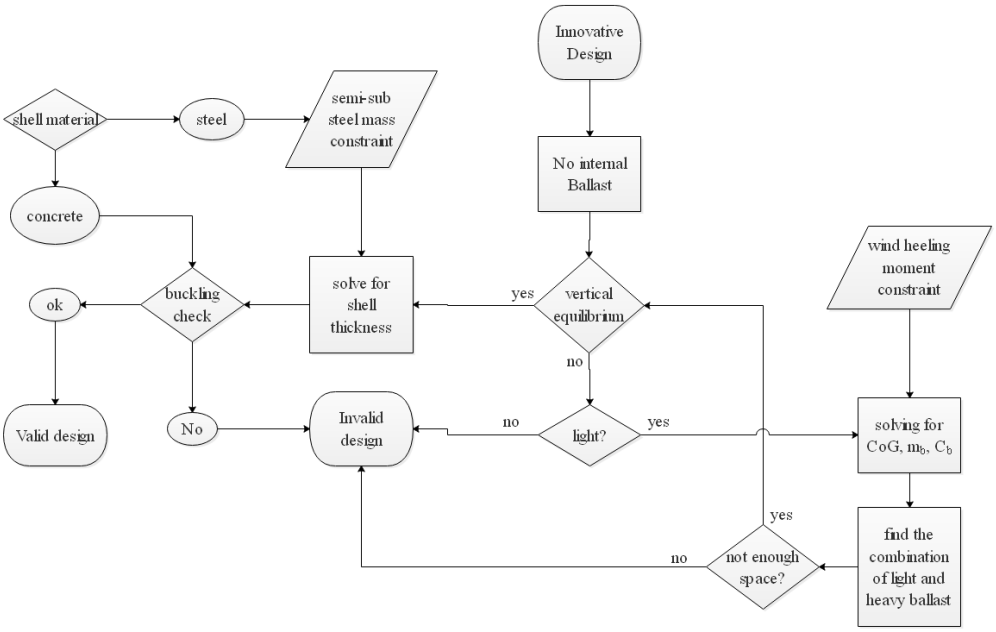

Figure 6.2: Flowchart explaining the procedure of a one-design point for the innovative geometry.

Table 6.1: Summary of the design constraints.

Constraints & Limitations	Values
Metacentric height $\overline{GM}$	$>$ 1m (DNV-GL, 2018)
Roll/pitch inertia I_{xx}	$> 2.0e + 07$ t $\cdot$ m^2
Wind heeling-induced maximum offset	$<$ 7 m
Wind heeling-induced maximum moment	$< 3^{\circ}$
Natural periods in heave and pitch	$> 40\ s$

Stability is mostly achieved by the immense amount of ballast, explicitly categorizing the novel platform as a ballast-stabilized one. Its location in the renowned pitch stability triangle is allocated, as seen in Figure 6.5. These positions are calculated

according to the contribution of buoyancy, ballast, and mooring to the overall pitch stiffness.

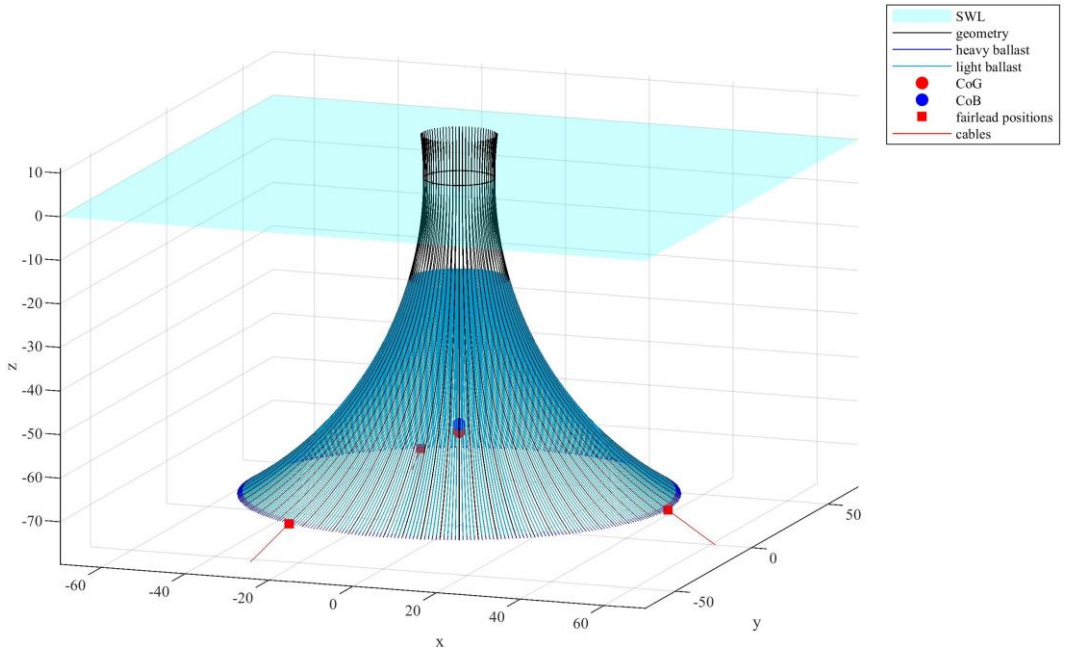

Figure 6.3: Innovative model geometric configuration.

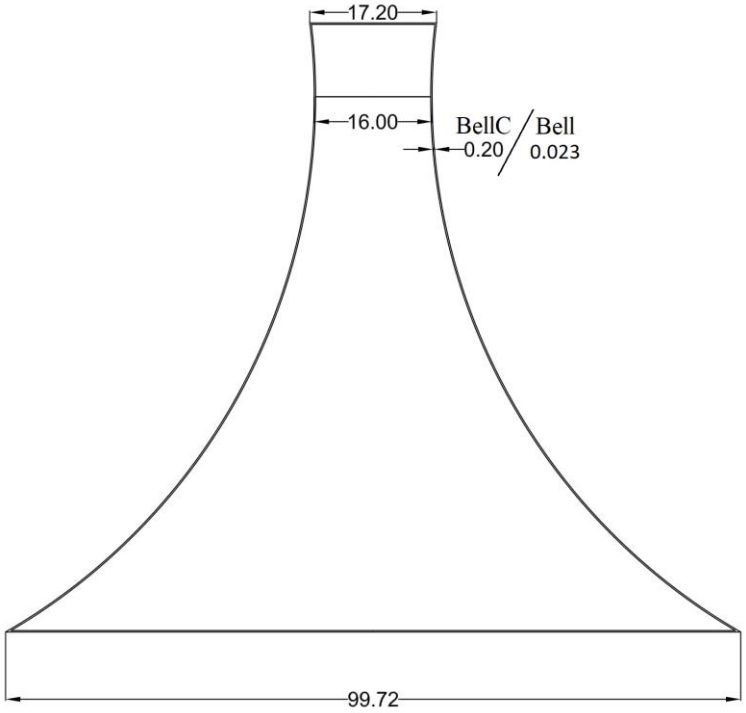

Figure 6.4: Innovative model dimensions in m.

Table 6.2: Design example parameters and platform structural properties.

Parameter	Values
Diameter neck D_N	16 m
Draft d	72.5 m
Arc angle θ_{arc}	60 deg.
Thickness t	0.023 (Bell) 0.2 (BellC)
Shell material	$\rho_s = 8.0\ t/m^3$ (Bell) $\rho_s = 2.4\ t/m^3$ (BellC)
Ballast material	6% sand, 94% seawater (Bell) 2% sand, 98% seawater (BellC)
Shell mass m_s	3.85E+03 t (Bell) 9.99E+03 t (BellC)
Ballast mass m_b	1.23E+05 t (Bell) 1.18E+05 t (BellC)
Elevation to the tower base (air gap)	10 m
Greatest radius from centerline	49.8579 m
Depth to CoG	58.1908 m (Bell) 58.3975 m (BellC)
Roll inertia I_{xx}	2.87E+07 $t \cdot m^2$ (Bell) 2.86E+07 $t \cdot m^2$ (BellC)
Pitch inertia I_{yy}	2.87E+07 $t \cdot m^2$ (Bell) 2.86E+07 $t \cdot m^2$ (BellC)
Yaw inertia I_{zz}	9.62E+05 $t \cdot m^2$ (Bell) 2.49E+06 $t \cdot m^2$ (BellC)

Table 6.3: Hydrostatic properties of the innovative floating platform.

Displaced water volume ∇	1.26E+05 m^3
Depth to CoB	56.485 m
Static buoyancy force F_B	1.26E+06 kN

(cont. on next page)

(table cont.)

Hydrostatic restoring in heave k_{33}	1.99E+03 kN/m
Hydrostatic restoring in roll k_{44}	3.77E+04 kN · m/deg (Bell) 4.27E+04 kN · m/deg (BellC)
Hydrostatic restoring in pitch k_{55}	3.77E+04 kN · m/deg (Bell) 4.27E+04 kN · m/deg (BellC)
Water-plane area A_{wp}	198.07 m^2
Metacentric height $\overline{GM}$	1.731 m (Bell) 1.937 m (BellC)

Table 6.4: Chain properties of the mooring cable for the innovative design.

Linear density in air	0.1276 t/m
Steel density	8.298 t/m^3
Nominal diameter of the chain	0.078
Axial stiffness EA	8.4222e+05
Volume-equivalent diameter	0.1404
Volume-equivalent cross-sectional area	0.0155
Added mass coefficient C_a	0.5556
Transverse drag coefficient	0.2034
Longitudinal drag coefficient	1.2394

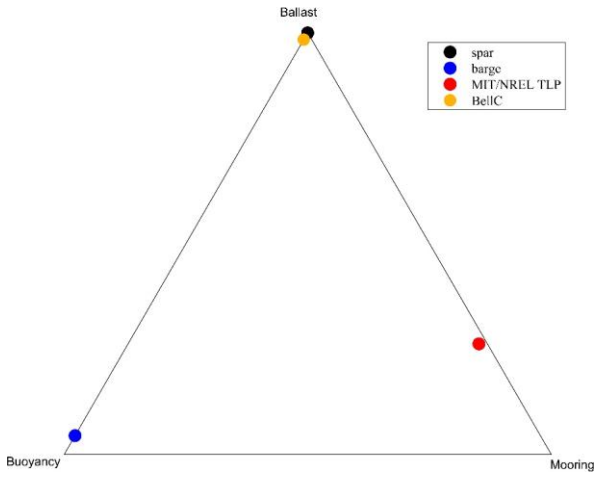

Figure 6.5: The position of the innovative platform in the stability triangle along with other existing platforms.

CHAPTER 7

PLATFORMS COMPARISONS

To test the performance of the innovative design, a comparative analysis between the OC3-Hywind spar-buoy, OC5 DeepCwind semi-submersible, and the proposed Bell/BellC platforms all supporting the same NREL 5-MW baseline wind turbine is conducted. Ballast is assumed to be compartmentalized for all platforms. Environmental properties (e.g., water density $\rho_f = 1.025\ t/m^3$, water depth $h = 200$, etc.), are set equal. The three platforms are manifested side by side in Figure 7.1.

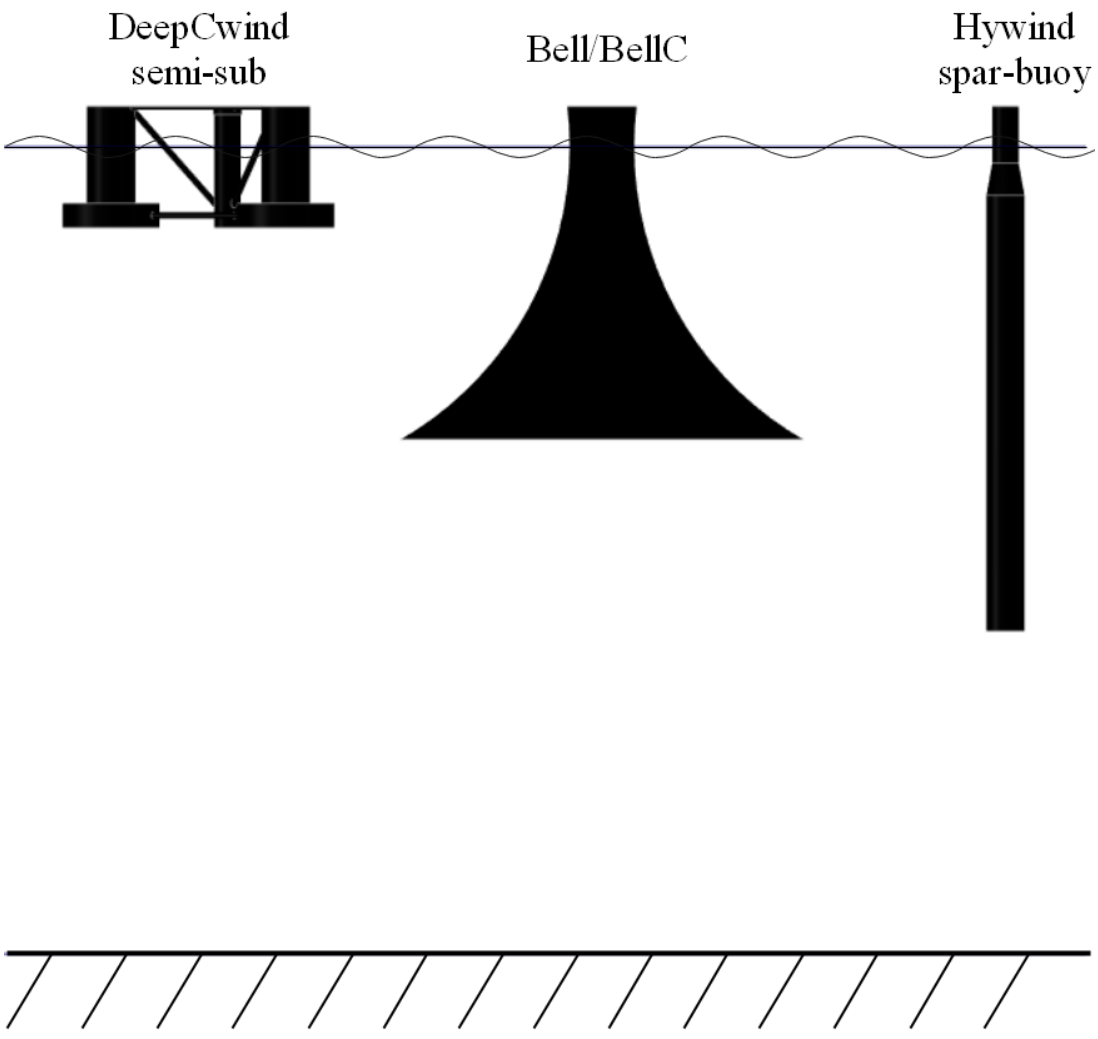

Figure 7.1: Configuration of platforms to be contrasted.

7.1. Dimensional and Hydrostatic Comparisons

As clearly observed from Figure 7.1 and emphasized in Figure 7.2. The proposed design has almost half the draft of the spar and slightly higher width radius than the semi-sub.

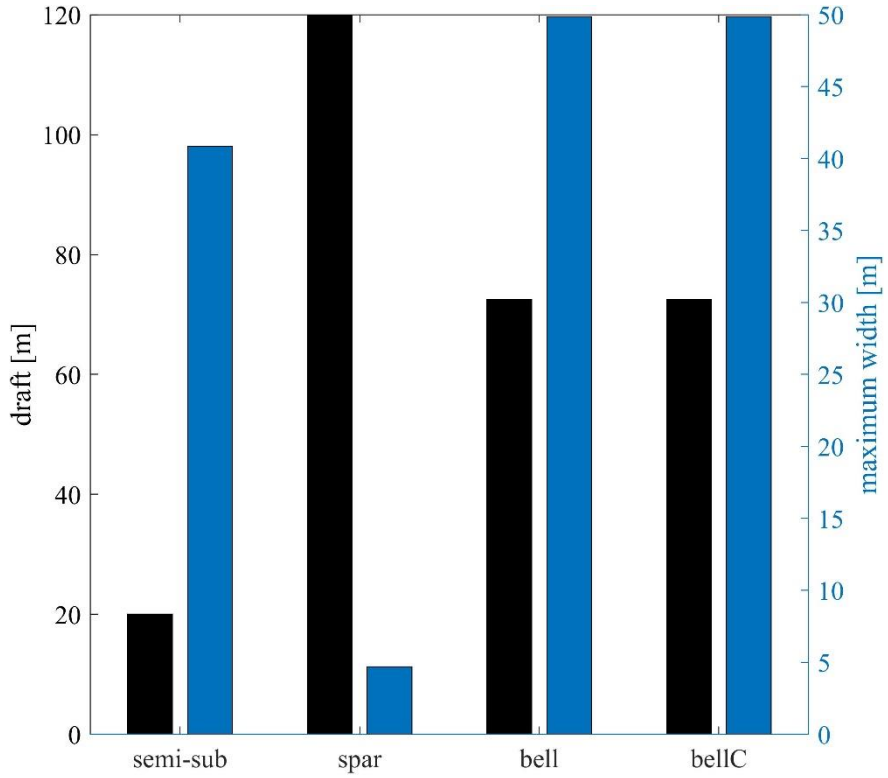

Figure 7.2: Geometric platform comparison. The left y-axis represents draft, and right y-axis is the width.

Masses and inertia are compared in Figure 7.3 and Figure 7.4. The high dependence on ballast in the proposed design is conspicuous when comparing the ballast masses. Steel mass in Bell is equivalent to that of the semi-submersible design, as this is one of the constraints described in Chapter 6. The concrete design, however, has a higher mass emerging from its thicker walls. But, the price comparison in Figure 7.5 probes that the concrete version is much cheaper than other steel alternatives. The enormous volume of ballast makes the inertia of the novel design large, which reflects positively on the wave resistance capability of the floating platform. Inertia along the z-axis is analogous to the one in spar design.

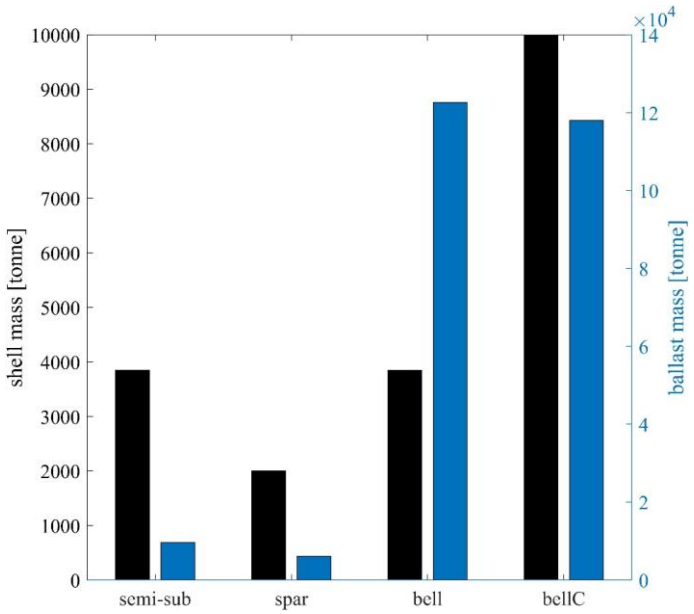

Figure 7.3: Shell and ballast mass of the platforms compared (left y-axis is shell mass; right y-axis is ballast mass).

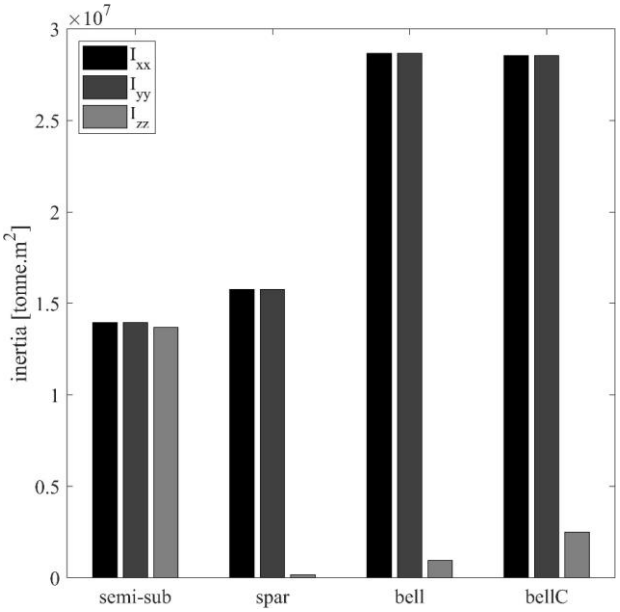

Figure 7.4: Inertias of the platforms compared.

Hydrostatic comparison is conducted. The significant volumetric displacement of Bell/BellC, as seen in Figure 7.6, leads to high buoyant force (Figure 7.7) and restoring moments in roll and pitch (Figure 7.8). When comparing water-plane areas in Figure 7.9, it is clear that Bell/BellC has an intermediate value between the spar and the semi-sub.

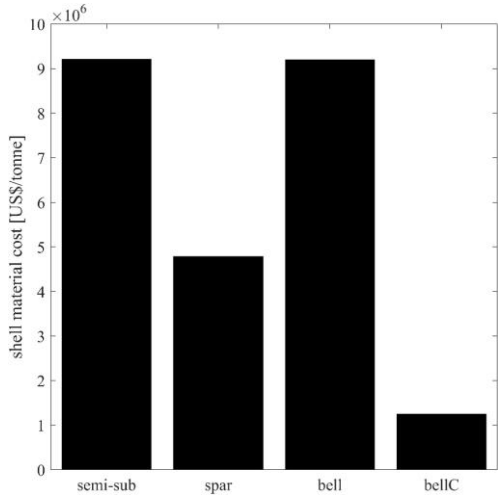

Figure 7.5: Comparison of shell cost.

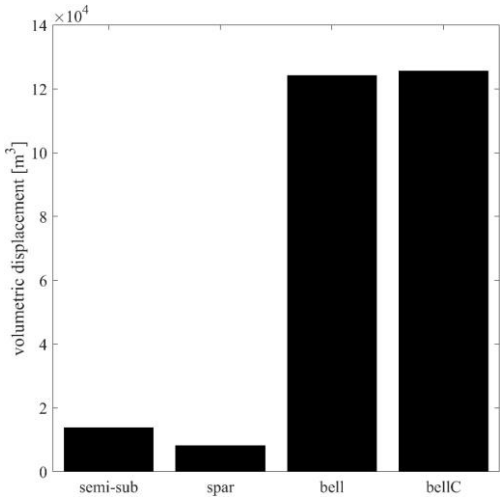

Figure 7.6: Comparison of the displaced volume of water among the platforms.

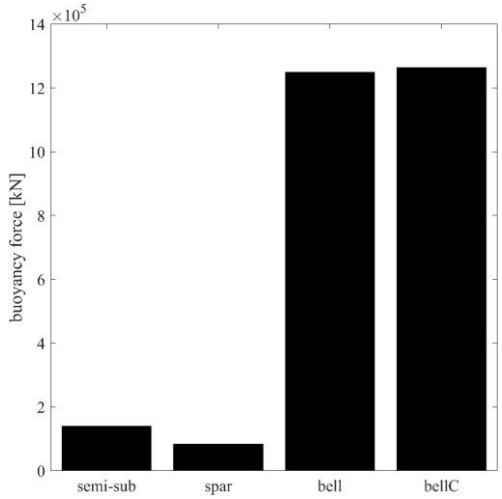

Figure 7.7: Buoyant force on the platforms compared.

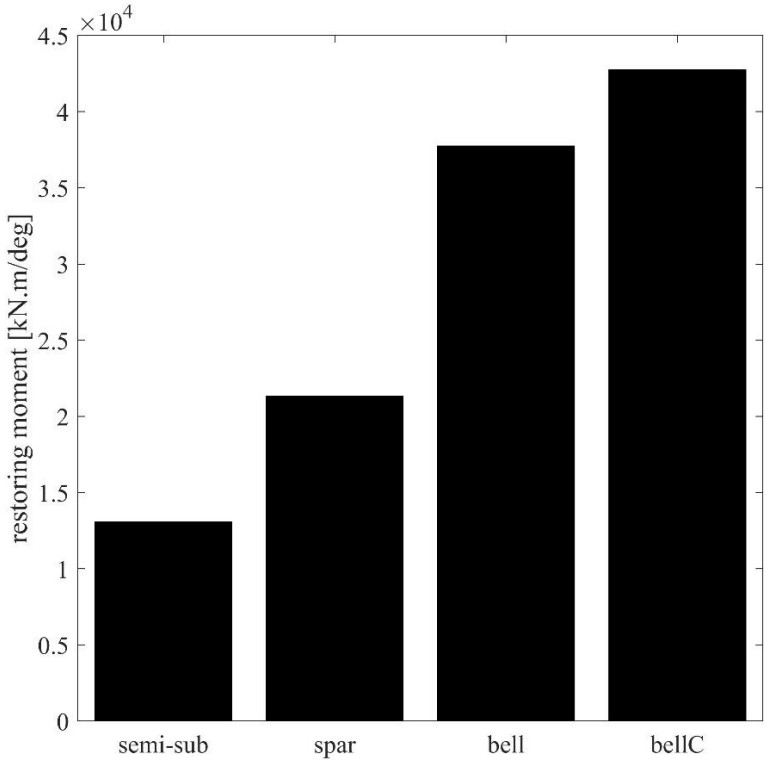

Figure 7.8: Restoring moments of the platforms compared.

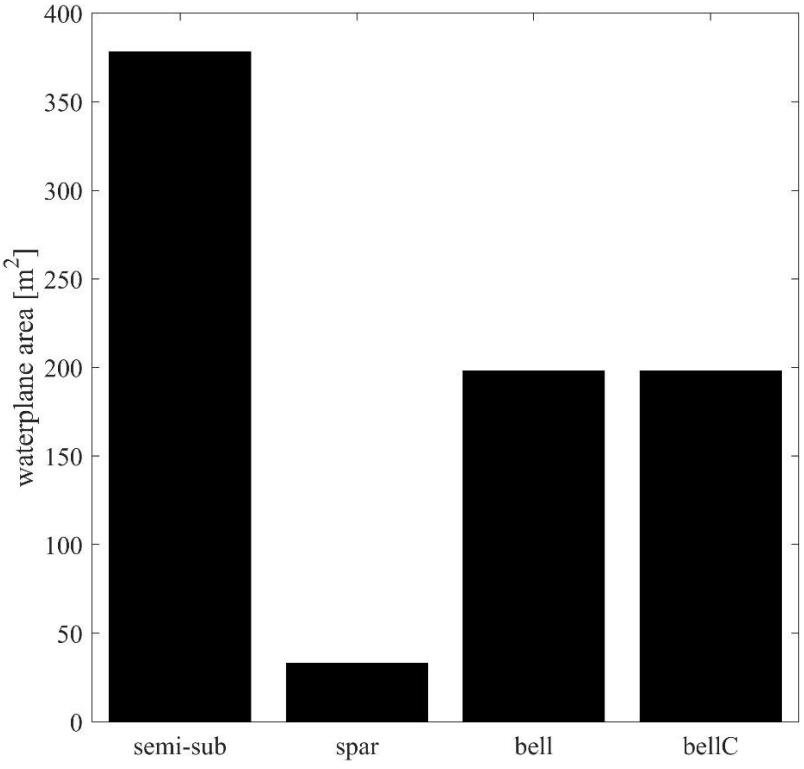

Figure 7.9: Water-plane area between the platforms.

7.2. Hydrodynamic Diffraction Comparison

Froude-Krylov forces and diffraction forces as a function of wave period in the three DoF excited by 0° incident wave are individually specified in Figure 7.10 and Figure 7.11. Forces generally prevail over the proposed designs due to their higher volume.

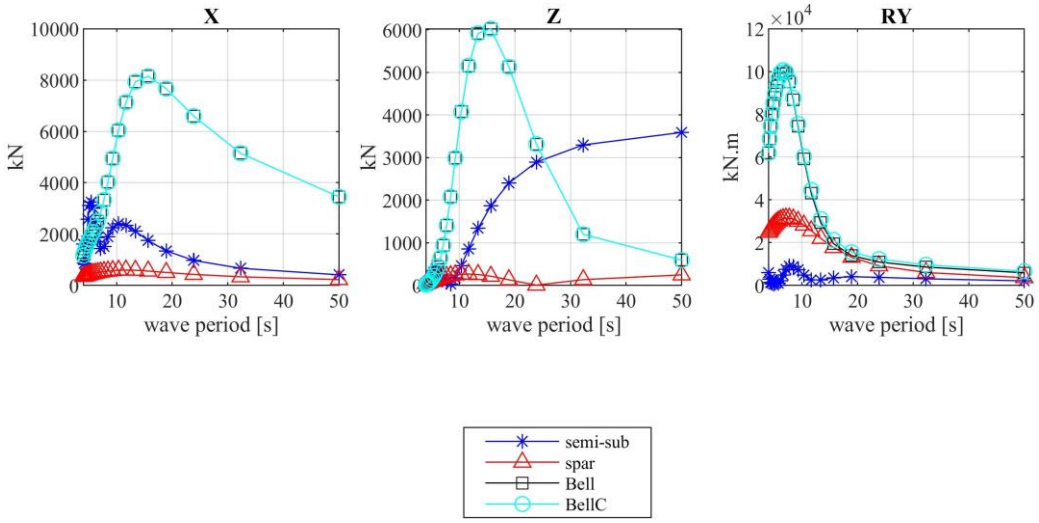

Figure 7.10: Froude-Krylov forces as a function of wave period for the studied platforms under the investigated DoF.

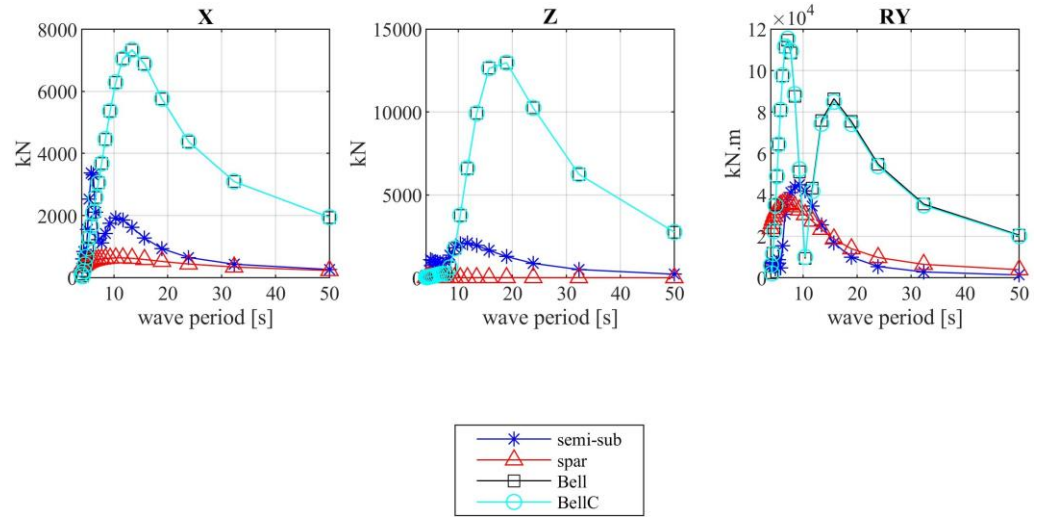

Figure 7.11: Diffraction forces as a function of wave period for the studied platforms under the investigated DoF.

One advantage of Bell RAO responses in heave and pitch is seen at low to moderate wave periods. But when the wave period increases, pitch relatively dissipates at the expanse of slightly more heave oscillations. Reducing pitch motion at extreme conditions limits the

fatigue forces on the wind turbine, prolonging the structural life-span (Si et al., 2014). Heave high amplitudes, while affect power generation efficiency, they entail lower fatigue on the system. Not to mention that pitch RAO is greatly enhanced while heave is only slightly deteriorated at overly longer periods. For the sake of completion, RAO phases are also included in Figure 7.13.

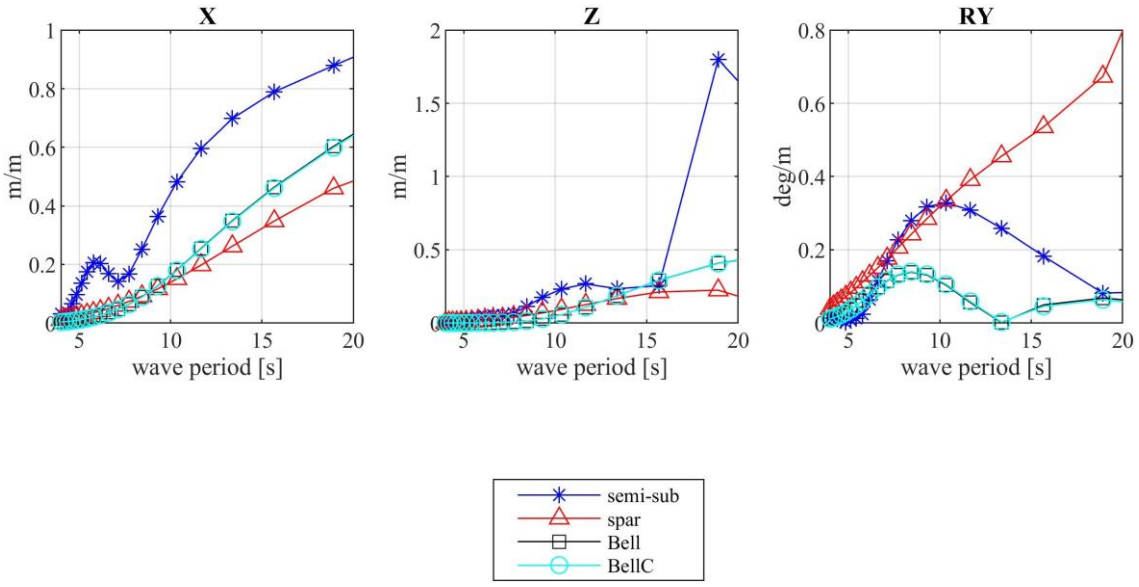

Figure 7.12: RAO amplitudes comparison as a function of wave periods for the studied platforms under the investigated DoF.

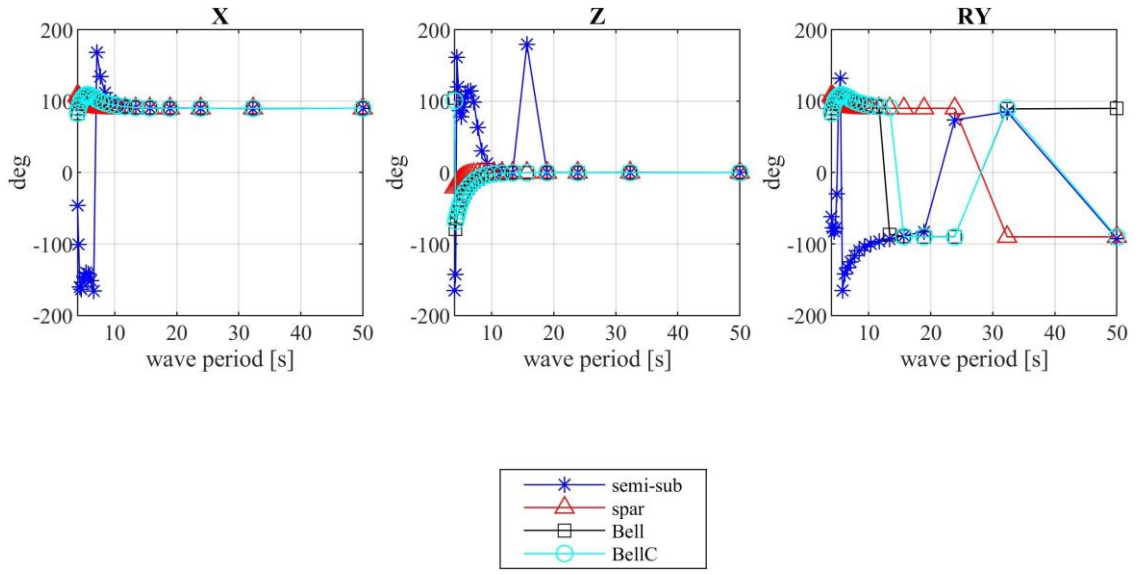

Figure 7.13: RAO phase comparison as a function of wave periods for the studied platforms under the investigated DoF.

Bell designs manifest higher radiation damping and added mass coefficients in the excited DoF due to their enormous size (Figure 7.14 and Figure 7.15). Sum and difference QTF matrices for all platforms are illustrated in Figure 7.16 and Figure 7.17, respectively. In general, it is fair to say that Bell and BellC have similar hydrodynamic diffraction outputs.

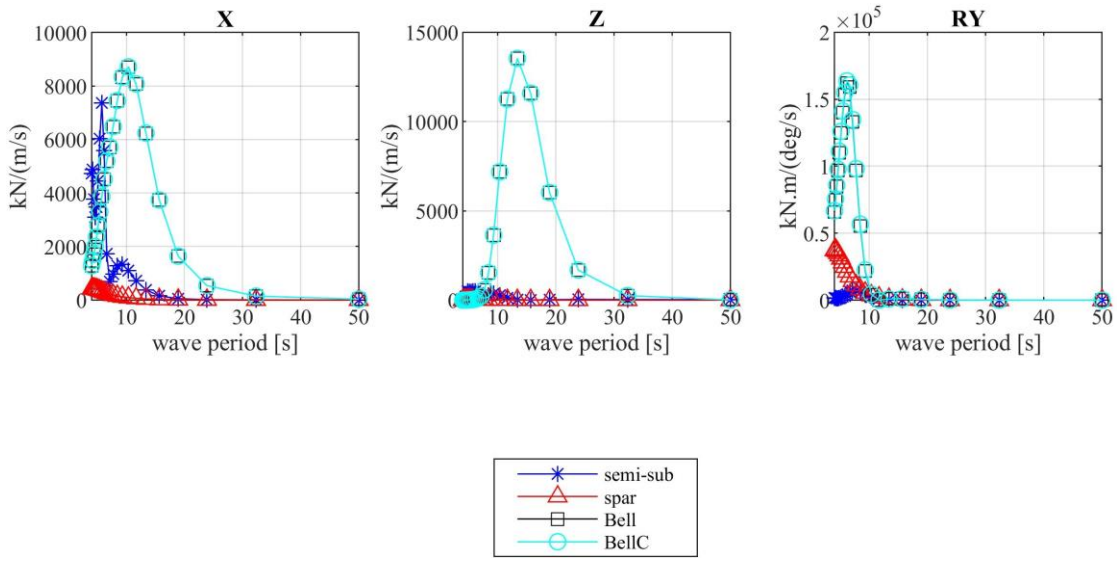

Figure 7.14: Radiation damping coefficient as a function of wave periods for the studied platforms under the investigated DoF.

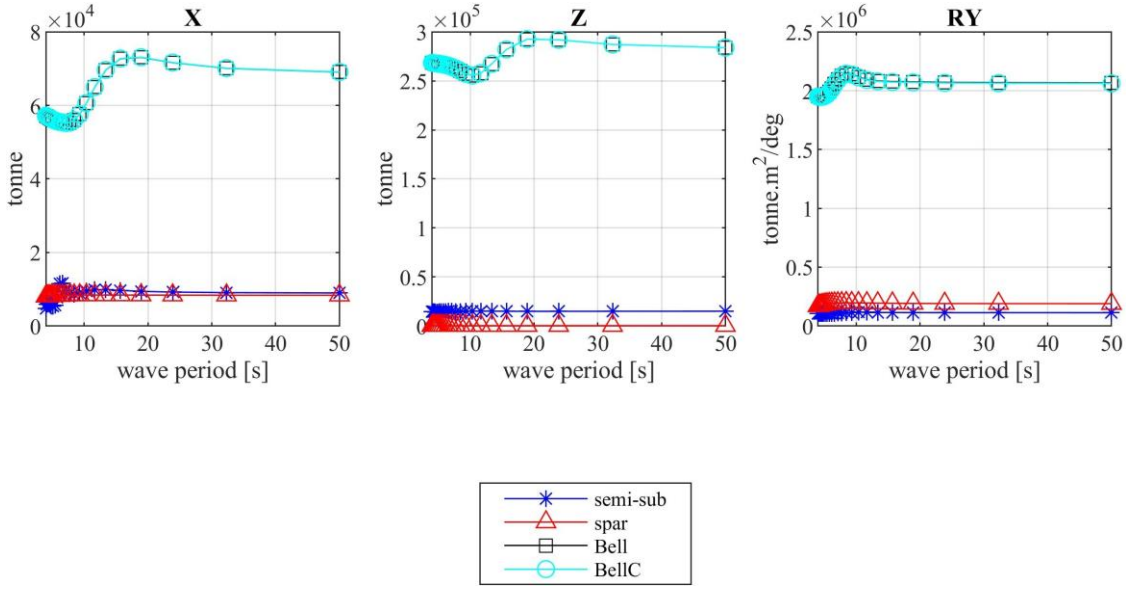

Figure 7.15: Added mass coefficient as a function of wave periods for the studied platforms under the investigated DoF.

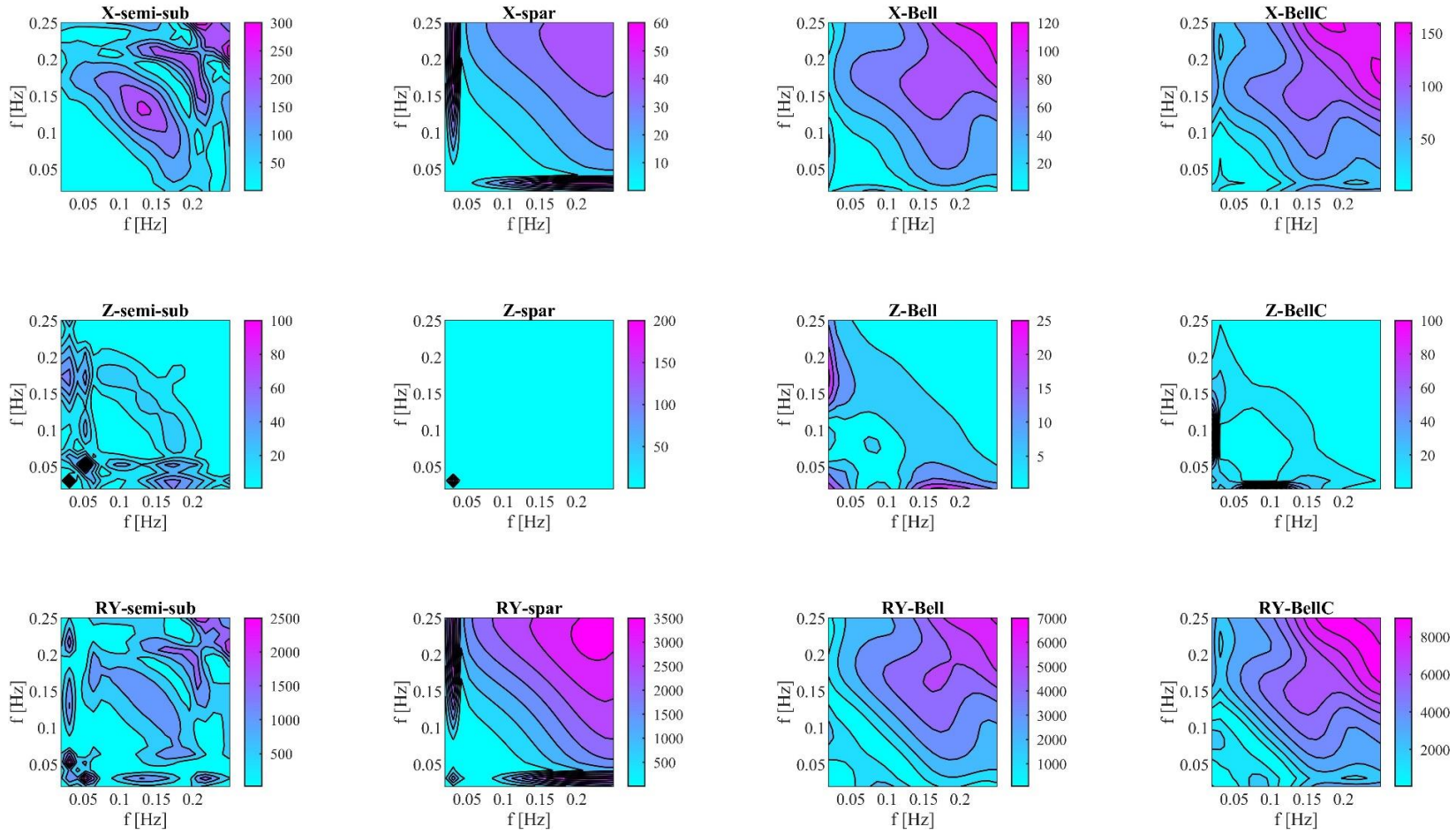

Figure 7.16: Sum QTF matrices for the studied platforms under the investigated DoF $[kN/m^2]$ for translational and $[kN \cdot m/m^2]$ for rotational mode.

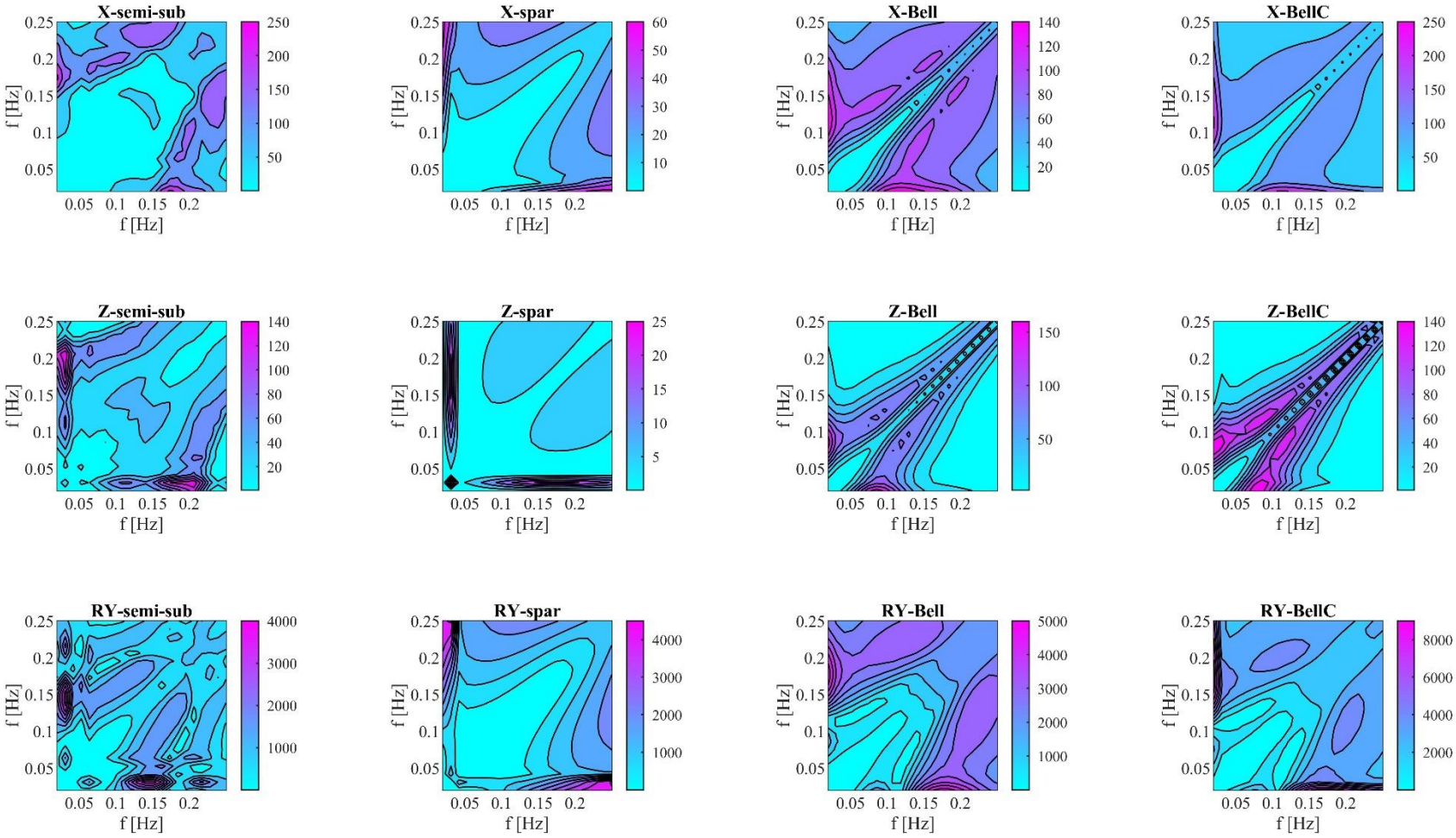

Figure 7.17: Difference QTF matrices for the studied platforms under the investigated DoF $[kN/m^2]$ for translational and $[kN \cdot m/m^2]$ for rotational mode.

7.3. Hydrodynamic Responses

In addition to the hydrodynamic forces, this section includes mooring system-induced effects and external aerodynamic forces. The cable section properties of the mooring cable are identical amongst all the platforms and are previously given in Table 6.4. Due to the platforms' different geometries, fairlead positions are not identical. The linearized mooring-induced horizontal stiffness is set alike to grant an apple-to-apple comparison. Figure 7.18 confirms the alikeness of the mooring behavior despite some deviation at extreme offsets. Table 7.1 contrasts the final mooring configuration choice.

Table 7.1: Mooring configurations for the compared platforms.

	Semi-sub	Spar	Bell/BellC
Horizontal mooring stiffness k_{xx} [kN/m]	82.8	82.8	82.8
Number of mooring lines N_c	3	3	3
Angle between the mooring lines θ_c	120˚	120˚	120˚
Radius to fairleads from tower centerline [m]	40.9	5.2	49.9
Depth to fairleads form SWL [m]	14.0	70.0	72.5
Radius to anchor from tower centerline [m]	837.6	853.9	840.0
Cable unstretched length L_c [m]	833.6	874.1	815.4
Cable Pretension T_0 [kN]	1229.5	877.6	847.1

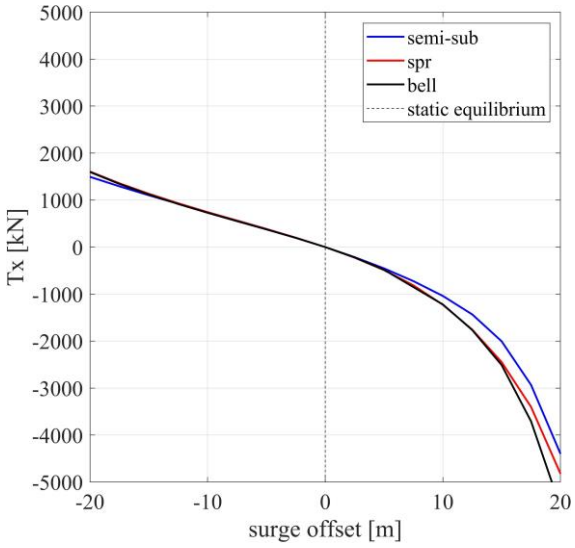

Figure 7.18: Sum of the horizontal mooring forces as a function of static surge offset.

7.3.1. Static Comparison

All platforms are statically in equilibrium. Upon the application of wind heeling, platforms have their static responses shown in Figure 7.19. The horizontal excursion is approximately the same since the mooring produces the same restoring forces. That said, pitch heeling moment is drastically lower for the Bell designs, especially BellC. Usually, this comes at the sacrifice of low natural periods in pitch. But for the Bell designs, their pitch natural periods are even higher than both platforms, as demonstrated in Figure 7.20, rendering its performance statically and dynamically more advantageous.

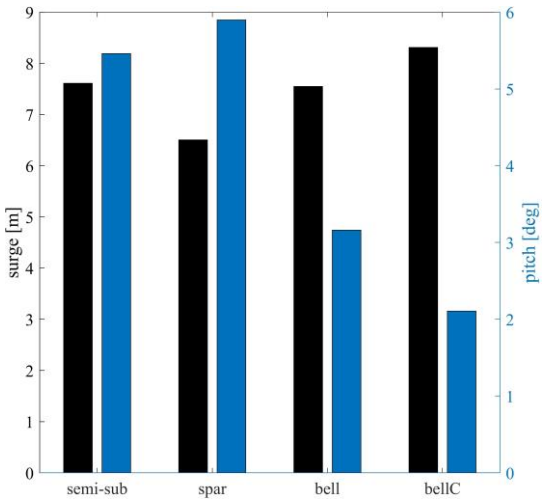

Figure 7.19: Platform responses to wind heeling moment (left y-axis is surge; right y-axis is pitch angle).

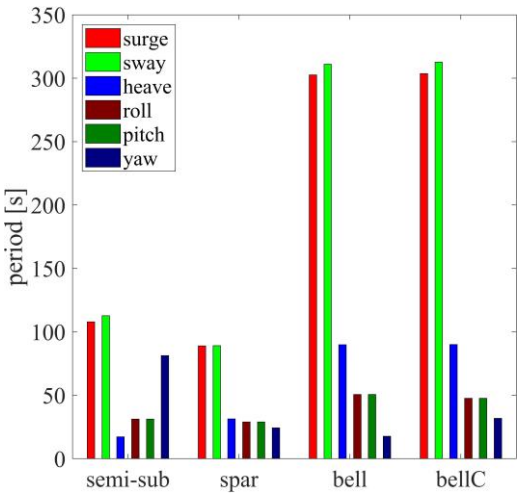

Figure 7.20: Natural modes comparison.

7.3.2. Wave-only Comparisons

From here on, Bell replaces Bell/BellC since their hydrodynamic responses are observed to be identical. Load cases LC3.1 through LC3.4 described in Table 4.8, corresponding to a moderate and extreme regular/irregular wave loading, are tested to compare the performance of the designated platforms. Results are provided as RAO in Figure 7.21 and Figure 7.22. As explained previously, the Bell system translates extreme energy wave into heave motion for better safety, delivering the highest amplitude in heave but the lowest in pitch in Figure 7.22. Surge resides slightly higher than spar amplitude but majorly lower than the semi-submersible. Tension in the BOW cable of Bell fluctuates the least for the moderate wave, but spar BOW outperforms under extreme excitation. Bell leeward cables perform better in all cases due to low pretension value.

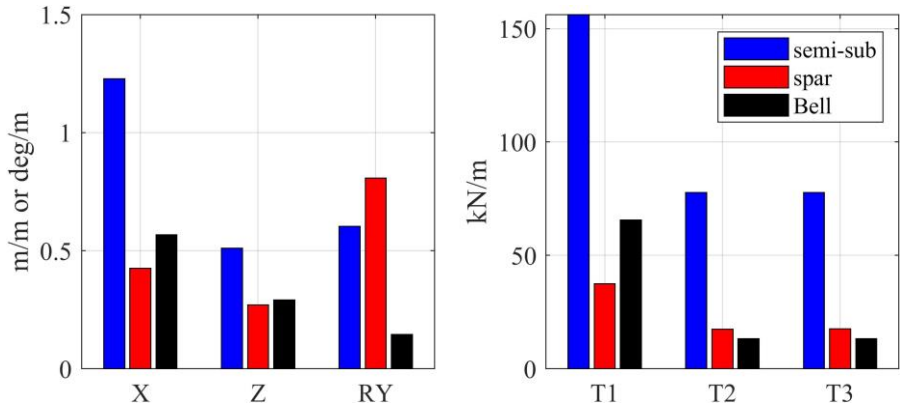

Figure 7.21: RAO results under moderate regular wave excitation LC3.1.

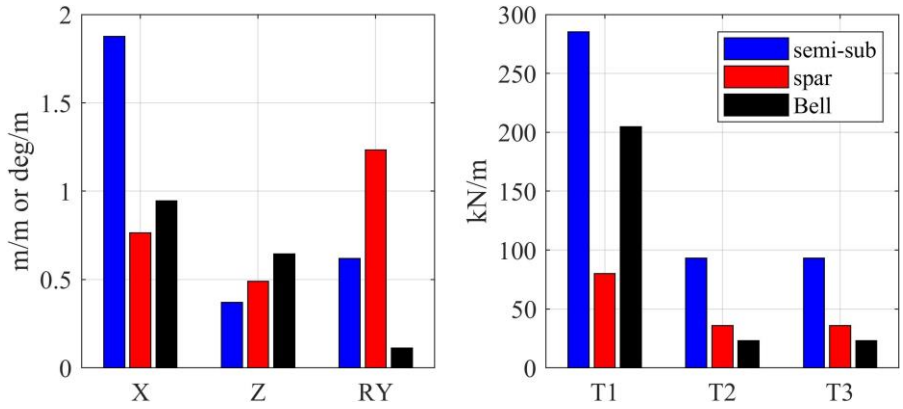

Figure 7.22: RAO results under moderate regular extreme excitation LC3.2.

Spectral responses emerging from irregular wave loading are portrayed in Figure 7.23 for the moderate case and Figure 7.24 for the extreme one. For better visualization, the LF and WF responses are differentiated, and their amplitudes are quantified in Figure 7.25 and Figure 7.26. These figures reveal improvements in the WF performance of the Bell design. The LF responses are worse than the spar but better than the semi-submersible platform. It is normal to see higher amplitudes in the extreme condition (left side of Figure 7.25 and Figure 7.26). The notable LF surge amplitude of Bell produces high LF oscillations in tension forces. However, WF tension bars are astonishingly narrow. Figure 7.27 explicitly exposes the low-pass filtered response for the motion responses in the extreme wave. As can be seen, heave oscillations are higher than other platforms' motions. These slowly varying heave oscillations have a minimal effect on the vertical acceleration of the hub (Figure 7.28). Horizontal acceleration is more dominant in all platforms, which is mostly the product of surge motions.

The low pretension values of the mooring cables suggest that there is a room of stiffening the mooring lines to limit LF surge responses. For instance, if the pretension value is doubled (from 847 kN to 1694 kN), surge LF amplitude gets reduced by 34% at the expanse of increasing LF tension amplitude, and more than doubling the WF amplitude for all cables (check Figure 7.29 & Figure 7.30).

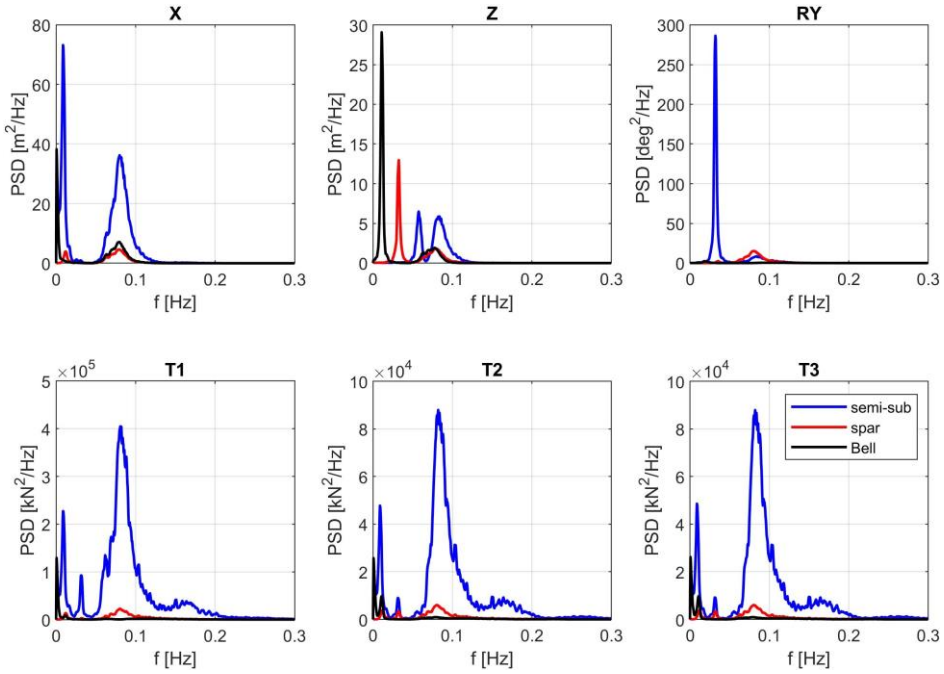

Figure 7.23: Spectral density of platforms responses under moderate, irregular wave excitation LC3.3.

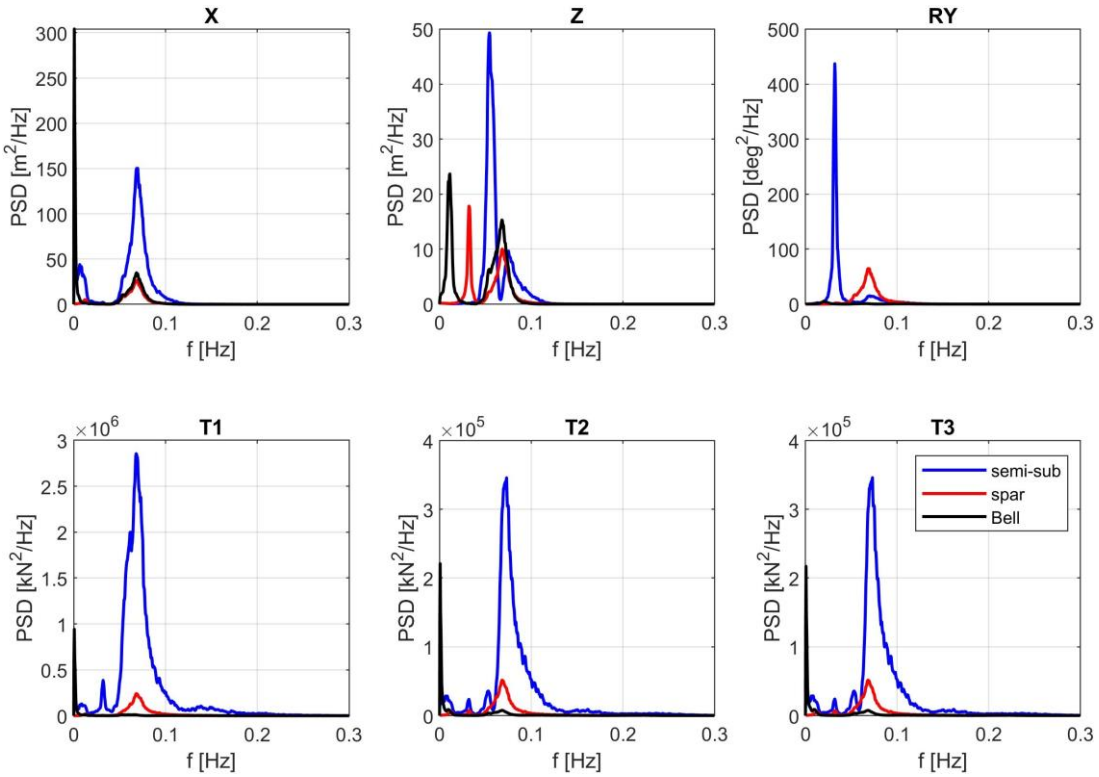

Figure 7.24: Spectral density of platforms responses under extreme, irregular wave excitation LC3.4.

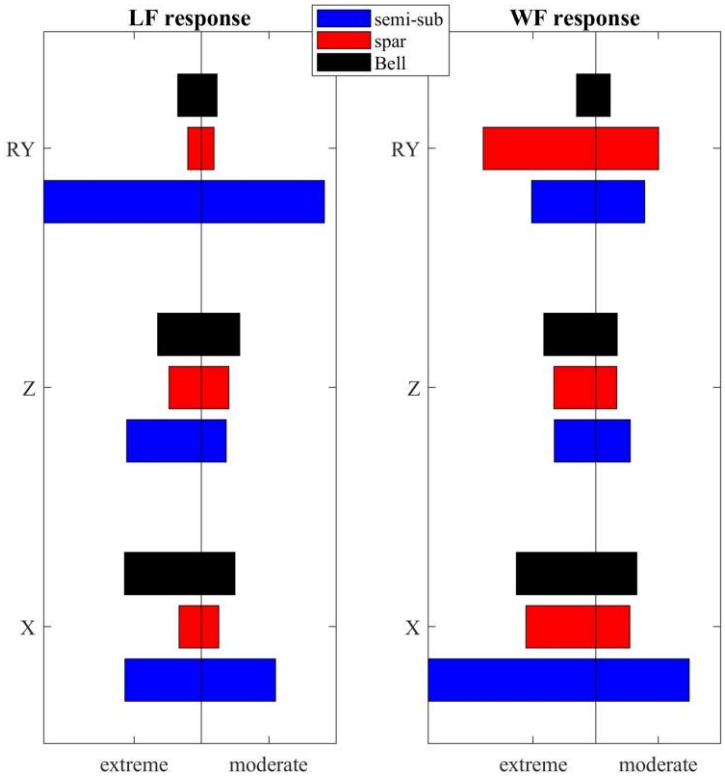

Figure 7.25: Moderate and extreme LF & WF motion response comparison.

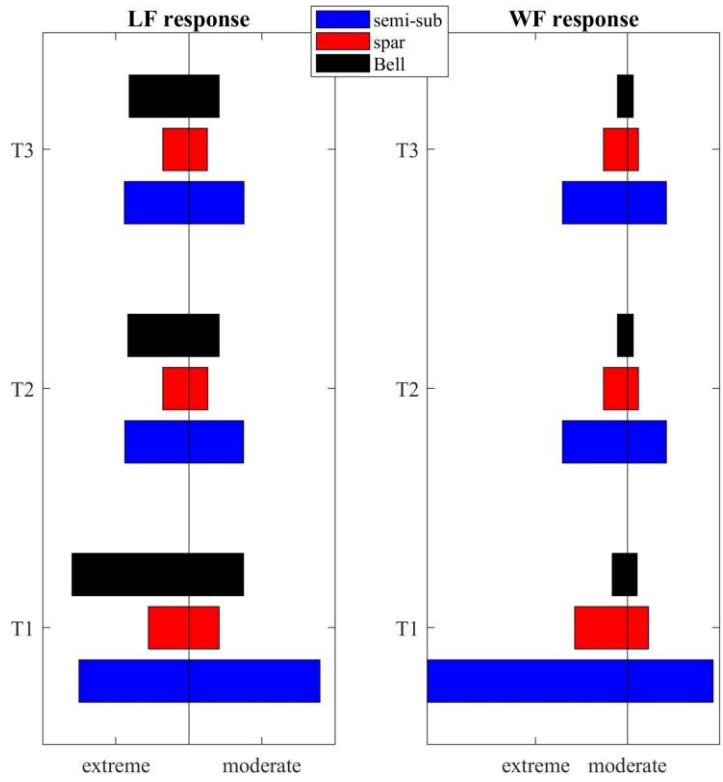

Figure 7.26: Moderate and extreme LF & WF tension response comparison.

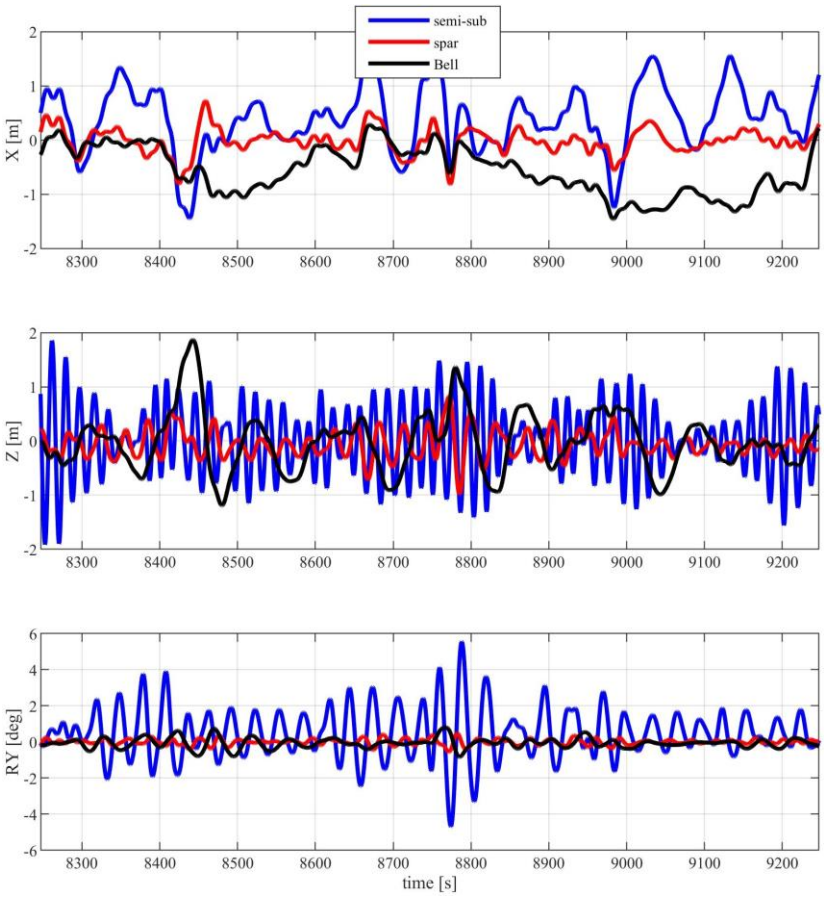

Figure 7.27: LF response at the extreme case in time-domain.

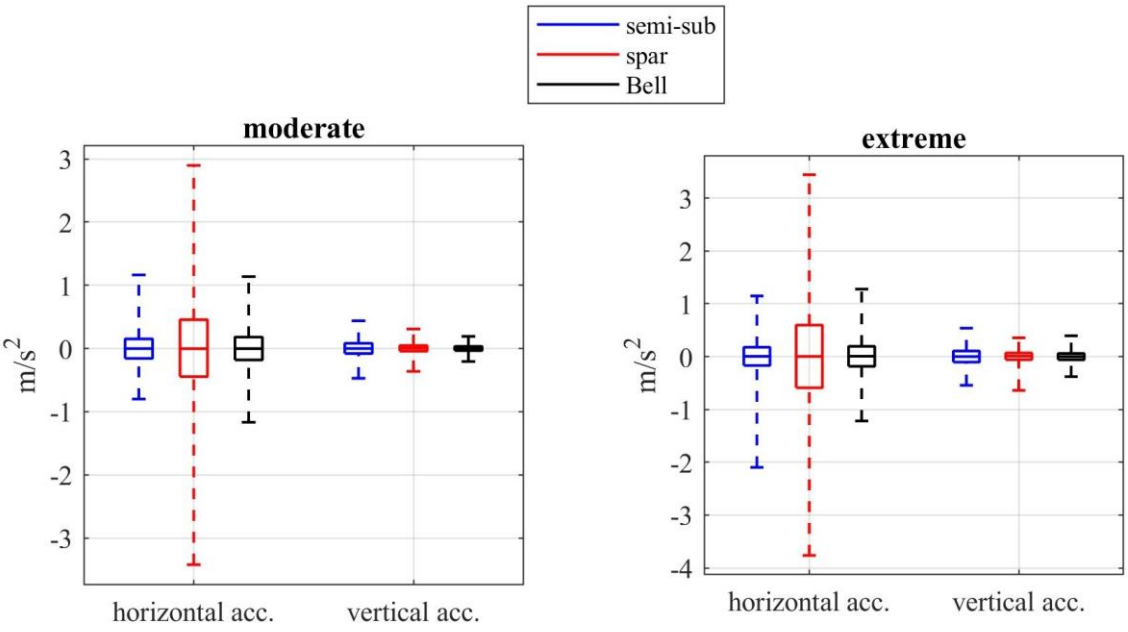

Figure 7.28: Hub acceleration components in moderate and extreme wave conditions.

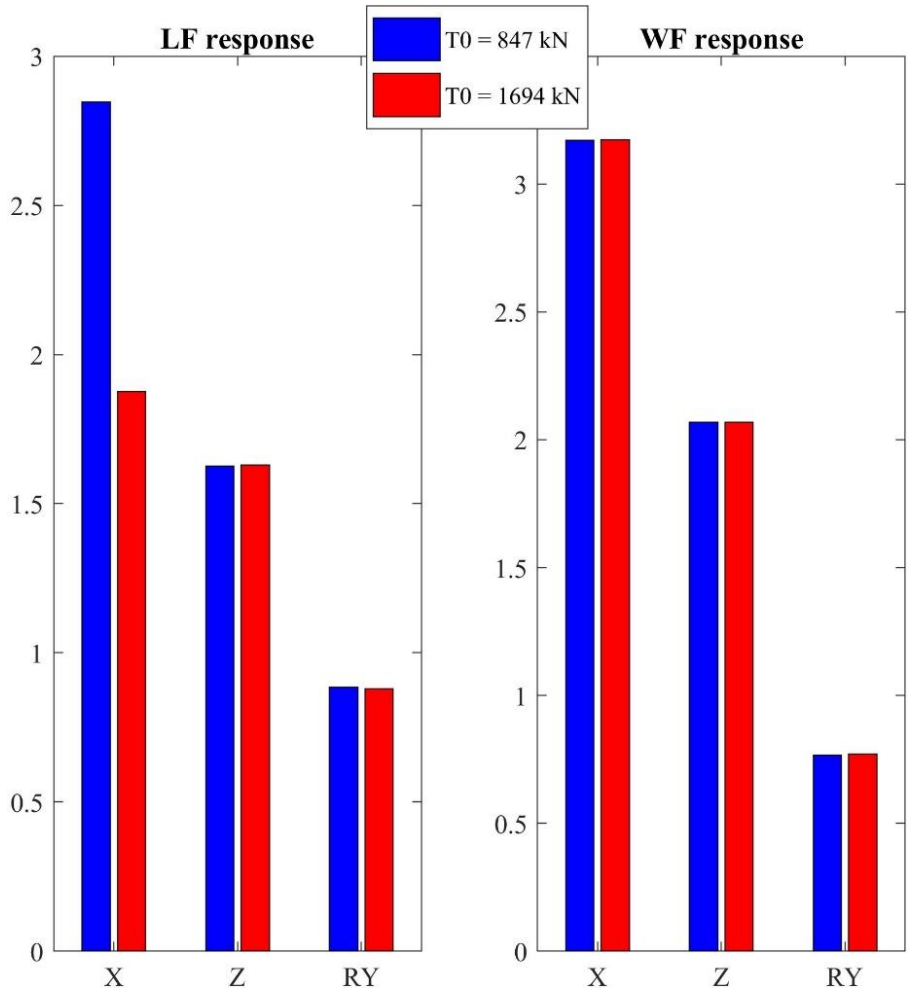

Figure 7.29: Effect of doubling the pretension value of BellC on motion responses.

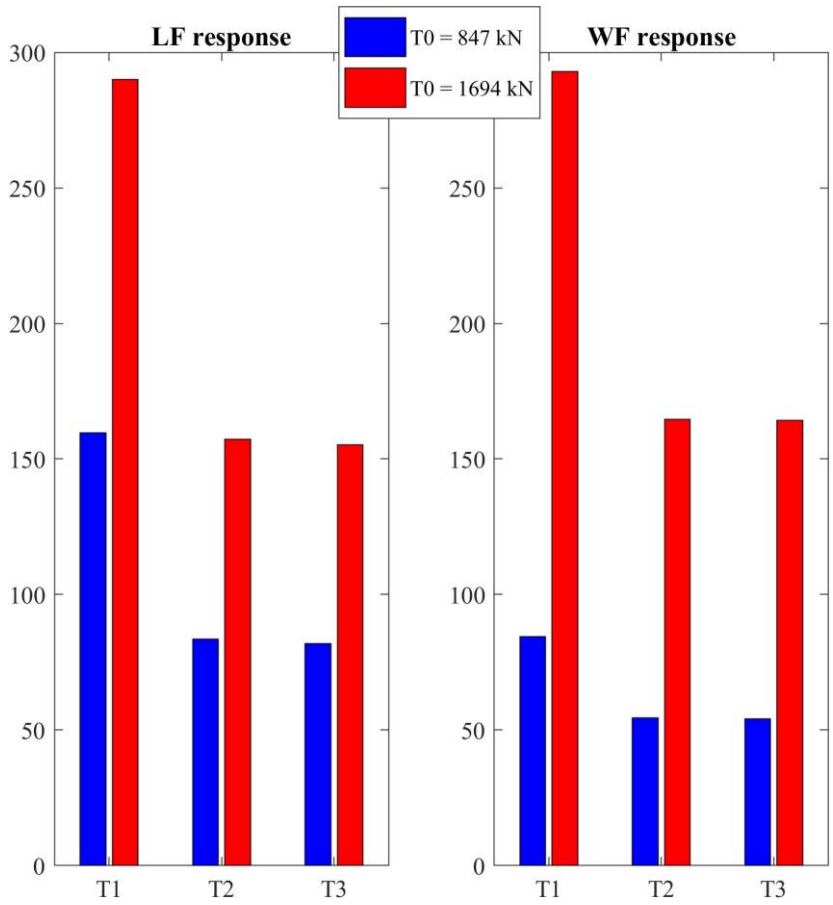

Figure 7.30: Effect of doubling the pretension value of BellC on tension responses.

7.3.3. Wave/Wind Comparisons

The response under both stochastic wind and wave excitations are eventually scrutinized. The load case is LC4.3, described in Table 4.8. The outcomes are statistically summarized in Figure 7.31. The mean responses of surge and pitch coincide with the results of Figure 7.19. Surge range in Bell is better than semi-sub, and the pitch range is better than both. Due to the cables' low pretension values required to reach the same horizontal stiffness in Bell design, its static and dynamic cable tensions outperform the rest. Aerodynamic coefficients are nevertheless similar in all platforms. There is a minuscule advantage for Bell in terms of maximum thrust force exerted on the system and mean power coefficient. Simultaneous maximum action of wind and wave generally do not occur in nature, because wind ought to be too fast (above the rated wind speed – thrust forces are not maximum) to generate extreme waves. For the sake of trial, imagine an extreme scenario of dual dominance from wind and wave. Subsequently, the system response to wind from

load case LC4.3 combined with the wave loading from load case LC3.4 is investigated. Mean drift viscous force is also applied for all platforms, according to Eq. (4.4). The resulting force is the highest for a semi-submersible (258 kN) due to its large cylinders at the water surface, then comes the force exerted on the Bell (97 kN), then on the spar (40 kN). Platforms react similarly to LC4.3 (Figure 7.32). However, surge severe excursions render the upwind cables extremely taut. The zero-upcrossed tension ranges are compared with their periods. The Bell records the highest periods and lowest amplitudes. Snap events do not develop under the tested duration for the spar and Bell design, but they do in semi-sub, as Figure 7.33 demonstrates.

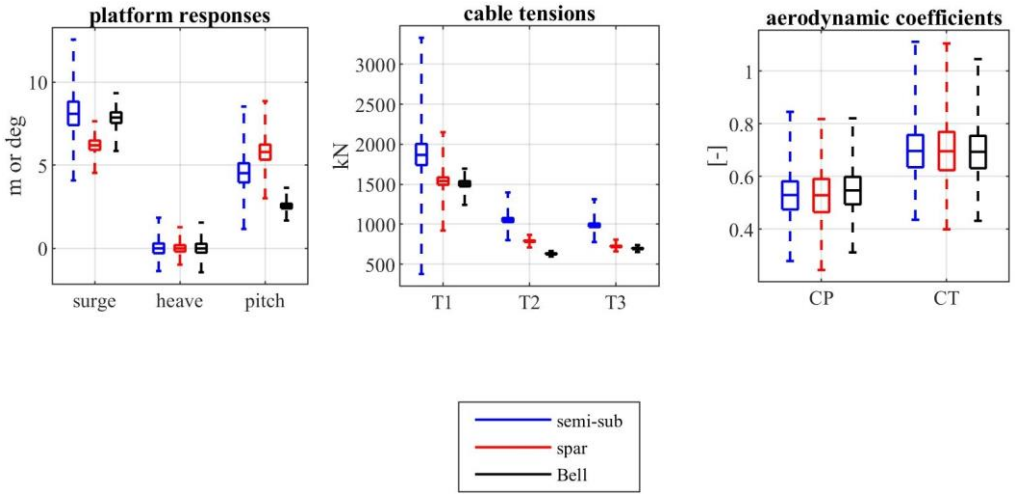

Figure 7.31: Whisper box, comparing responses, tensions, and aerodynamic coefficients for the designated platforms.

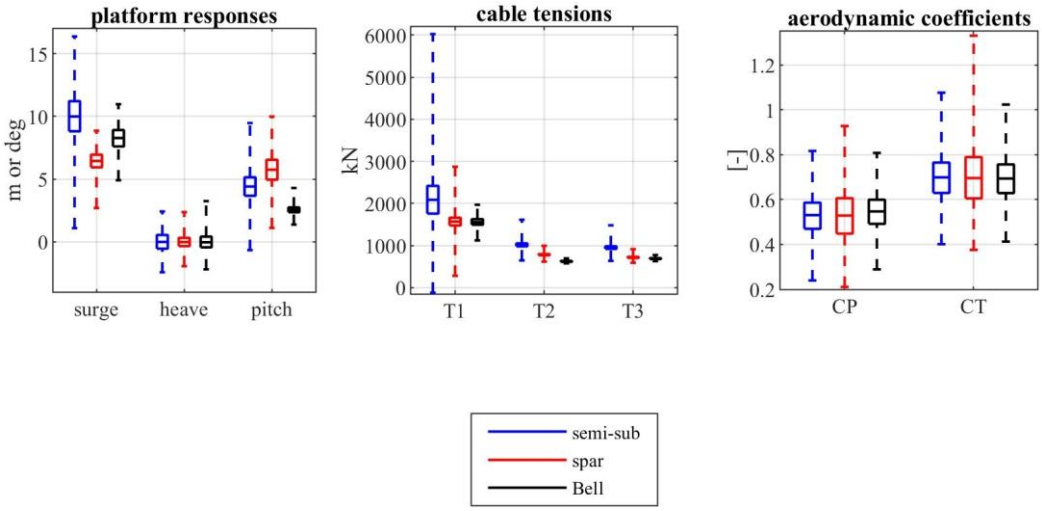

Figure 7.32: Platforms responses to simultaneous wind and wave extremities.

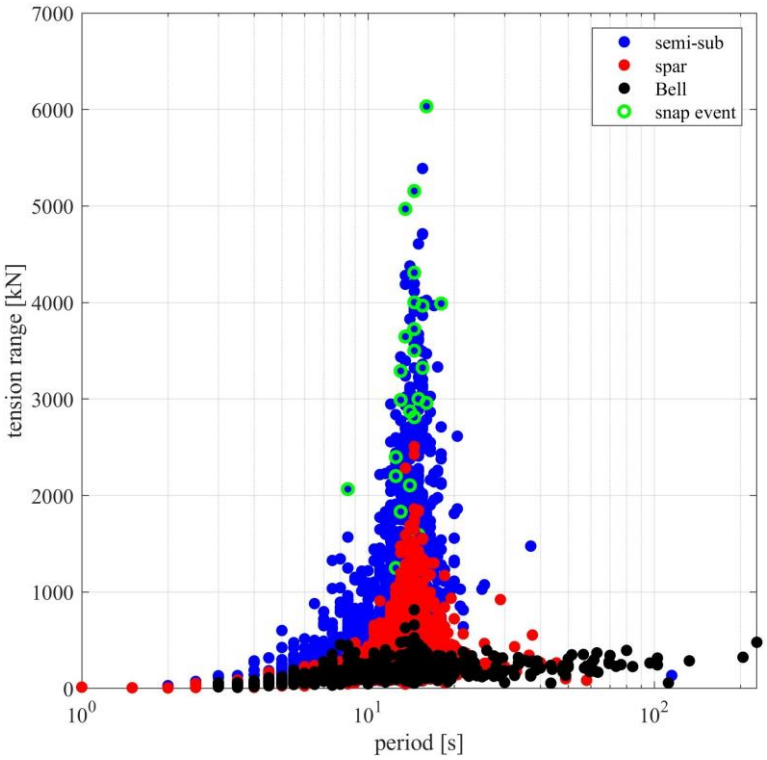

Figure 7.33: Tension ranges as a function of oscillatory periods and snap event occurrence.

CHAPTER 8

CONCLUSIONS

A numerical model consisting of aerodynamics, hydrodynamics, and mooring dynamics is developed. The response of the DeepCwind semisubmersible platform supporting the 5-MW baseline wind turbine to excitations of wind and wave is investigated under various settings. It is concluded that the inclusion of wave kinematics and the application of viscous-induced mean drift force in the direction of the wave helps to capture slowly-varying motions in the horizontal excursion and on the wave-frequency oscillations of the mooring tension. The capability of a numerical model to capture nonlinearities in the system determines how accurate its estimations are. When conducting error assessment among the codes developed by the various international institutes participated to OC5 code comparison project. It becomes evident that discrepancies with the test model shrink when the second-order potential theory is adopted, and when the dynamics of the mooring cables are included. Contrasting their codes with the present model reveals the outperformance of the second proposed calibration method. The average participant's error is around 50% for the low-frequency of surge, pitch, and tension responses whilst the current model errs by around 7%.

Simplified environmental assumptions, while crucial in the design stage of a FOWT system, it does not manifest reality as it is for operational conditions. The same platform is examined under the influence of wave irregularity in terms of the frequency spectrum shape and the directional spreading. As spectral shape becomes narrower, excitations increases in wave frequency region. However, low-frequency motion behaves in an opposite pattern than the wave-frequency motions. It is also shown that the wave groping is pronounced as spectrum becomes narrower. Therefore, the presence of consecutive high-amplitude waves has a cumulative influence on the responses, and thus, on the tensions as the most loaded cable snaps more frequently. Stochastic waves have their energy distributed for a wide range of frequencies and directions. A thorough examination of the platform's response patterns to a uni-directional vs. a multidirectional wave indicates that the conservatism of uni-directional assumption is not always correct as multidirectional-induced motions at particular angles and modes can surpass the uni-

directional behavior. Therefore, it is critical to examine such types of loading, especially if the platform is asymmetric.

Moreover, a parametric optimization for a truncated spar-buoy design operating in moderate water depth is scrutinized. Due to depth restrictions, mooring cables must be delicately designed to circumvent any unwanted peak tensions. Additionally, an original truncated mooring configuration is devised for the platform to be tested in a narrow wave flume without sacrificing much in mooring properties and mooring effects on the platform motion.

The essential role played in this study is to comprehend the fundamentals of creating a novel platform designed exclusively for FOWT systems. For this, shell geometric optimization is investigated, aiming to enhance the platform resistance to external excitations employing passive techniques. During the optimization process, it is revealed that a trade-off is inevitable. However, a well-engineered design must not be confined to local enhancements or improvements in one part that might cause deterioration in vital functionalities. Based on this, the proposed model is a product of simultaneous enrichment of static and dynamic characteristics while keeping material costs low. The result is the Bell design with high ballast-induced inertia. It has the following advantages:

1- Low-cost shell material

2- 60% reduction in rotation under wind heeling moment. (static optimization)

3- Improved low-frequency & wave-frequency pitch motion, especially at extreme conditions. (dynamic optimization)

4- Shorter required cables to reach the same horizontal stiffness

5- Lower fatigue on the mooring cables

Side effects of the design are:

1- An increase in the manufacturing costs due to the peculiar geometry the design has.

2- A slight increase in the low-frequency heave responses.

The static and dynamic comparison conducted provides supporting shreds of evidence in favor of the Bell/BellC design. The enhanced wave resistance of the design

prompts lower fatigue to the system, prolonging the system's life-span, which might cover the additional initial cost. Due to the low pre-tension values of the mooring cable, increasing the cables stiffness to limit horizontal excursions even further is a possibility, but that will come at a sacrifice of tensioning the cables.

This thesis is ongoing research. Future work will include:

1- Dynamic calibration of wind through the use of tested wind-only load cases.

2- Impact of ballast water sloshing effects inside the Bell design.

3- Introduction of fin damper designs on the side of the shell

4- Optimization of multi-segmented mooring configuration

5- Parabolic and hyperbolic functions of Bell walls.

6- Experimental work on the spar-buoy design proposed in Chapter 5.

Due to its globally vast potential, offshore wind power is likely to expand splendidly over the coming decades as raising awareness of the fact that life on earth as we know it is in a critical conjuncture. Efforts to resist the ever-increasing ecological exacerbation must be our priority if not to reverse the situation, then at least to mitigate the damage from the inevitable impact.

REFERENCES

ANSYS Inc. 2013. “Aqwa Theory Manual,” 174.

Archer, Cristina L., and Mark Z. Jacobson. 2005. “Evaluation of Global Wind Power.” *Journal of Geophysical Research D: Atmospheres* 110 (12): 1–20. https://doi.org/10.1029/2004JD005462.

Barrera, Carlos, Iñigo J. Losada, Raúl Guanche, and Lars Johanning. 2019. “The Influence of Wave Parameter Definition over Floating Wind Platform Mooring Systems under Severe Sea States.” *Ocean Engineering* 172: 105–26. https://doi.org/10.1016/j.oceaneng.2018.11.018.

Benitz, Maija A., David P. Schmidt, Matthew A. Lackner, Gordon M. Stewart, Jason M. Jonkman, and Amy Robertson. 2015. “Validation of Hydrodynamic Load Models Using CFD for the OC4-DeepCwind Semisubmersible.” In *Volume 9: Ocean Renewable Energy*, V009T09A037. St. John’s, Newfoundland, Canada: ASME. https://doi.org/10.1115/OMAE2015-41045.

Branlard, Emmanuel. 2017. *Wind Turbine Aerodynamics and Vorticity-Based Methods*. *Research Topics in Wind Energy*. Vol. 7. https://doi.org/10.1007/978-3-319-55164-7_14.

Butterfield, Sandy, Walter Musial, Jason M. Jonkman, and Paul D. Sclavounos. 2005. “Engineering Challenges for Floating Offshore Wind Turbines.” *Journal of Applied Physics*, no. December 1989 (October): 13. http://ieeexplore.ieee.org/xpls/abs_all.jsp?arnumber=5041769%5Cnhttp://gisceu.net/pdf/u444.pdf.

Chakrabarti, Subrata. 1995. “Offshore Structure Modelling.” *Applied Ocean Research* 17 (6): 391–92. https://doi.org/10.1016/s0141-1187(96)00012-0.

Chen, Da, Peng Gao, Shanshan Huang, Ke Fan, Ning Zhuang, and Yingdi Liao. 2017. “Dynamic Response and Mooring Optimization of Spar-Type Substructure under Combined Action of Wind, Wave, and Current.” *Journal of Renewable and Sustainable Energy* 9 (6): 063307. https://doi.org/10.1063/1.5017228.

Coulling, Alexander, Andrew Goupee, Amy Robertson, and Jason M. Jonkman. 2013.

"IMPORTANCE OF SECOND-ORDER DIFFERENCE-FREQUENCY WAVE-DIFFRACTION FORCES IN THE VALIDATION OF A FAST SEMI-SUBMERSIBLE FLOATING WIND TURBINE MODEL," 1–10.

Ding, Qinwei, Chun Li, Binxin Li, Wenxing Hao, and Zhou Ye. 2017. "Research on the Influence of Helical Strakes and Its Parameters on Dynamic Response of Platform of Floating Wind Turbine Based on Optimization Method of Orthogonal Design." *Journal of Solar Energy Engineering* 139 (5): 051002. https://doi.org/10.1115/1.4037091.

DNV-GL. 2010. "Environmental Conditions and Environmental Testing." *INTELEC, International Telecommunications Energy Conference (Proceedings)* 2 (October): 92–99. https://doi.org/10.1109/INTLEC.1993.388591.

———. 2011. "Offshore Standard DNV-RP-H103 -Modelling And Analysis Of Marine Operations." *Det Norske Veritas*, no. April: 150.

———. 2015. "OFFSHORE STANDARD DNV GL AS Position Mooring," no. July: 114.

———. 2018. "DNVGL-ST-0119 Floating Wind Turbine Structures," no. July: 162.

Duarte, Tiago, Sébastien Gueydon, Jason M. Jonkman, and António Sarmento. 2014. "Computation of Wave Loads under Multidirectional Sea States for Floating Offshore Wind Turbines." *Proceedings of the International Conference on Offshore Mechanics and Arctic Engineering - OMAE* 9B (March). https://doi.org/10.1115/OMAE2014-24148.

Eckert-gallup, Aubrey C, Cédric J Sallaberry, Ann R Dallman, and Vincent S Neary. 2014. "Modified Inverse First Order Reliability Method (I-FORM) for Predicting Extreme Sea States." *Sandia National Laboratories Report*, no. September: 41.

Ghafari, Hamidreza, and Morteza Dardel. 2018. "Parametric Study of Catenary Mooring System on the Dynamic Response of the Semi-Submersible Platform." *Ocean Engineering* 153 (April): 319–32. https://doi.org/10.1016/j.oceaneng.2018.01.093.

Glauert, Hermann. 1935. "Airplane Propellers." In *Aerodynamic Theory*, 169–360. Springer.

Goda, Yoshimi. 2010. *Random Seas and Design of Maritime Structures*. Vol. 33. Singapore: World Scientific. https://doi.org/10.1142/7425.

Goupee, Andrew, and Richard Kimball. 2015. "A Calibrated Blade- Element / Momentum Theory Aerodynamic Model of the MARIN Stock Wind Turbine Preprint," no. April.

Gueydon, Sébastien, Tiago Duarte, and Jason M. Jonkman. 2014. "Comparison of Second-Order Loads on a Semisubmersible Floating Wind Turbine." *Proceedings of the International Conference on Offshore Mechanics and Arctic Engineering - OMAE* 9A (March). https://doi.org/10.1115/OMAE2014-23398.

Hall, Matthew, and Andrew Goupee. 2015. "Validation of a Lumped-Mass Mooring Line Model with DeepCwind Semisubmersible Model Test Data." *Ocean Engineering* 104 (June): 590–603. https://doi.org/10.1016/j.oceaneng.2015.05.035.

Hansen, Martin O.L. 2008. *Aerodynamics of Wind Turbine Second Edition*. *Sterling, VA*. https://doi.org/10.1002/0470846127.

Hasselmann, Klaus, T P Barnett, E Bouws, H Carlson, D E Cartwright, K Enke, J A Ewing, H Gienapp, D E Hasselmann, and P Kruseman. 1973. "Measurements of Wind-Wave Growth and Swell Decay during the Joint North Sea Wave Project (JONSWAP)." *Ergänzungsheft 8-12*.

Helder, Joop, and Mario Pietersma. 2013. "Umaine–Deepcwind/Oc4 Semi Floating Wind Turbine Repeat Tests." *MARIN, Wageningen, The Netherlands*.

Hsu, Wei ting, Krish P. Thiagarajan, and Lance Manuel. 2017. "Extreme Mooring Tensions Due to Snap Loads on a Floating Offshore Wind Turbine System." *Marine Structures* 55 (September): 182–99. https://doi.org/10.1016/j.marstruc.2017.05.005.

IACS. 2013. "Unified IACS Requirements Concerning Materials and Welding – W22 Offshore Mooring Chain." Vol. DNV-OS-E30.

Jaksic, Vesna, C S Wright, J Murphy, C Afeef, S F Ali, D P Mandic, and V Pakrashi. 2015. "Dynamic Response Mitigation of Floating Wind Turbine Platforms Using Tuned Liquid Column Dampers." *Philosophical Transactions of the Royal Society A: Mathematical, Physical and Engineering Sciences* 373 (2035).

https://doi.org/10.1098/rsta.2014.0079.

Jonkman, Jason M. 2007. “Dynamics Modeling and Loads Analysis of an Offshore Floating Wind Turbine” 8 (11): 1595–1606. https://doi.org/10.4161/hv.21225.

———. 2010. “Definition of the Floating System for Phase IV of OC3.” *Contract* 1 (May): 31. https://doi.org/10.2172/979456.

Jonkman, Jason M., and M. L. Jr. Buhl. 2005. “FAST User’s Guide - Updated August 2005.” https://doi.org/10.2172/15020796.

Jonkman, Jason M., Sandy Butterfield, Walter Musial, and G. Scott. 2009. “Definition of a 5-MW Reference Wind Turbine for Offshore System Development.” *Contract*. https://doi.org/10.2172/947422.

Jonkman, Jason M., Torben Juul Larsen, A. Craig Hansen, Tor Anders Nygaard, K. Maus, M. Karimirad, Z. Gao, et al. 2010. “Offshore Code Comparison Collaboration within IEA Wind Task 23: Phase IV Results Regarding Floating Wind Turbine Modeling.” *European Offshore Wind Conference*, April, 23. https://doi.org/10.1007/s00374-009-0370-2.

Jonkman, Jason M., and Denis Matha. 2013. “Dynamics of Offshore Floating Wind Turbines—Analysis of Three Concepts†.” *Wind Energy*, no. January: 1–20. https://doi.org/10.1002/we.

Karimirad, Madjid. 2013. “Modeling Aspects of a Floating Wind Turbine for Coupled Wave-Wind-Induced Dynamic Analyses.” *Renewable Energy* 53 (May): 299–305. https://doi.org/10.1016/j.renene.2012.12.006.

Karimirad, Madjid, and Constantine Michailides. 2015. “V-Shaped Semisubmersible Offshore Wind Turbine: An Alternative Concept for Offshore Wind Technology.” *Renewable Energy* 83 (November): 126–43. https://doi.org/10.1016/j.renene.2015.04.033.

Karimirad, Madjid, and Torgeir Moan. 2012a. “Feasibility of the Application of a Spar-Type Wind Turbine at a Moderate Water Depth.” *Energy Procedia* 24: 340–50. https://doi.org/10.1016/j.egypro.2012.06.117.

———. 2012b. “A Simplified Method for Coupled Analysis of Floating Offshore Wind Turbines.” *Marine Structures* 27 (1): 45–63.

https://doi.org/10.1016/j.marstruc.2012.03.003.

Kim, Byoung Wan, Sa Young Hong, Hong Gun Sung, and Seok Won Hong. 2015. "Comparison of Simplified Model and FEM Model in Coupled Analysis of Floating Wind Turbine" 5 (September). https://doi.org/10.12989/OSE.2015.5.3.221.

Kimball, Richard, Andrew J. Goupee, Matthew J. Fowler, Erik-Jan Jan De Ridder, and Joop Helder. 2014. "Wind/Wave Basin Verification of a Performance-Matched Scale-Model Wind Turbine on a Floating Offshore Wind Turbine Platform." In *Proceedings of the ASME 2014 33rd International Conference on Ocean, Offshore and Arctic Engineering*, 9B:1–10. American Society of Mechanical Engineers. https://doi.org/10.1115/OMAE2014-24166.

Kvittem, Marit I., and Torgeir Moan. 2015. "Time Domain Analysis Procedures for Fatigue Assessment of a Semi-Submersible Wind Turbine." *Marine Structures* 40: 38–59. https://doi.org/10.1016/j.marstruc.2014.10.009.

Lai, Bin Bin, Cheng Bi Zhao, Xiao Ming Chen, You Hong Tang, and Wei Lin. 2014. "A Novel Structural Form of Semi-Submersible Platform for a Floating Offshore Wind Turbine with Hydrodynamic Performance Analysis." *Applied Mechanics and Materials* 477–478: 109–13. https://doi.org/10.4028/www.scientific.net/AMM.477-478.109.

Landberg, Lars. 2016. *Meteorology for Wind Energy*. Chichester, UK ; Hoboken, NJ: John Wiley & Sons. https://doi.org/10.1002/9781118913451.

Larsen, Torben Juul, and Tor D. Hanson. 2007. "A Method to Avoid Negative Damped Low Frequent Tower Vibrations for a Floating, Pitch Controlled Wind Turbine." *Journal of Physics: Conference Series* 75 (1). https://doi.org/10.1088/1742-6596/75/1/012073.

Lee, Hsien H., S. H. Wong, and R. S. Lee. 2006. "Response Mitigation on the Offshore Floating Platform System with Tuned Liquid Column Damper." *Ocean Engineering* 33 (8–9): 1118–42. https://doi.org/10.1016/j.oceaneng.2005.06.008.

Li, Jiawen, B. Yougang Tang, and C. Ronald W. Yeung. 2014. "Effects of Second-Order Difference-Frequency Wave Forces on a New Floating Platform for an Offshore Wind Turbine." *Journal of Renewable and Sustainable Energy* 6 (3):

033102. https://doi.org/10.1063/1.4872360.

Liu, Zhenqing, Tu Yuangang, Wei Wang, and Qian Guowei. 2019. “Numerical Analysis of a Catenary Mooring System Attached by Clump Masses for Improving the Wave-Resistance Ability of a Spar Buoy-Type Floating Offshore Wind Turbine.” *Applied Sciences* 9 (6): 1075. https://doi.org/10.3390/app9061075.

Liu, Zhenqing, Qingsong Zhou, Yuangang Tu, Wei Wang, and Xugang Hua. 2019. “Proposal of a Novel Semi-Submersible Floating Wind.”

Longuet-higgins, B Y M S. 1957. “The Statistical Analysis of a Random , Moving Surface Author (s): M . S . Longuet-Higgins Source : Philosophical Transactions of the Royal Society of London . Series A , Mathematical Published by : Royal Society Stable URL : Https://Www.Jstor.Org/Stable” 249 (966): 321–87.

Masciola, Marco D. 2013. “Instructional and Theory Guide to the Mooring Analysis Program.” *Nrel*.

Masciola, Marco, Amy N. Robertson, Jason M. Jonkman, Alexander Coulling, and Andrew Goupee. 2013. “Assessment of the Importance of Mooring Dynamics on the Global Response of the DeepCwind Floating Semisubmersible Offshore Wind Turbine.” *23th International Offshore and Polar Engineering* 9: 359–68.

Mattson, Christopher A., Anoop A. Mullur, and Achille Messac. 2004. “Smart Pareto Filter: Obtaining a Minimal Representation of Multiobjective Design Space.” *Engineering Optimization* 36 (6): 721–40. https://doi.org/10.1080/0305215042000274942.

Moharrami, Mohammadreza, and Mazdak Tootkaboni. 2014. “Reducing Response of Offshore Platforms to Wave Loads Using Hydrodynamic Buoyant Mass Dampers.” *Engineering Structures* 81: 162–74. https://doi.org/10.1016/j.engstruct.2014.09.037.

Newman, John Nicholas. 1978. “The Theory of Ship Motions, Advanced in Applied Mechanics, Vol. 18.” Academic Press.

Øye, Stig. 1991. “Dynamic Stall Simulated as Time Lag of Separation.” In *Proceedings of the 4th IEA Symposium on the Aerodynamics of Wind Turbines*.

Ozbahceci, Berguzar Oztunali, Tomotsuka Takayama, Hajime Mase, and Aysen Ergin.

2002. “Occurrence Probability of Wave Grouping for Different Shapes of Wave Energy Spectra.” *Proceedings of the International Offshore and Polar Engineering Conference* 12 (January): 37–42.

Pineda Iván, and Tardieu Pierre. 2016. “Wind in Power Wind in Power,” no. February: 24. https://windeurope.org/about-wind/statistics/european/wind-in-power-2016/.

Pinkster, Johannes Albert. 1980. “Low Frequency Second Order Wave Exciting Forces on Floating Structures.” *Journal of Chemical Information and Modeling* 53 (9): 1689–99. https://doi.org/10.1017/CBO9781107415324.004.

Robertson, Amy. 2015. “Introduction to the OC5 Project.” *EERA Deepwind*, 23. http://www.sintef.no/Projectweb/Deepwind_2015/Presentations/.

Robertson, Amy, Jason M. Jonkman, Fabian Vorpahl, Wojciech Popko, Jacob Qvist, Lars Frøyd, Xiaohong Chen, et al. 2014. “Offshore Code Comparison Collaboration Continuation Within IEA Wind Task 30: Phase II Results Regarding a Floating Semisubmersible Wind System.” In *Volume 9B: Ocean Renewable Energy*, V09BT09A012. San Francisco, California, USA: ASME. https://doi.org/10.1115/OMAE2014-24040.

Robertson, Amy N., Jason M. Jonkman, and Marco D. Masciola. 2014. “Definition of the Semisubmersible Floating System for Phase II of OC4.” *Nrel/Tp-5000-60601*. https://doi.org/10.1021/jp200953k.

Robertson, Amy N., Jason M. Jonkman, Fabian Wendt, and Andrew J. Goupee. 2016. “Definition of the OC5 DeepCwind Semisubmersible Floating System,” 44. https://doi.org/10.1007/s10436-006-0062-y.

Robertson, Amy N., Fabian Wendt, Jason M. Jonkman, Wojciech Popko, Habib Dagher, Sebastien Gueydon, Jacob Qvist, et al. 2017. “OC5 Project Phase II: Validation of Global Loads of the DeepCwind Floating Semisubmersible Wind Turbine.” *Energy Procedia* 137 (October): 38–57. https://doi.org/10.1016/j.egypro.2017.10.333.

Rodrigues, Sílvio F., R. Teixeira Pinto, M. Soleimanzadeh, Peter A.N. Bosman, and P. Bauer. 2015. “Wake Losses Optimization of Offshore Wind Farms with Moveable Floating Wind Turbines.” *Energy Conversion and Management* 89 (January): 933–41. https://doi.org/10.1016/j.enconman.2014.11.005.

Sarpkaya, Turgut. 2010. *Wave Forces On Offshore Structures*. Cambridge: Cambridge University Press. http://ebooks.cambridge.org/ref/id/CBO9781139195898.

Saulnier, Jean Baptiste, Alain Clment, Antnio F.De O. Falco, Teresa Pontes, Marc Prevosto, and Pierpaolo Ricci. 2011. "Wave Groupiness and Spectral Bandwidth as Relevant Parameters for the Performance Assessment of Wave Energy Converters." *Ocean Engineering* 38 (1): 130–47. https://doi.org/10.1016/j.oceaneng.2010.10.002.

Sclavounos, Paul D., S. Lee, J. DiPietro, G. Potenza, P. Caramuscio, and G. De Michele. 2010. "Floating Offshore Wind Turbines: Tension Leg Platform and Taught Leg Buoy Concepts Supporting 3–5 Mw Wind Turbines." In *European Wind Energy Conference (EWEC)*, 3:1–7. https://doi.org/10.1108/IJCHM-08-2013-0350.

Si, Yulin, Hamid Reza Karimi, and Huijun Gao. 2014. "Modelling and Optimization of a Passive Structural Control Design for a Spar-Type Floating Wind Turbine." *Engineering Structures* 69: 168–82. https://doi.org/10.1016/j.engstruct.2014.03.011.

Sørensen, Asgeir J. 2011. "A Survey of Dynamic Positioning Control Systems." *Annual Reviews in Control* 35 (1): 123–36. https://doi.org/10.1016/j.arcontrol.2011.03.008.

Sudhakar, S., and Seeninaidu Nallayarasu. 2014. "Hydrodynamic Responses of Spar Hull with Single and Double Heave Plates in Random Waves." *International Journal of Ocean System Engineering* 4 (1): 1–18. https://doi.org/10.5574/ijose.2014.4.1.001.

Tran, Thanh Toan, and Dong Hyun Kim. 2018. "A CFD Study of Coupled Aerodynamic-Hydrodynamic Loads on a Semisubmersible Floating Offshore Wind Turbine." *Wind Energy* 21 (1): 70–85. https://doi.org/10.1002/we.2145.

Waals, Olaf J. 2009. "The Effect of Wave Directionality on Low Frequency Motions and Mooring Forces." *Proceedings of the International Conference on Offshore Mechanics and Arctic Engineering - OMAE* 4 (PART A): 289–98. https://doi.org/10.1115/OMAE2009-79412.

Walsh, Colin. 2019a. "Offshore Wind in Europe." *Refocus* 3 (2): 14–17.

https://doi.org/10.1016/s1471-0846(02)80021-x.

———. 2019b. “Wind Energy in Europe.”

Wayman, Elizabeth. 2006. “Coupled Dynamics and Economic Analysis of Floating Wind Turbine Systems.” *Doctoral Dissertation, Massachusetts Institute of Technology*, 146.

Zhang, Shining, and Takeshi Ishihara. 2016. “EFFECTS OF MULTIDIRECTIONAL SEA STATES AND FLEXIBLE FOUNDATION ON DYNAMIC RESPONSE OF FLOATING OFFSHORE,” 729–38.

Zhang, Zili, and Christian Høeg. 2020. “Dynamics and Control of Spar-Type Floating Offshore Wind Turbines with Tuned Liquid Column Dampers.” *Structural Control and Health Monitoring*, no. February. https://doi.org/10.1002/stc.2532.

Zhu, Lixin, and Hee-Chang Lim. 2017. “Hydrodynamic Characteristics of a Separated Heave Plate Mounted at a Vertical Circular Cylinder.” *Ocean Engineering* 131 (February): 213–23. https://doi.org/10.1016/j.oceaneng.2017.01.007.

Appendix A

The Modified Inverse FORM method is achieved as follows:

1. Apply Principal Component Analysis (PCA) twice:
    a. between significant wave height (H_s) and wave period (T_p)
    b. between H_s and wind speed at hub height (W).

Note that wind speed at hub height ($z = 36m$) is extracted using power-law by knowing the wind speed at two heights (u_1 at $z_1 = 10m$ & u_2 at $z_2 = 100m$) taken from the metocean data:

$$W = u_1 \left(\frac{z}{z_1}\right)^{\alpha} \tag{A.1}$$

Such that:

$$\alpha = \frac{\ln(u_1/u_2)}{\ln(z_1/z_2)} \tag{A.2}$$

The application of PCA is essential as it de-correlate the two variables of interest and results in principal components ($C_{1_1}, C_{1_2}\ C_2, C_3$) representing ($H_s \rightarrow T_p, H_s \rightarrow W, T_p, W$), respectively. It gives two coefficient matrices (V_1, V_2) that if multiplied by the original components matrix (U) results in rotation of the data into the principal component space:

$$C = UV \tag{A.3}$$

To eschew negative values, the rotated components must be shifted upwards by an amount of s.

$$s = |\min(C_2)| + 0.1 \tag{A.4}$$

2. fit the most dominant components (C_{1_1}, C_{1_2}), since they have the highest variance, into a cumulative distribution function (CDF) defined by either 2-parameter (*a*-*b*) or 3-parameter (*a*-*b*-*c*) Weibull fit:

$$F(x) = \begin{cases} 1 - e^{-\left(\frac{(x-c)}{b}\right)^a} & x \geq 0 \\ 0 & x < 0 \end{cases} \tag{A.5}$$

such that $a, b,$ and c are the shape, scale, and position parameter, respectively. In the case of 2-prameter fitting, c becomes zero. The two fittings do not show a big difference as shown in Figure A.1.

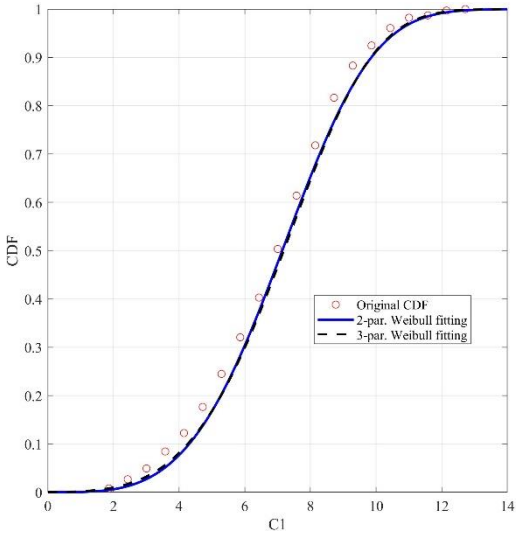

Figure A.1: Original CDF and Weibull fitting.

3. divide the other components into bins such that each bin has its CDF fitted with a statistical distribution that beholds the mean μ and standard deviation σ information of the data such as a normal or lognormal distribution. Figure A.2 illustrates this with the second component. The reason of selecting this distribution is to be able to relate the statistical parameters of these components with the first one via a linear or quadratic function of the data as seen necessary. In this study, a quadratic formulation is used:

$$F_\mu(C_1)_n = s_1 C_{1_n}^2 + s_2 C_{1_n} + s_3 \tag{A.6}$$

$$F_\sigma(C_1)_n = s_4 C_{1_n}^2 + s_5 C_{1_n} + s_6 \tag{A.7}$$

where $n = 1, 2$ for the two components. Parameters in Eq. (A.7) are sometimes constrained as seen necessary to always result in a positive standard deviation.

Figure A.3 & Figure A.4 illustrates these relationships and provides the fitting coefficients obtained.

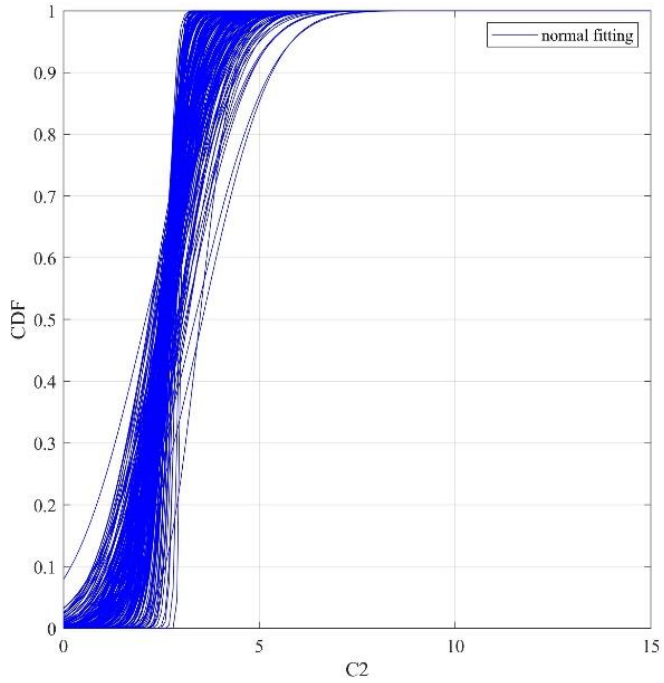

Figure A.2: Normal fitting of CDF of all the bins for the second component C_2.

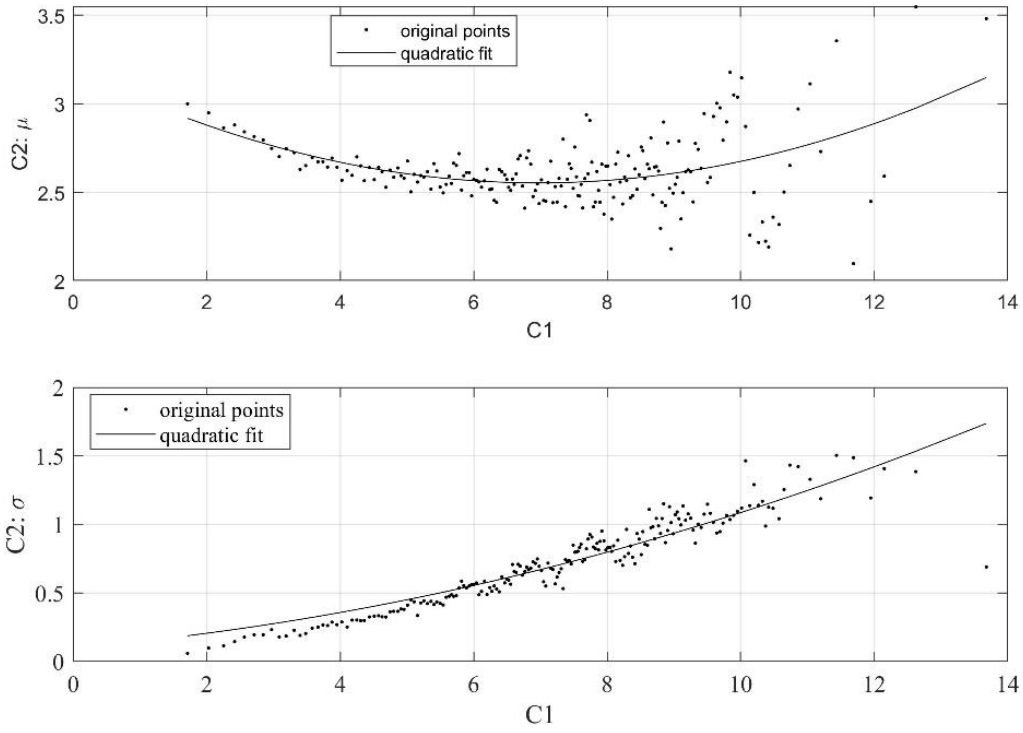

Figure A.3: Quadratic fitting of the scattered C_1 compared to the mean and standard deviation of C_2 data.

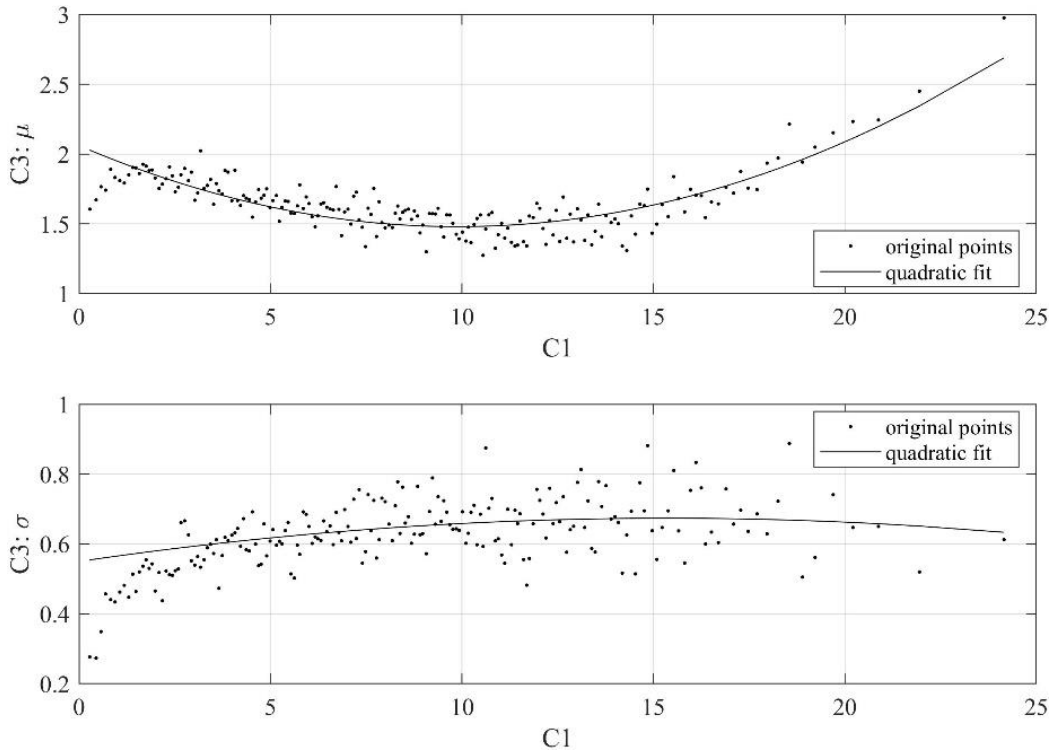

Figure A.4: Quadratic fitting of the scattered C_1 compared to the mean and standard.

Table A.1: Summary of the fitting coefficients utilized.

Principal component	Fitting type	Fitting coefficients					
		a			b		
C_{1_1}	2-par. Weibull	3.64			8.00		
C_{1_2}		1.75			10.02		
		s_1	s_2	s_3	s_4	s_5	s_6
C_2	Normal	0.01	-0.18	3.19	0.01	0.04	0.100*
C_3		0.01	-0.12	2.06	-0.01	0.02	0.55

*: value fixed at bound

4. create standard normal space components of $U1, U2, \& U3$ and discretize the circumference of the sphere that has a radius of a reliability index β as following (Figure A.5):

$$\begin{cases} x_i = \beta cos\phi_j cos\theta_i \\ y_i = \beta cos\phi_j sin\theta_i \\ z_i = \beta sin\phi_j \end{cases} \quad with\ \theta_i = \frac{i2\pi}{k}, \phi_j = \frac{j2\pi}{k}; \quad i, j = 1, 2, \dots, k \tag{A.8}$$

such that:

$$\beta = \phi^{-1}\left(1 - \frac{T_{ss}}{365 \times 24 \times T_r}\right) \tag{A.9}$$

where $T_{ss}$is the sea-state duration in hours, T_r is the demanded return period in years (in this case, 50 years), and $\phi()$ represents the standard normal distribution.

5. Evaluate the quantile positions in all directions and evaluate the inverse CDF at the principal component space.
6. Finally, rotate back to the physical space to get the contours at the requested return period as seen in Figure 5.4

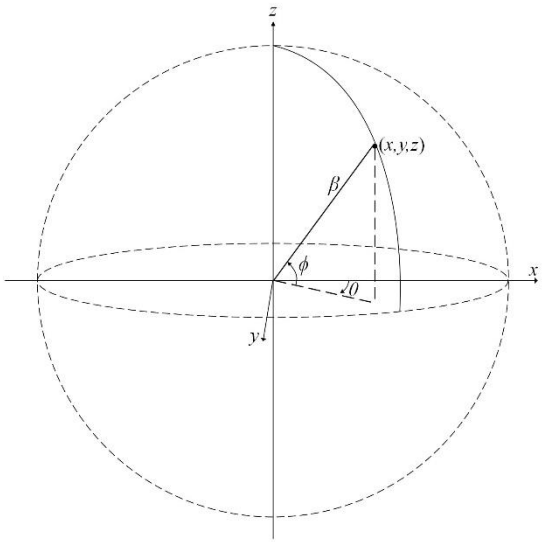

Figure A.5: Standard normal space sphere.